FACULTY
OF MATHEMATICS
AND PHYSICS
Charles University

DOCTORAL THESIS

František Staněk

Source mechanisms of microseismic events induced by hydraulic fracturing

Department of Geophysics

Supervisor of the doctoral thesis: Mgr. Leo Eisner, Ph.D.
Study programme: Physics
Specialization: Geophysics

Prague 2018

I declare that I carried out this doctoral thesis independently, and only with the cited sources, literature and other professional sources.

I understand that my work relates to the rights and obligations under the Act No. 121/2000 Coll., the Copyright Act, as amended, in particular the fact that the Charles University has the right to conclude a license agreement on the use of this work as a school work pursuant to Section 60 paragraph 1 of the Copyright Act.

In Prague 22.04. 2018

František Staněk

Thank you, Leo!

Název: Zdrojové mechanismy mikroseismických jevů indukovaných hydraulickým štěpením

Autor: Mgr. František Staněk

Katedra: Katedra geofyziky

Vedoucí disertační práce: Mgr. Leo Eisner, Ph.D.

Abstrakt:

Pochopení ekonomické úspěšnosti nekonvenční těžby z břidlic vyžaduje vysvětlení vztahu mezi indukovanou seismicitou a hydraulickým štěpením. Tato práce se zabývá pozorováním a analýzou syntetických a reálných dat z hydraulického štěpení a seismického monitorování. Zejména se opírá o analýzu zdrojových mechanismů indukovaných seismických jevů, které se v několika posledních letech začaly určovat a interpretovat i v průmyslu. Výsledky analýzy jsou interpretovány pomocí geomechanického modelu vztahu mezi hydraulickým štěpením břidlic a indukovanou seismicitou.

Studium zdrojových mechanismů začíná detailní analýzou prostorového rozložení stability inverze plného momentového tensoru, které bylo vymapováno dle synteticky napočtených kondičních čísel v prostoru okolo různých typů monitorovacích sítí, zahrnující husté sítě na povrchu, ale i řídké sítě s přijímači ve vrtech. Stabilita výpočtu zdrojových mechanismů byla testována v závislosti na různých podmínkách, především pak na velikosti a geometrii monitorovací sítě a různých hladinách šumu v datech. V této práci je ukázáno, že husté povrchové monitorovací sítě mohou dosahovat velmi dobré stability invertovaných zdrojových mechanismů, které mohou být dále interpretovány. Zároveň tato studie ukazuje rostoucí podíl nestřižné složky momentového tensoru s rostoucí hladinou šumu (relativně k signálu), ale překvapivě také i závislost stability inverze na typu mechanismu. Výsledky zpracování reálných dat naměřených v průběhu hydraulického štěpení břidlic v Severní Americe jsou získány použitím nově vyvinuté metody, která umožňuje detekci, lokaci a současně i inverzi zdrojového mechanismu. Součástí zpracování dat je i testování spolehlivosti a stability obdržených výsledků včetně sledování koherence amplitud podélných vln pro detekci. Výsledné, detailně analyzované, zdrojové mechanismy ukazují na dominanci dip-slip a strike-slip typu mechanismů s převažující střižnou složkou, které byly následně využity k výpočtu napětí a nakonec i k interpretaci geomechanickým modelem skluzu podél vrstevních ploch vysvětlujícím vztah mezi hydraulickým štěpením břidlic a indukovanou seismicitou. Práce je zakončena diskuzí různých způsobů ověření navrhovaného modelu a návrhem experimentu, který by mohl pomoci ověřit, zdali je navrhovaný geomechanický model opravdu ten správný.

Klíčová slova:
Mikroseismické monitorování, hydraulické štěpení, momentový tenzor, zdrojové mechanismy, geomechanický model

Title: Source mechanisms of microseismic events induced by hydraulic fracturing

Author: Mgr. František Staněk

Department: Department of Geophysics

Supervisor of the doctoral thesis: Mgr. Leo Eisner, Ph.D.

Abstract:

Understanding economic success of unconventional production from shales requires an explanation of the relationship between induced seismicity and hydraulic fracturing. This thesis deals with observing and analyzing synthetic and real microseismic monitoring data acquired during hydraulic fracturing. The thesis is based on observation and analyses of source mechanisms of induced microseismic events that have recently become regularly inverted and interpreted in the oil and gas industry. The results of analyses are interpreted with the geomechanical model of the relationship between hydraulic fracturing and induced seismicity.

The study of source mechanisms starts with detailed analyses of spatial distribution of full moment tensor inversion stability. It was mapped based on synthetically computed condition numbers in the vicinity of different monitoring arrays including dense arrays at the surface and sparse arrays with sensors in the boreholes. Stability of inversion was tested under several conditions, mainly dependency on size and geometry of monitoring array and level of noise in the data. In this part of the thesis it is shown that dense surface arrays may provide very stable inversion of source mechanisms which may be interpreted. The study shows that an increasing percentage of non-shear components is present with an increasing level of noise (relatively to signal). Surprisingly, the tests reveal also a dependency on the type of source mechanism. Results of the processing of the real data recorded during hydraulic fracturing of shale formation in North America are obtained using newly developed methodology capable to detect, locate and invert source mechanism of a microseismic event. Part of the analyses was also a test of reliability and stability of obtained results including checking amplitude coherency of compressional waves used for detection. Final, analyzed in detail, source mechanisms show dominancy of dip-slip and strike-slip type of mechanisms with prevailing shear component. The mechanisms were later used for the inversion of stress field orientation and for interpretation with the geomechanical bedding plane slip model explaining the relationship between hydraulic fracturing in shale and induced seismicity. The thesis is concluded with a discussion about the possible ways on how to prove the suggested model and a design of an experiment that could possibly prove the reliability of the model.

Keywords:
Microseismic monitoring, hydraulic fracturing, moment tensor, source mechanisms, geomechanical model

Contents

Introduction

Chapter 5

Conclusions

Outlook

Introduction

Thesis motivation

Hydraulic fracturing is a petroleum engineering method enabling hydrocarbon production from unconventional, lowly permeable, reservoirs such as tight sands or shales. Development of this stimulation technique together with an ability to drill horizontal wells were the key technologies which enabled economically successful production from unconventional reservoir in the last two decades. Hydraulic fracturing consists of pumping fluids into the well under the pressure high enough to crack the target formation. It has been known since 1960s that pumping fluid into underground induces (micro-)earthquakes, so-called microseismic events. They can be recorded with a passive microseismic monitoring network either from (near-)surface or from borehole(s). The monitoring of these events is used to map the hydraulic fractures and understand what the injected fluid does in the underground. The main goals of microseismic monitoring are to detect events from continuous records, locate the events, and get as much as possible information about the hydraulic fracture and the reservoir.

One of the main challenges of the current production from unconventional reservoirs is to understand how and why the hydraulic fracturing results in high production. Original models of single symmetrical hydraulic fractures underestimate the observed production by orders of magnitude. Therefore, engineers use concept of stimulated reservoir volume to estimate production. Such volumes are estimated from the microseismicity but even these models encounter significant problems when predicting observed production. Therefore, any information on interaction between fluid, fracture and rock formation may provide new understanding how to produce from unconventional reservoirs. For example, one may be motivated to explain why North America shales do and why Polish shales do not produce commercial quantities of natural gas and oil.

While locations of microseismic events are well studied and continuously improved by commercial companies. Very little attention was paid to source mechanisms of these induced events although they may provide crucial insight into interaction between the hydraulic fracture and formation. General motivation for this thesis is to determine source mechanisms of real microseismic events induced by hydraulic fracturing of shale, test which parts of the determined source mechanisms are suitable for interpretation, specifically their shear and non-shear components. This understanding in turn allows us to develop knowledge of the response of shale reservoir to the hydraulic fracture stimulation and interpretation of the observed microseismic data. Ultimately, better understanding may lead to optimizing the process of stimulation and more effective hydrocarbon production or even production.

At the beginning of my doctoral studies, back in 2013, the source mechanism inversion was a novel concept in microseismic community. Nowadays, it has become part of standard processing delivered by most of service companies. However, the quality of the source mechanisms is sometimes speculative and resulting interpretations differ widely. The reasons for such inconsistency in results can be that different geophysicists analyze different, sometimes very complicated, data from different areas and the fact that an inversion of source mechanism for weak microseismic event is not always easy. In addition, the monitoring networks are significantly different from the earthquake seismology. There are several limitations such as low signal-to-noise ratio of data recorded by arrays of receivers at the surface or small linear array of receivers in boreholes. Different source mechanisms obtained from different monitoring arrays result in different interpretations adding little to no understanding. Therefore, my motivation was to carefully test the most important factors affecting source mechanism determination from the microseismic monitoring arrays on synthetic and real datasets and understand what can be interpreted in the analysis of real datasets. I was lucky that I could use for my doctoral studies unique dataset recorded by a large surface array during hydraulic fracturing of a shale formation with many detected high-quality events. That allowed me to fulfill the plan to invert stable source mechanisms which were explained with a geomechanical model explaining interaction between injected fluids and response of the shale formation.

Thesis overview

The main part (Chapters 1 to 5, Conclusions and Outlook of this thesis) of the presented doctoral thesis is comprised of seven peer-reviewed articles which I have authored/co-authored during my studies. Five articles are published in scientific journals with IF, four of them are with me as the first author:

Staněk, F., Eisner, L. and T.J. Moser, 2014. Stability of source mechanisms inverted from P-wave amplitude microseismic monitoring data acquired at the surface. *Geophys. Prospect.*, 62(3), 475–490.

Anikiev, D., Valenta, J., **Staněk, F.** and L. Eisner, 2014. Joint location and source mechanism inversion of microseismic events: benchmarking on seismicity induced by hydraulic fracturing. *Geophys. J. Int.*, 198(1), 249-258.

Staněk, F., Anikiev, D., Valenta, J. and L. Eisner, 2015. Semblance for microseismic event detection. *Geophys. J. Int.*, 201(3), 1362-1369.

Staněk, F., Jechumtálová, Z. and L. Eisner, 2015. Reservoir stress from microseismic source mechanisms. *The Leading Edge*, 34(8), 890–893, 895.

Staněk, F., Eisner, L. and A. Vesnaver, 2017. Theoretical assessment of the full-moment-tensor resolvability for receiver arrays used in microseismic monitoring. *Acta Geodyn. et Geomater.*, 14(2), 233-240.

Staněk, F. and L. Eisner, 2017. Seismicity Induced by Hydraulic Fracturing in Shales: A Bedding Plane Slip Model. *J. Geophys. Res.*, 122, 7912–7926.

Eisner, L. and **F. Staněk,** 2018. Microseismic data interpretation — what do we need to measure first? *First Break*, 36(2), 55 – 58.

The chapters are logically ordered and present results which are connected from tests on synthetic datasets through processing and analysis of real dataset to an interpretation with a new geomechanical model.

The first paper, presented in this thesis as the Chapter 1, describes test on a synthetic dataset where I studied limitations of full-moment-tensor invertability for different monitoring arrays used by companies in microseismic community. I was computing condition numbers of the inversion matrix for the hypothetical event in a 3-D space for three types of arrays. The obtained results show that some monitoring arrays do not provide suitable datasets for the full-moment tensor inversion due to poor receiver coverage of the focal sphere. However, the large surface star-like array, for which I have available real dataset used in this thesis, provide the most robust source mechanism inversion.

The Chapter 2 summarizes results of tests of stability of source mechanism inversion from P-wave amplitudes recorded by large, dense star-like array of receivers deployed at the surface on synthetic datasets. As the main challenge of surface monitoring is poor signal-to-noise ratio, therefore I have tested mainly effects of noise. In addition, I have carried out a set of tests to determine robustness to errors in the velocity model used in the inversion of the full moment tensors of microseismic events. The results show low sensitivity to incorrect velocity model ignoring anisotropy and very good stability of inversion even for examples with signal-to-noise ratio lower than one. The increasing level of noise in data cause increasing non-shear component with Compensated Linear Vector Dipole approximately two-times higher than volumetric component. Surprisingly, I observe also a dependency on type of source mechanism, the inversion of strike-slip seems to be more stable than dip-slip. Such tests are used to understand the results of processing of real dataset. Knowledge of effects caused by noise in the data are also important for interpretation of source mechanisms.

The Chapter 3 presents an article describing a method of automatic processing of the real dataset. The newly developed algorithm is capable to detect a microseismic event from continuous data, and jointly locate the event and invert its full-moment-tensor source mechanism. The method is using stacking of amplitudes from all the receivers along a precomputed travel-time moveout to detect events which may not even be visible on a single trace due to low signal-to-noise ratio. We selected the strongest events, visible on individual receivers and carried out manual picking suitable for source mechanism inversion and location. The comparison of these results with automatic processing enabled generalization of the automated results. There are mainly two types of mechanisms – dip-slips and strike-slips. The events with these two types of mechanisms differ in the percentage of the non-shear component. The automatically processed source mechanisms show on average higher percentage of the non-shear components since the amplitudes for inversion are taken automatically along computed moveout derived from an imperfect velocity model while the manual picking determines mostly the first arrivals correctly.

The Chapter 4 is derived from the article describing the semblance computation for microseismic data detection. The semblance is rarely used in earthquake seismology because the arrays are usually not dense enough. The use of semblance in active seismic data processing assumes homogeneous radiation pattern. Therefore, a new method of semblance computation was needed. This method helps to eliminate false detections and detect weaker microseismic events providing a more complete dataset for interpretation.

An important insight into stress orientation determined by the source mechanisms of the microseismic events is described in the Chapter 5. I have used the source mechanisms inverted from automatically and manually processed data and compared the results. The important result is that I have got one stress field for all selected source mechanisms. This means that the observed source mechanisms can be explained by a single stress field. This observation implies that there is no evidence of significant stress changes in time and space during the hydraulic fracturing or that the microseismic events do not result from stress heterogeneity. In addition, I obtained orientation of the three principal stress axes very similar for both manual and automated processing of events. The only difference between tested groups of mechanisms is in the stress ratio between magnitudes of stresses, but it is necessary to note that it is the least stable parameter inverted.

The Conclusions of this thesis comprises all the previous results and interprets them with a geomechanical model called “bedding plane slip”. This model explains locations of the events elongated in the direction of maximum horizontal stress, prevailing presence of the dip-slip type of source mechanisms during the hydraulic fracture creation, orientation of the almost vertical plane of the observed source mechanisms in direction of maximum horizontal stress and dominant shear component of the source mechanisms. Unlikely slipping bedding plane (from the geomechanical point of view) results probably from the fact that fractured shales are over-pressured horizontally layered rock.

The last part of the thesis is an Outlook. There are summarized currently accepted models explaining induced seismicity, their implications on predicted production and discussed possible ways to prove the suggested bedding plane model. The proposed experiment could provide deeper insight on the plane (possibly horizontal plane) which is faulting based on seismic directivity measured by Distributed Acoustic Sensors in the nearby wells drilled around the sources.

Chapter 1

Theoretical assessment of the full-moment-tensor resolvability for receiver arrays used in microseismic monitoring

Published in *Acta Geodynamica et Geomaterialia*, in 2017,
Volume 14, No. 2 (186), 235-240. doi: 10.13168/AGG.2017.0006

Frantisek Staněk [1,2,3], Leo Eisner [3,4] and Aldo Vesnaver[1]

[1] *The Petroleum Institute, Dept. of Geosciences, Abu Dhabi, United Arab Emirates*

[2] *Charles University, Faculty of Mathematics and Physics, Dept. of Geophysics, Prague, Czech Republic*

[3] *Czech Academy of Sciences, Institute of Rock Structure and Mechanics, Dept. of Seismotectonics, Prague, Czech Republic*

[4] *Seismik s.r.o., Prague, Czech Republic*

An inversion of full moment tensors representing source mechanisms is becoming routinely used when interpreting microseismic monitoring. However, a stability of such inversion varies significantly for different receiver arrays. Unlike stability of location, which is hard to assess, the stability of inverted full moment tensor can be measured by a condition number. We tested three types of receiver arrays (dense surface array, dual borehole array and multi-borehole array) used in the microseismic monitoring and computed the theoretical stability of full moment tensor inversion from P- or P- and S-wave amplitudes at areas of interest. We analyzed 3D distributions of the condition numbers and show that with surface and multi-borehole arrays of receivers we are capable of inverting stable source mechanisms for the events located at depths comparable to the maximum offset of receivers, but shallower events and the events at the depths of the borehole arrays are poorly constrained. This study provides a guidance for a quick prediction of source mechanism inversion quality. Computing condition numbers does not require any information about the data, it measures a theoretical quality of the moment tensor

inversion. The computed condition numbers represent inversion for ideal dataset with the selected geometry.

1.1 Introduction

Microseismic monitoring is used to evaluate an efficiency of reservoir stimulation with the goal of improving production from low permeability formations. Source mechanisms are retrieved along with microseismic event locations mapping the geometry of the hydraulic fracture. These mechanisms provide an additional information on the activated fault or fracture orientation, the direction of the slip relative to the fault plane and may also resolve if microseismic events have a shear or a (partly) non-shear component. Such additional information is used to determine geomechanical parameters of the stimulated rock and improve the interpretation. For instance, based on event locations and their source mechanisms, we can estimate discrete fracture network, compute stimulated rock volume, invert for local stress field or estimate pore pressure perturbations needed to activate faults (e.g., Zoback, 2007; Warpinski *et al.*, 2013; Neuhaus *et al.*, 2014). These additional parameters lead to better understanding and optimization of the reservoir stimulation resulting in an increased reservoir permeability and hydrocarbon production.

Each step in microseismic data processing carries some uncertainty and every uncertainty may affect data interpretation (e.g., Zimmer, 2011). For example, uncertainty in an event location negatively affects the source mechanism inversion and may project into a false fault plane or spurious non-shear components may be obtained. Not every inverted source mechanism has quality good enough to be used for further interpretation or, at least, should be treated with higher uncertainty.

The source mechanisms of microseismic events are usually inverted from the amplitudes and phases of the first arrivals of P- and S-waves (e.g. Jechumtálová and Eisner, 2008), alternatively from S/P amplitude ratios (Foulger *et al.*, 2014). The inversion of full-waveforms is not as common as in earthquake seismology because the reservoir models generally do not allow modeling the full waveforms at high frequencies – in microseismic monitoring, the signal strength usually peaks at frequencies in the band 20-40 Hz for surface monitoring and typically waveforms with peak frequencies 100 Hz and higher are used in borehole monitoring (Duncan and Eisner, 2010). Each source mechanism of a point source is mathematically fully described with a full moment tensor. It carries information about the orientation of the fault plane, sense of slip on the fault and the mode of the fracture. Studying shear and non-shear components is crucial for distinguishing pure-shear event from (partly) non-shear event indicating fracture opening or closing.

There are many sources of uncertainties influencing a source mechanism inversion, such as the data noise (e.g. Staněk *et al.*, 2014; Mustać and Tkalčić, 2016), uncertainty in location and velocity model (e.g. Šílený, 2009; Yagi and Fukahata, 2011), uncertainty in attenuation model, receiver array geometry, etc. The receiver array geometry is usually the only thing we can control. Therefore, we focused our study on the evaluation of this effect.

In this study, we compute the theoretical stability of source mechanisms for three examples of receiver arrays currently used in microseismic monitoring. Specifically, we compute a 3D distribution of condition numbers highlighting zones with good and bad quality of inverted full moment tensors representing source mechanisms. Although the condition numbers do not depend on the data, the condition numbers say how much the source mechanism parameters are stable and sensitive to a small change in the input: in our case amplitude, velocity model, event location, etc. We have chosen condition numbers as one of the commonly used and robust measures of inversion stability, but other parameters might be used to evaluate source mechanism quality as well, e.g., error ellipsoid (Zahradník and Custodio, 2012). However, none of the other measures represents perfectly the uncertainty and each of the measures of the source mechanism stability has both drawbacks and advantages.

We mimic three different types of arrays used to monitor reservoir stimulation that were used in publications interpreting source mechanisms of microseismic events. We test a dense surface array (e.g., Anikiev *et al.*, 2014), dual borehole array (Jechumtálová *et al*., 2016) and receiver arrays in many shallow boreholes (Mahrooqi *et al*., 2013).

The goal of this study is not to criticize or praise any type of the arrays. Every array is designed for a specific purpose, and not necessarily for estimating the source mechanisms, and is limited by different rock types and surface infrastructures. Also, every project has a limited budget. Our goal is to quickly predict the quality of source mechanisms and possibly avoid an erroneous interpretation of microseismic results. Another goal is to provide a tool for an improvement of array design and selecting appropriate installations to optimize the cost of microseismic monitoring.

1.2 Methodology

For each selected receiver array, we set an area of interest (the stimulated area) where we test the theoretical assessment of the full-moment-tensor resolvability. Surface and near-surface arrays have all the expected events below the arrays, unlike the deeper borehole arrays which are intentionally installed closer to the stimulated part of the reservoir and events occur at similar depths as the depths of receivers.

In the area of interest, we define a regular grid of potential microseismic event locations for which the stability of source mechanism inversion is computed. We assume that all receivers of the arrays contribute with the signal (P- or P- and S-wave amplitudes). Hence, our study presents the best-case scenario for the strongest events, i.e. events with sufficient signal-to-noise ratio at the monitoring arrays as discussed later.

We compute synthetic first arrival amplitudes (either positive or negative values) of direct P- and S-wave for the receivers from each point of the grid of potential microseismic event locations. For simplicity, we assume a homogeneous isotropic medium and a point source; however, we realize that more complex media would affect the source mechanism inversion. The point source is a good approximation for microseismic events which are smaller than magnitude 0. The receiver array configuration has a dominant effect because sufficient receiver coverage overcomes uncertainties in the velocity model (Šílený, 2009). We neglect the noise effect and assume that we are able to correctly pick the right arrival amplitudes at every receiver, i.e., that we have a sufficient signal-to-noise ratio at every receiver. The latter one is quite a strong assumption for all the tested arrays, but this study evaluates ability to correctly invert for the source mechanism of the well recorded microseismic events. This means that the predicted stability of the inversion is true only for the events strong enough to be recorded on all receivers of the tested monitoring array. Generally, the downhole monitoring arrays achieve high signal-to-noise ratio even for weaker events, it is not true for surface monitoring arrays. In such sense the condition number represents an ideal situation and real data may only degrade such assumption. We remark that downhole monitoring array tests assume the inversion of S-waves in an isotropic velocity model, which may not be a suitable approximation in anisotropic media (Grechka, 2015).

We compute Green's function matrix G for the full moment tensor M inversion of the first P-wave arrival amplitudes (either positive or negative values – see Eisner *et al.*, 2010 with example of real data picking strategy) for the surface vertical component array and shallow boreholes receivers with only vertical components array, and another matrix of both the first P- and first S-wave arrival amplitudes modeled for the dual borehole array. The observed amplitudes of direct P- and S-wave displacement d can be related with G and M by equation

$$d = G * M \text{ .} \tag{1.1}$$

An example of matrixes d and G for one three-component station and both P- and S-waves looks like this

$$d = \begin{bmatrix} A_{PN} \\ A_{PE} \\ A_{PZ} \\ S_{PN} \\ S_{PE} \\ S_{PZ} \end{bmatrix}, G = \begin{bmatrix} G_{PN}(1) G_{PN}(2) \ldots G_{PN}(6) \\ G_{PE}(1) G_{PE}(2) \ldots G_{PN}(6) \\ G_{PZ}(1) G_{PZ}(2) \ldots G_{PN}(6) \\ G_{SN}(1) G_{SN}(2) \ldots G_{SN}(6) \\ G_{SE}(1) G_{SE}(2) \ldots G_{SE}(6) \\ G_{SZ}(1) G_{SZ}(2) \ldots G_{SZ}(6) \end{bmatrix}.$$

Here A_{PN} is an amplitude of P-wave displacement measured on north component; $G_{PN}(1)$ is the P-wave Green's function's derivative for a far-field ray approximation of north component amplitude due to the first component of moment tensor M; numbers (1)…(6) denote all six independent components of M. Time variation of $G*M$ in a far-field ray approximation is delta function. That is why at every station each component is represented by just a single time sample (at the first arrival P- or S-wave).

The least-square moment tensor inversion of linear equation (1.1) is

$$M = (G^T G)^{-1} G^T d \text{ .} \tag{1.2}$$

The condition number CN is defined as a square root of a ratio between the maximum and the minimum eigenvalue of the symmetric inversion matrix G^TG in equation (1.2):

$$CN = \sqrt{\frac{\max\left[eig\left(G^T G\right)\right]}{\min\left[eig\left(G^T G\right)\right]}} \,. \tag{1.3}$$

A well-conditioned inversion has a low condition number and its result is stable, whereas ill-conditioned inversion has a high condition number and the resulting source mechanism is very sensitive to any small change in the input. While low condition number does not guarantee correctly inverted mechanism (due to uncertain velocity and attenuation models, incorrect picks, etc.), the high condition number means highly unstable and probably incorrect source mechanism even if the event is well recorded with a high signal-to-noise ratio. Note that determination of the condition number does not require any information about the data and is only dependent on matrix $\boldsymbol{G}$, hence on source-station configuration and the assumed velocity model.

The specification of a condition number threshold between well- and ill-conditioned inversions is not clear and depends also on the inversion parametrization. Dufumier and Rivera (1997), using the same condition number definition as we do in this study, suggest a condition number magnitude providing reliable results in order of first tens, whereas, Nolen-Hoeksema and Ruff (2001) or Vera Rodrigues *et al*. (2011), using condition number definition without the square root, get results with sufficient quality using the condition numbers as large as 500. Therefore, because we are interested just in relative resolvability measure, we tentatively assume that a reasonable upper limit for a reliable source mechanism inversion is 20 and we show the condition numbers on a scale from 1 to 20. Our results are 3D grids of condition numbers showing zones where the full moment tensors describing source mechanisms are expected to be stable and reliable for an interpretation.

1.3 Stability for three types of microseismic monitoring arrays

The first tested monitoring array is a surface star-like array with 800 receivers in 8 arms around the wellhead. Each arm is 2.5 km long and the whole array is covering approximately 25 km^2. The area of interest where we expect induced events is around the stimulated lateral parts of the four hypothetical treatment wells at the depth 2 km. Inverting P-wave amplitudes from all the receivers on vertical components, we get the lowest condition numbers around 5 (the most stable results) for the locations below the middle of the array (Figure 1.1). The quality of the inverted source mechanisms decreases to the edges of the star and with the depth. The events located deeper than 2300 m, i.e., approximately the length of the arm, have source mechanisms inverted very poorly.

Based on our results, the inverted source mechanisms of real events presented in Anikiev *et al.* (2014) or Staněk and Eisner (2013) of this thesis are stable and could be used for further interpretations. This statement neglects the noise effect, but Staněk *et al.* (2014) showed that a source mechanism inversion using the method of equation (1.2) represents the stacking which suppresses the noise and results in reliable source mechanisms even for weak events. The results of Anikiev *et al.* (2014) are consistent with this conclusion, as the achieved results have high stability of the inverted strikes even for weak events with moment magnitudes down to -1.7.

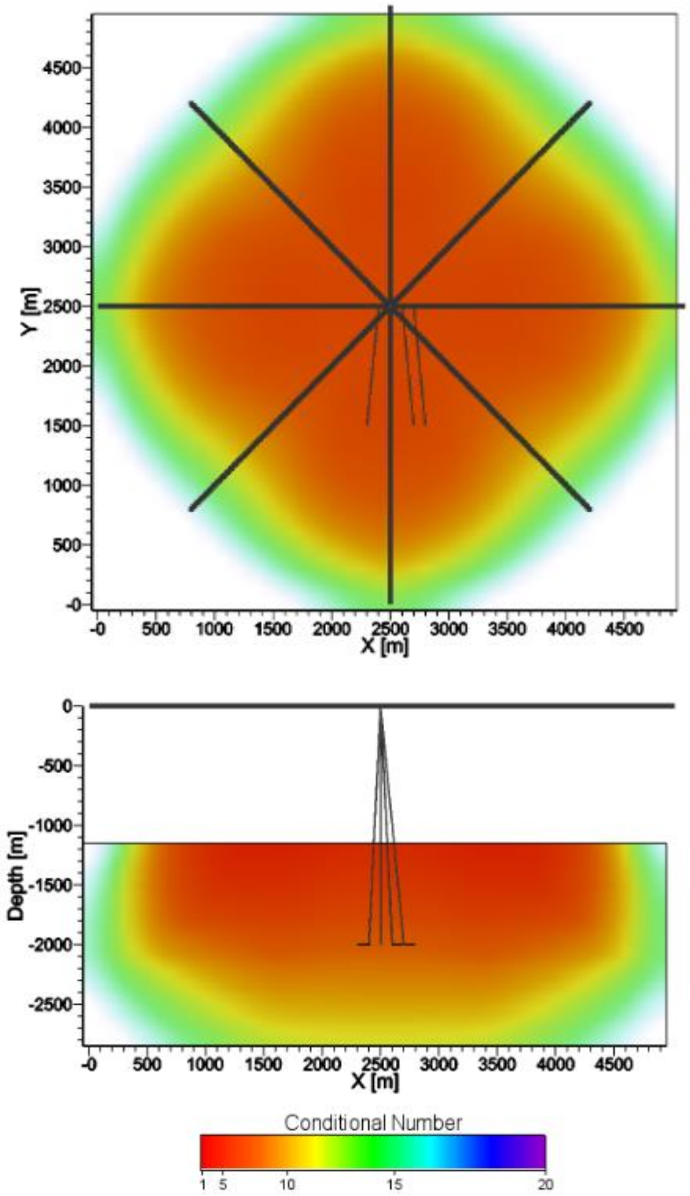

Figure 1.1: Horizontal and vertical cross-section slices of condition numbers computed for a dense surface star-like array (black lines). The hypothetical horizontal treatment wells are shown as thin black lines in the horizontal (at the depth 2 km) and the vertical (at Y=2500 m) cross-sections. The quality of the inverted source mechanisms decreases for higher condition numbers, from red to blue. The values above 20 are shown as white color.

The second tested array configuration is a dual borehole monitoring array with 11 receivers in each well, similar to Jechumtálová at al. (2016). The vertical wells are drilled 500 m from each other and the receivers are located at depths ranging from 1800 to 1920 m. In this case, we use as input both P- and S-wave amplitudes, because they are commonly used for borehole receivers. The most stable source mechanisms for this array are estimated between the two wells, but not along the plane connecting them as shown in Figure 1.2. The color scale is the same as in Figure 1.1. The best possible inversion with CN = 7.7 is achieved for an event located at the depth of the center receivers, and with the angle 45° between the event location and the plane containing both wells. The unstable results depicted by high condition numbers are for events located too far away from the wells, and close to the plane containing both wells and in the vicinity of each well. These results are consistent with Vavryčuk (2007), who showed that the full moment tensor is not constrained along the plane containing both monitoring wells. This problem could be practically solved using arrays in slightly deviated wells (Vera Rodrigues *et al.*, 2011) which improves focal sphere coverage in the problematic direction, or by using a constrained inversion (Jechumtálová and Šílený, 2005). Luckily, events located by Jechumtálová *et al.* (2016) seems to be in a zone (cut by cross-sections in Fig. 1.2) where we get relatively low condition numbers, indicating stable inversion of the observed source mechanisms.

The inversion from the surface array seems stable for most stimulation area because of the higher number of receivers and better focal sphere coverage. Comparing to (near-)surface arrays, the key advantage of borehole receiver arrays is the short distance from the induced events, the resulting availability of S-wave amplitudes and the detectability of low magnitude events.

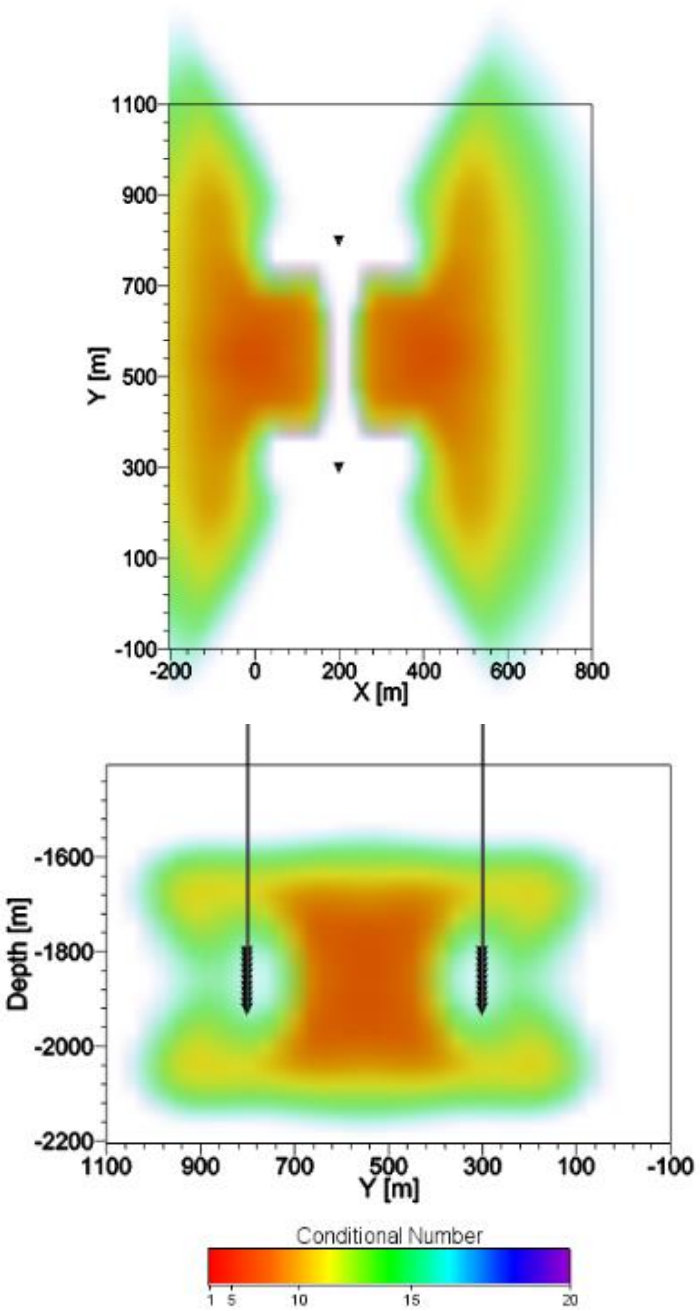

Figure 1.2: Horizontal and vertical cross-sections of condition numbers computed for a dual borehole array. The wells are shown as thin black lines and the receivers of the monitoring array are shown as black upside-down triangles. The condition numbers are shown at the horizontal (at the depth 1820 m) and the vertical (at X=370 m) cross-section slices.

The third tested array consists of 13 shallow boreholes arrays with 104 receivers in total, as illustrated in Figure 1.3. A similar array was used by Mahrooqi *et al.* (2013) to study source mechanisms in Oman. Although this array is designed to monitor a stimulation in a very shallow reservoir, we test the source mechanism inversion from only P-wave amplitudes, because S-waves are very complex in shallow horizontal propagation. For such receiver geometry, we get a very good stability of the source mechanisms inverted below the center of the (multi-)borehole array at the depths exceeding 300 m and optimally around 700 m, as shown by the red area in Figure 1.3 with minimum CN=2.7. At this depth, comparable to the offsets of the monitoring wells, we have high stability and good focal sphere receiver coverage, similarly as for the surface array. Unfortunately, the real stimulated reservoir is shallower and the monitoring was designed to detect events at depths shallower than 500 m. At these depths, the focal sphere coverage is worse. For some locations, we get extremely high condition numbers because most of energy comes from the receivers, which are close to the horizontal plane of the inverted source mechanisms. Horizontal rays do not constrain the vertical component of moment tensor, as it is well known in global seismology (Lay and Wallace, 1995). This situation is similar to the borehole array.

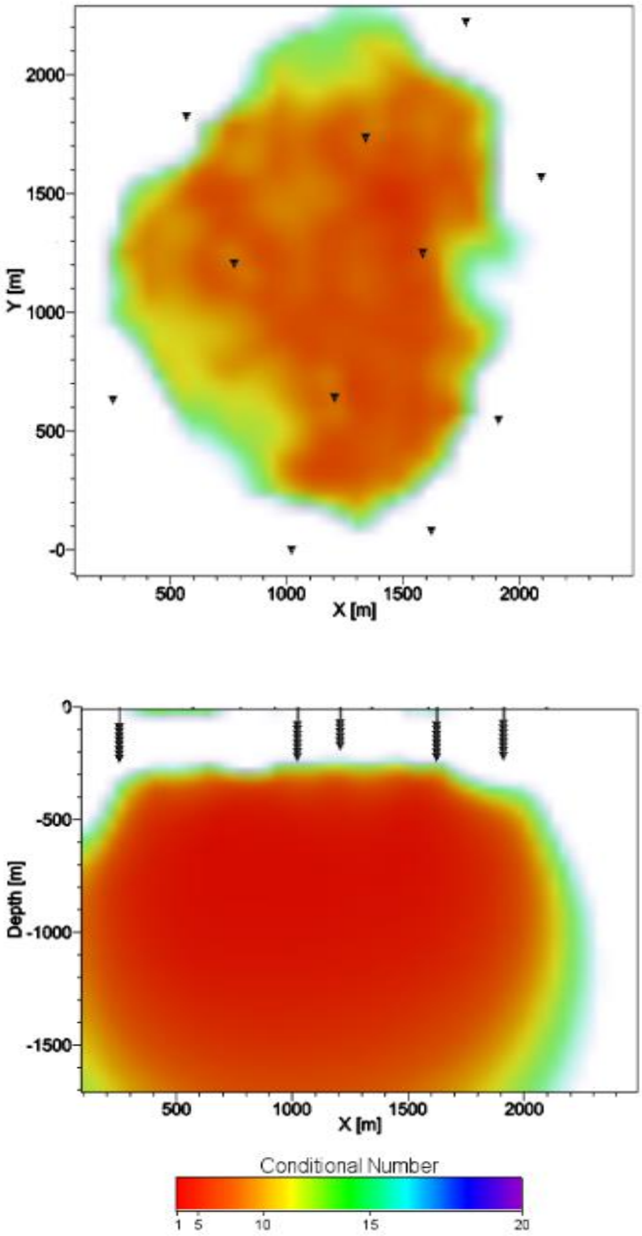

Figure 1.3: Horizontal and vertical cross-sections of condition numbers computed for receiver array installed in shallow boreholes, represented by the black upside-down triangles projected to the plane. The condition numbers are shown at the horizontal (at the depth 330 m) and the vertical cross-sections (Y=1100 m).

A better stability of the source mechanism inversion could be achieved by using S-wave amplitudes on the shallow borehole array. However, using all P-wave arrivals for all the receivers in the shallow reservoir is likely to be too optimistic. Mahrooqi *et al*. (2013) observed useful signal only on a few neighboring wells (usually two). In such a case, the source mechanism stability is very similar to our second tested array – the dual monitoring borehole array. Using both P- and S-wave arrivals for two near boreholes may solve the problem with events located in the depths of receivers close to the wells. However, the stability of the inversion from two boreholes only has limitations and the best quality of inversion is achieved between the wells, 45° from the plane containing both wells. Thus, a reliable inversion requires the monitoring boreholes to be drilled closer to each other than in the case presented by Mahrooqi *et al*. (2013). A possible improvement for such a shallow reservoir could be adding (near-)surface stations, but these stations would be probably noisy. Another option would be extending the monitoring wells to a greater depth and making the monitoring arrays longer to improve the focal sphere receiver coverage.

1.4 Discussion and conclusions

We computed 3D distributions of condition numbers for three commonly used types of receiver arrays in microseismic monitoring. Note that this methodology is not dependent on the actual acquired data but is derived from synthetic medium model (equation 1.1 and 1.2), we assume homogenous isotropic medium for simplicity. Each of the three tested arrays provides specific result, although there are some similarities too. The surface array (first tested array) has low condition numbers (i.e. good invertability) similarly to the (multi-)array of shallow boreholes (third tested array), at depths comparable with the distance between the center of the array and the most distant receiver. High condition numbers are found around and between the wells for both, dual-borehole array (second tested array) and array of shallow boreholes, indicating low stability of inverted full moment tensor source mechanisms.

In this study, we assumed the best possible scenario: all amplitudes are contributing on all stations, i.e., P-wave for surface and shallow borehole array and P- and S-waves for dual borehole array. Considering low magnitude microseismic events and a realistic signal-to-noise ratio, we might not be able to correctly pick the amplitudes at each receiver and this would deteriorate real resolvability of moment tensor. For example, Mahrooqi *et al*. (2013) did not have sufficient signal-to-noise ratio to reliably pick the amplitudes on all the receivers and used data from only limited number of wells. The surface monitoring star-like array of Anikiev et al. (2014) and the dual borehole monitoring array of Jechumtálová *et al*. (2016) detected events which had sufficient signal on most of the receivers.

Our study clearly shows that there are places where some arrays do not allow to invert stable full moment tensor even in the best scenario situation. The ability of using all receivers is not a major problem for a dense surface array, where are hundreds of receivers, but it is critical for borehole arrays. There it is necessary to record reliable P- and S-wave amplitudes on as many receivers as possible to achieve as large as possible solid angle (an angle given by the aperture of receiver array, as viewed from the source location) resulting in a stable source mechanism inversion. We remark also that the velocity model affects more severely the borehole arrays, where guided and head waves may interfere with reflected and direct arrival waves, and anisotropy affects severely S-waves.

The source mechanism inversion can be made more stable by adding more optimally placed stations, using S-wave amplitudes for surface or near surface receivers or adding another input parameter constraining the mechanism such as SH/P or SV/P amplitude ratios.

The key factor for the source mechanisms inversion is the solid angle or in other words the focal sphere coverage. For weak events in records with low signal-to-noise ratio recorded only by the downhole arrays, it is important to record arriving waves in the largest possible solid angle (e.g., Eaton and Forouhideh, 2011). For strong events, a large solid angle is achievable with (near-)surface arrays.

The presented results neglect the effects of velocity and attenuation model. They show where the moment tensor inversions are (un-)stable due to a receiver configuration. Therefore, the results in this study in some sense represent the most optimistic estimate we can achieve.

Chapter 2

Stability of source mechanisms inverted from P-wave amplitude microseismic monitoring data acquired at the surface

Published in *Geophysical Prospecting*, in 2014,
Volume 62, 475-490. doi:10.1111/1365-2478.12107

František Staněk[1,2], Leo Eisner[1] and Tijmen Jan Moser[3]

[1] *Czech Academy of Sciences, Institute of Rock Structure and Mechanics, Dept. of Seismotectonics, Prague, Czech Republic*
[2] *Charles University, Faculty of Mathematics and Physics, Dept. of Geophysics, Prague, Czech Republic*
[3] *Moser Geophysical Services, Den Haag, The Netherlands*

We study the stability of source mechanisms inverted from data acquired at the surface and near surface monitoring arrays. The study is focused on P-wave data acquired on vertical components, as this is the most common type of acquisition. We apply ray modelling on three models: a fully homogeneous isotropic model, a laterally homogeneous isotropic model and a laterally homogeneous anisotropic model to simulate three commonly used models in inversion. We use geometries of real arrays, one consisting of surface receivers and one consisting of “buried” geophones at near surface. The stability was tested for two of the frequently observed source mechanisms: strike-slip and dip-slip and was evaluated by comparing the parameters of correct and inverted mechanisms. We assume these double-couple source mechanisms and use quantitatively the inversion allowing non-double-couple components to measure stability of the inversion. To test the robustness, we inverted synthetic amplitudes computed for laterally homogeneous isotropic model and contaminated with noise using a fully homogeneous model in the inversion. Analogously amplitudes computed in laterally homogeneous anisotropic model were inverted in all three models. We show that a star-like

surface acquisition array provides very stable inversion up to very high level of noise in data. Furthermore, we revealed that strike-slip inversion is more stable than dip-slip inversion for the receiver geometries considered here. We show that noise and incorrect velocity model may result in narrow bands of source mechanisms in Hudson's plots.

2.1 Introduction

Gas production in North America is being significantly complemented by unconventional production from tight sands, shales and coal beds. The unconventional gas production is enabled by a stimulation technique called hydraulic fracturing. This process typically creates (micro)earthquakes with a magnitude range from -3 to -1 (Duncan 2005). However sometimes it can induce stronger events with larger magnitudes (Eisner *et al.* 2011). Microseismic point sets may determine geometry of the activated fractures, and recently advanced characterization of induced microseismic events, such as source mechanisms, is used for further analysis of stimulated reservoir. The source mechanisms can constrain Discrete Fracture Networks (Williams-Stroud *et al.* 2010) or can also be used to characterize shear and tensile events indicating fracture openings (Baig and Urbancic 2010).

In shale gas, microseismic monitoring is carried out by receivers deployed at the surface, near surface or by receivers in monitoring boreholes. While numerous studies have investigated source mechanisms inverted from datasets acquired in boreholes (e.g. Rutledge and Phillips 2003, Vavryčuk 2007) much less attention was paid to inversion of data acquired at surface, particularly in geometries used in oil and gas industry. This study investigates the stability of inversion of (near)surface array based microseismic monitoring data for frequently observed source mechanisms in microseismic monitoring (in most tectonic settings), i.e. strike-slip and dip-slip mechanisms (Rutledge and Philips 2003, Eisner *et al.* 2010). Šílený (2009) studied the stability of source mechanisms from microseismic events inverted from data recorded on a very sparse surface network (used in geothermal industry). He studied effects of receiver distribution, velocity model and location accuracy and showed that with a good receiver distribution the velocity model has a strong influence on the stability of the inversion (more than uncertainty in the location). Heterogeneity and anisotropy affect the trajectory of rays. Hence the source mechanism inversion may result in a systematic bias due to an incorrect velocity model. We investigate sensitivity of the inverted source mechanisms in fixed location on different velocity models and dense receiver distributions used in oil and gas industry. Furthermore, Eaton and Forouhideh (2011) showed that beside the influence of receiver geometry, the presence of random noise has a significant effect on stability of inversion. So, we also add sensitivity to various noise contamination of the data (various signal-to-noise ratios (SNR), as the noise is the main limitation in surface monitoring of microseismic events. Such a study is a necessary step in the understanding of the feasibility of location by migration algorithms instead of more commonly used pick and locate algorithms (see Duncan and Eisner 2010). Migration algorithms require polarization correction based on source mechanisms (e.g. Zhebel and Eisner 2012) and hence it is important to understand if the correct source mechanisms can be recovered from noise contaminated surface observations.

The field application was simulated by two common types of receiver geometries: a star-like geometry (also known as FracStar[i]) and array of shallow boreholes (also known as BuriedArray[i]) and real velocity models from the localities where they are/were installed. The goal of this study is to investigate the stability of source mechanisms inverted from the sparse network of shallow borehole receivers over a large area relative to a dense array of receivers in a star-like geometry over smaller area at the surface.

2.2 Methodology

We use ray modelling for both the forward and inverse problem. Synthetic amplitudes of P-waves are computed from a point source to an array of vertical component receivers due to two types of source mechanisms. Then we invert amplitudes contaminated with noise in different (correct and incorrect) models and compare the result with source mechanism input in forward modelling.

Forward modelling of propagation effects

The forward modelling is carried out as a wave front tracing and includes kinematic and dynamic ray tracing. Here, we describe our implementation of wave front tracing specially tailored for microseismic monitoring. For details on ray theory

---

[i] Registered trademark

and wave front tracing we refer to Červený (2001), Moser and Červený (2007), Vinje *et al.* (1996a,b) and Lambaré, Lucio and Hanyga (1996). Both kinematic and dynamic ray tracing are formulated in terms of a Hamiltonian function. One of the advantages of the Hamiltonian formulation is that the model definition and ray tracing functionality can be fully separated.

For a single ray, kinematic ray tracing solves the kinematic ray equations which results in the ray trajectory and travel time and slowness vector along it. Dynamic ray tracing consists in the solution of an additional system of linear ordinary differential equations along the ray and is used to determine the geometrical spreading, and amplitude along the ray. Additionally, it provides geometrical derivatives which are useful for many applications. The Hamiltonian formalism is suitable for dynamic ray tracing when implemented in terms of the 6x6 propagator matrix in Cartesian coordinates (Moser and Červený 2007).

Wave front tracing consists of computing rays in all directions from an initial source point, organized in such a way that the ray density along wave fronts is uniform over the model. This is done by re-interpolating rays at each computation step. The advantage of such an organization of the ray computations is that at each step the capture of receiver points can be checked. If a receiver point is captured all necessary ray quantities (such as travel time, amplitude, etc.) are written to output for that point. In such a way, the otherwise notoriously difficult two-point ray-tracing problem is solved automatically. The wave front is allowed to fold over itself, thus automatically accounting for multivalued arrivals. The wave front tracing organization assumes a single source point and many receiver points; based on reciprocity, the source and receiver roles can be freely exchanged should this be desired.

The wave fronts are represented by triangulated surfaces. The initial wave front is a tetrahedron at the source point. Upon re-interpolating rays, each triangle exceeding a splitting threshold is subdivided into four smaller triangles. The splitting criterion is a combined distance and angle criterion - as soon as two neighboring rays are further apart or have directions differing more than pre-defined thresholds, a new ray is inserted and the corresponding triangles are subdivided into new smaller ones. In this way, by imposing an upper bound on the triangle size, a uniform accuracy over the whole model is ensured. At the same time, the computational effort of wave front tracing is inverse proportional to the triangle size.

At each step in the wave front propagation, the capture of a receiver point is checked between two consecutive wave fronts, by considering the prismatic ray cell consisting of an elementary ray triangle before and after the propagation step and subdividing it into three tetrahedra. For each of these tetrahedra an inside-test is performed for all receiver points, based on barycentric coordinates. If a receiver point is located within an elementary tetrahedron, the same barycentric coordinates are used for interpolation of the ray quantities of the elementary ray cell onto the receiver location. In addition, the 6×6 propagator matrix is used to compute the geometrical spreading and amplitude. For selected receiver points, the ray trajectory, which is not recomputed upon ray interpolation at triangle splitting, is re-constructed by tracing back to the source point.

The source-receiver acquisitions relevant for the microseismic monitoring are typically a single point source at a given depth location and a large number of receiver points irregularly located at the surface. The topography of the surface may be irregular as well, so that the receiver points have irregular elevations. As a result, the receiver capture for each elementary wave front triangle has to be organized in a way that all receiver points are checked for every triangle at each propagation step. This may pose a burden on the computational effort. However, by constructing a bounding box around all receiver points, the receiver capture check can be restricted to this box. Otherwise, owing to the limited number of sources computation time is not an important issue and accuracy of the computed ray quantities can be given a first priority. In this way, the wave front tracing for microseismic monitoring differs from other applications, where the receivers are located on a regular grid, but the number of source points can be very large (e.g. Green's functions computation for depth migration).

Velocity model description

The model is fully anisotropic with 21 elastic parameters and density, which may be smoothly spatially variable. Isotropy and vertical transverse isotropy (VTI) are treated as special cases handled within the same wave front tracing code. All elastic parameters and density are represented on uniform equidistant and rectangular three-dimensional grids of B-splines. The spacing of the grids is macroscopic, meaning that it adopts to model variations while satisfying the ray tracing validity conditions (length scale of model variations should be larger than the dominant seismic wavelength) and at the same time ensuring an optimal allocation of memory. Free surface boundary condition is applied to the dynamically computed amplitudes assuming flat free surface.

The velocity models are known to cause systematic biases in either locations or source mechanisms. To test influence of different velocity models we created three models for each receiver configuration under investigation: a fully homogeneous isotropic model (HIM), a laterally homogeneous isotropic model (1DIM) and a laterally homogeneous anisotropic model (1DAM). HIM is a test of extreme simplification of medium propagation sometimes used for inversion from surface monitoring networks (e.g. Eisner *et al.* 2010). The 1DIM reflects fundamental nature of inversion in sedimentary basins where current shale development is carried out: majority of these shale plays are in smoothly varied parts of the basin. The 1DAM reflects properties of VTI-type of anisotropy commonly observed in shale plays (e.g. Vernik 2008; Gei, Eisner and Suhadolc 2011). The HIM has the same average vertical velocity from the source depth to the surface as the other two models (1DIM and 1DAM).

The smoothed velocity models (Figure 2.1) are derived from active seismic data. For an array of shallow boreholes, we used a smoothed version of a 17-layered velocity profile of Zhang *et al.* (2013). The effective velocity for source depth of 4000 m is 3506 m/s. For a star-like array we took 1D velocity model composed of 7 layers with increasing velocity with depth from Gei, Eisner and Suhadolc (2011). The effective P-wave velocity of equivalent HIM from the source depth of 2100 m is 3187 m/s.

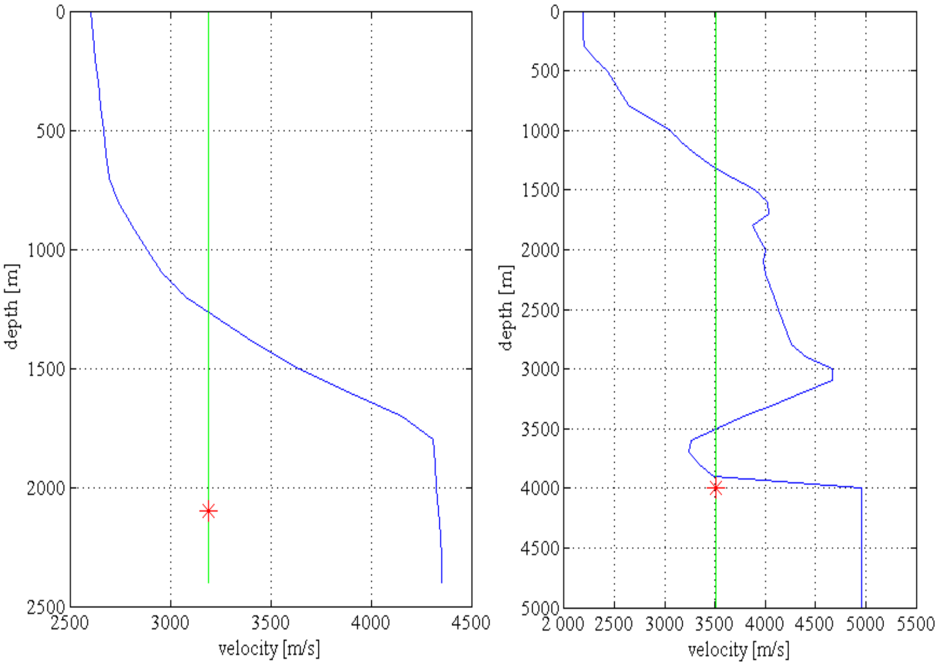

Figure 2.1: Smoothed 1D velocity profiles - on the left for a star-like array and on the right for a shallow borehole array. The blue line is for a laterally homogeneous isotropic model (1DIM) and a laterally homogeneous anisotropic model (1DAM). The green line represents the constant velocity for a fully homogeneous model (HIM). Red asterisk shows the position of source.

We assume a constant density 2700 kg/m^3 and V_P to V_S ratio 1.7 although these parameters do not significantly affect the source mechanism inversion from P-waves only. The effect of realistically variable V_P to V_S ratio is less than ten times smaller than effects of other parameters considered in this study as this ratio only affects transmission coefficients and free surface boundary condition. For example, a variation of the free surface boundary condition from vertical (i.e. 0°) to 80° impact angle is less than 30% of the amplitude for V_P to V_S ratios changing from 1.6 to 2 while amplitude variation due to noise variation is up to 1000% in this study.

The 1DAM has constant (effective) VTI parameters with vertical axis of symmetry. As we use only P-waves we compute corresponding Thomsen parameters δ and ε (Thomsen 2002) to characterize this weak anisotropy. We use the values δ = 0.061 and ε = 0.152 taken from Zhang *et al.* (2013) for both models.

Source and receiver geometries

The first receiver configuration for testing is a star-like array of less than thousand geophones. The array is used in a surface layout where high random noise is compensated by stacking of traces improving SNR as the square root of the number of receivers, i.e. approximately a factor of 30. It consists of arms spread out along radial lines around the wellhead which is the main source of noise. We use the geometry and layout from a real hydraulic fracture monitoring (Figure 2.2). There are 10 lines with a total of 911 vertical geophones. The number of receivers per arm varies between 54 and 122 and the average receiver separation is 23 m, which means that this configuration covers approximately 25 km^2.

The second array consists of receivers in shallow boreholes in which the smaller number of receivers is compensated by higher SNR in shallow boreholes less than 100 m deep. In our case, this permanent configuration consists of 99 receivers covering an area of about 100 km^2 - it has approximately ten times fewer receivers and covers four times the area as the star-like geometry.

The tested horizontal source position was near the centre of the receiver arrays and the depths similar to the stimulated intervals. For a shallow borehole array source position was at [X, Y, Z] = [5000 m, 5000 m, 4000 m] and for a star-like configuration it was at [X, Y, Z] = [2500 m, 2500 m, 2100 m]. This placement guarantees approximately 1:1 receiver offset to depth ratio as recommended for any surface monitoring (e.g. Duncan and Eisner 2010).

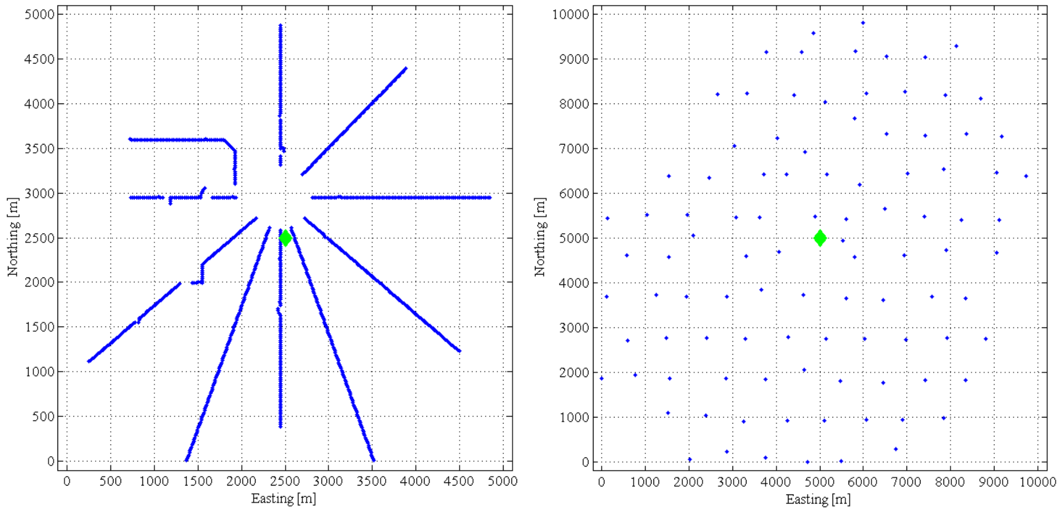

Figure 2.2: On the left is a star-like array and on the right is a shallow borehole array. The blue dots represent receivers, green diamond is epicenter.

Forward modelling of source mechanism

Using the above described ray tracing we compute synthetic P-wave amplitudes on vertical components as we simulate 1C vertical geophones deployed at the surface or shallow boreholes. For the star-like configuration we include free surface boundary condition in the dynamic ray tracing. According to representation theorem for a point source at ξ is particle displacement amplitude $u_n(x,t)$ given by a derivative of Green function and moment tensor:

$$u_n(x,t) = M_{pq}(\zeta,\tau) * G_{np,q}(\zeta,x,\tau,t) \tag{2.1}$$

The derivative of the green function is calculated using dynamic ray-tracing in the selected models between point source at ζ and receiver at x (Aki and Richard 1980). τ represents time at the point source and t time at receiver. We evaluate moment tensor $M_{pq}(\xi,\tau)$ from strike, dip and rake angles and scalar moment (page 117-118, Aki and Richards 1980). The temporal dependency of source time function (i.e. dependency of $M_{pq}(\xi,\tau)$ on source time τ) is assumed to be a delta function given that our microseismic sources have corner frequency above 100 Hz and surface observations are dominated by frequencies of 50 Hz (Duncan and Eisner 2010). In this study, we set seismic moment of events to 3.9×10^7 N.m, corresponding to approximately moment magnitude -1. However, as we set level of noise relative to computed synthetic amplitudes, the tests are valid for arbitrary magnitudes and the chosen moment magnitude value of -1 serves only for understanding how accurate any magnitude inversion is. Propagation effects are represented in equation (2.1) by the derivative of Green function, $G_{np,q}(\xi,x,\tau,t)$, which is computed from parameters of rays, such as slowness vectors in source and in receivers, polarizations, geometrical spreading, density, and velocity models.

As an output of the forward modelling we obtain synthetic amplitudes computed for the selected receiver configuration with polarity and size corresponding with the radiation pattern of source mechanism and also influenced by the velocity model in which the rays were modelled. We assume a homogeneous isotropic medium in the vicinity of source location even in case of 1DAM although we are aware this is to some extend a simplification. However, the tested source mechanisms have principal axes oriented along horizontal and vertical directions and hence we do not expect that the VTI anisotropy in the source region plays a significant role (see Vavryčuk 2005).

Using the above process, we computed 12 sets of noise free synthetic amplitudes: one set for each combination of receiver configuration, source mechanism and model. Noise free synthetic amplitudes for strike-slip and dip-slip source mechanisms in HIM are shown in Figure 3. The dip-slip mechanism is represented by dip of 90^o, strike 0^o, and rake 90^o, the strike-slip mechanism is represented by dip 90°, strike 0°, and rake 0°. We have chosen these two mechanisms as representative of seismicity induced during the hydraulic fracturing in sedimentary basins. Strike-slip source mechanisms were found for example by Rutledge and Phillips (2003) in Cotton Valley and Droujinine, Oates and Ita (2011) in shale formation. Dip-slip events were observed for example by Robein *et al.* (2009) or Eisner *et al.* (2010). While this (and no other finite) choice of source mechanisms does not cover the entire spectrum of observed mechanisms of microseismic events, based on our experience we believe this choice is covering the most important types of induced microseismic events as it represents vertical fractures.

Modelling of the noise

Each array has specific noise properties. Furthermore, the main source of noise is surface waves propagating from the center of the array where the stimulation operations are carried out. In a star-like array the noise is correlated as receivers are relatively near each other. In a shallow borehole array the noise is not correlated between different shallow wells and is distributed more randomly (similar to ideal white noise). We create noise using the real and computed synthetic amplitudes by the following equation:

$$Noise = \frac{A_{real}}{mean(|A_{real}|)} \cdot mean(|A_{synthetic}|) \cdot NoiseLevel, \qquad (2.2)$$

where $A_{synthetic}$ is a set of computed amplitudes for the assumed source mechanism and A_{real} are amplitudes taken from real measured data on each receiver at a randomly chosen time. *NoiseLevel* is in this meaning reversed value of SNR. We tested 11 levels from 0 for data with no noise to 10 where the noise exceeding ten times the signal. The *Noise* is then added to the computed synthetic amplitudes:

$$A(NoiseLevel) = A_{synthetic} + Noise(NoiseLevel). \tag{2.3}$$

A more representative sampling of the characteristic noise is achieved by taking 50 realizations for each *NoiseLevel* for every source mechanism and model. Examples of noise amplitudes for both geometries and noisy amplitudes with *NoiseLevel 1* are shown in Figure 2.3.

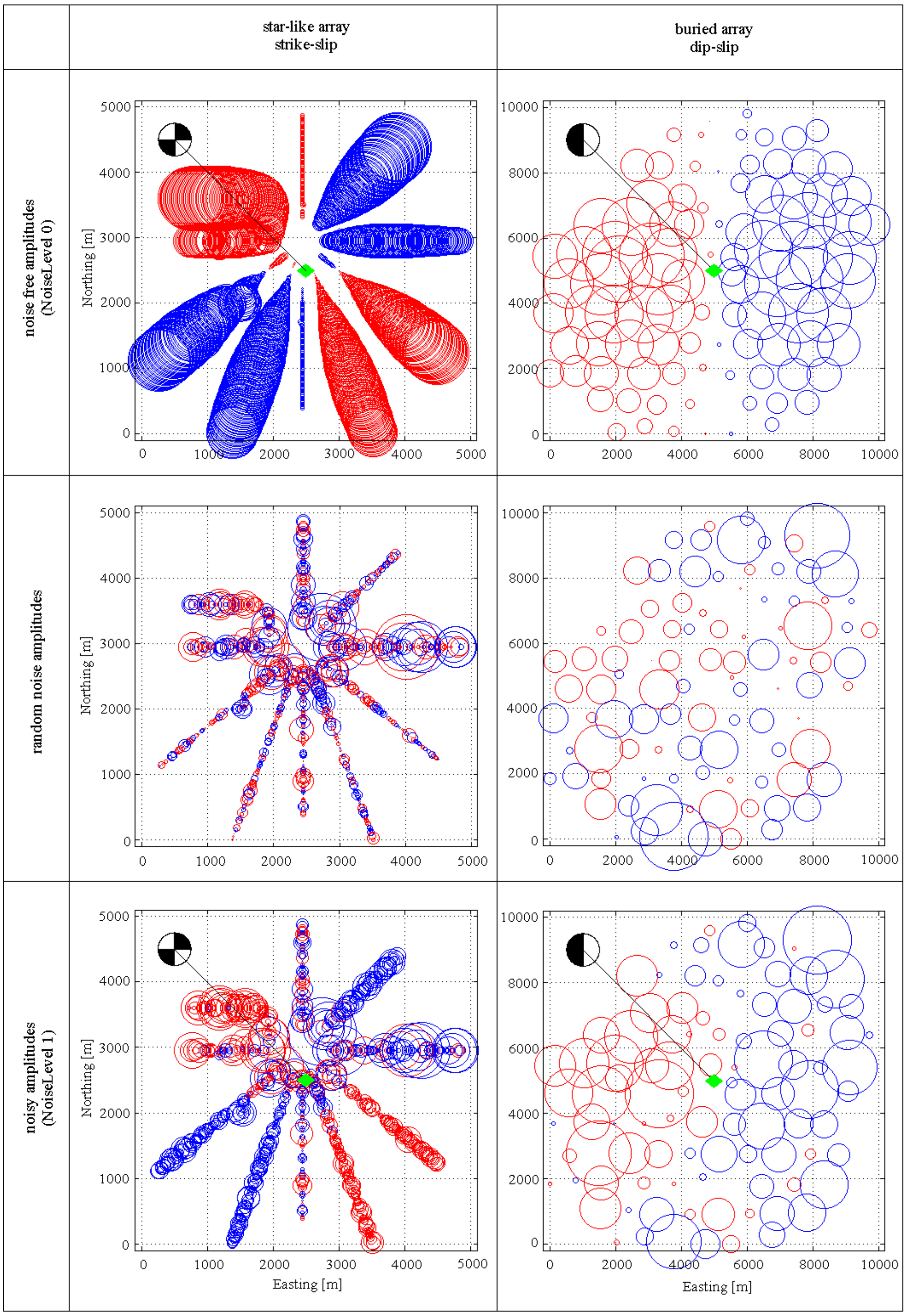

Figure 2.3: Noise-free synthetic amplitudes, random noise amplitudes and noisy amplitudes (i.e. sum of previous amplitude sets) with Noise Level 1 (SNR=1) for a strike-slip source mechanism monitored with star-like monitoring array (left) and for a dip-slip monitored by buried geophones (right) in a fully homogeneous model (HIM). A red and blue colored circle at each receiver position represents first motion down and up, respectively. The diameter of the circle is proportional to the amplitude. The Green diamond in the middle is epicenter. Focal mechanisms plots represent lower hemisphere projection.

Inversion of source mechanism and comparison

We use source mechanism inversion from the surface data based on a least squares inversion of the P-wave amplitudes on the vertical component. The moment tensor representing the source mechanism inverted from a point source relationship (2.1) for vertical components assuming source time delta function:

$$u_3(x) = M_{pq}(\zeta) G_{3p,q}(\zeta, x), \tag{2.4}$$

where $G_{3p,q}$ are vertical components of the Green's function derivative. Einstein's summation rule over p,q indexes applies. The linear equation (2.4) is inverted by least squares (Sipkin 1982):

$$u_3(x,t) = m_j(\zeta) g_{3j}(\zeta, x), \tag{2.5}$$

where m is a vector formed from 6 components of the moment tensor and g are modified Green functions to satisfy equation (2.4).

A general full moment tensor is obtained by least squares inversion:

$$m_i = \Gamma_{ij} \sum_x A(x) g_{j3}(\zeta, x), \tag{2.6}$$

where

$$\Gamma_{ij} = \left[\sum_x g_{3j}(\zeta, x) g_{3i}(\zeta, x) \right]^{-1} \tag{2.7}$$

is the inversion matrix, which can be characterized by condition number to estimate the quality of the inversion. The moment tensor components obtained by equation (2.6) are used to calculate least square misfit through equation for the full moment tensor:

$$L2 = \frac{\sqrt{\sum_x (A(x) - m_j(\zeta) g_{3j}(\zeta, x))^2}}{\sqrt{\sum_x A(x)^2}}. \tag{2.8}$$

Synthetic amplitudes computed for two pure shear source mechanisms (dip-slip and strike-slip) contaminated with variable levels and realizations of noise are inverted for testing stability of source mechanism. In the inversion, we use both the true (i.e. correct) as well as incorrect models. The amplitudes computed in 1DIM were inverted in 1DIM and HIM and amplitudes forwarded in 1DAM were inverted in all three models to simulate a real situation where the inversion model is usually simpler than the real medium.

The full moment tensor (MT) obtained from inversion is then decomposed into double-couple (DC), compensated linear vector dipole (CLVD) and isotropic (ISO) components (Hudson, Pearce and Roberts 1989). A match of polarity and size of amplitudes due to correct mechanisms and amplitudes corresponding to source mechanism from inversion is numerically represented by L2-misfit between these two amplitude sets. Finally, we also compute omega angle (Ω) as a difference between input and inverted orientation of the P-axis. This angle represents a maximal possible difference between dip, strike and rake angles of two mechanisms. In this way, we are able to quantitatively analyze the maximum error in determination of the fault plane orientations.

For each *NoiseLevel* the decomposition of the source mechanism (i.e. percentages of DC, CLVD and ISO), L2-misfits and omega angles are averaged over 50 realizations to obtain representative behavior for expected *NoiseLevel*.

We study changes in parameters relative to the *NoiseLevel* shown in Figure 2.4a,b, 2.5, and 2.6. Both input source mechanisms are pure shear (pure DC). Hence any non-shear components, higher L2-misfit or Ω greater than 0 are due to incorrect inversion, i.e. mismodeling or/and noise.

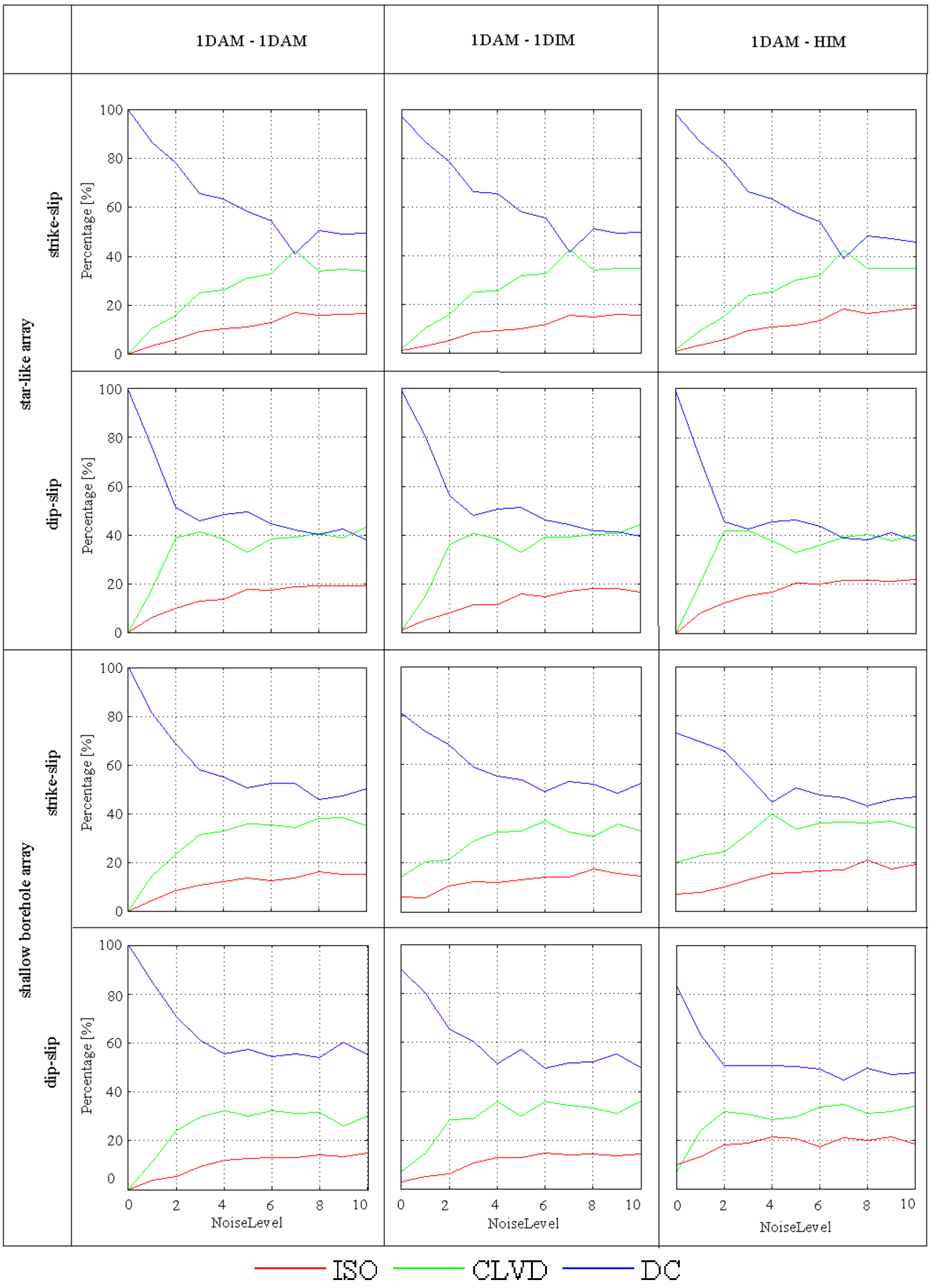

Figure 2.4a: Results of decomposition of mechanisms inverted from amplitudes computed in a laterally homogeneous anisotropic model (1DAM) for both arrays. The rows correspond to a star-like array (top two rows) and shallow borehole array (bottom two rows) for two tested source mechanisms. Left column plots are results of inversion in a true model (1DAM), central column is the result of inversion in a laterally homogeneous isotropic model (1DIM) and right column plots are results using fully homogenous isotropic model (HIM).

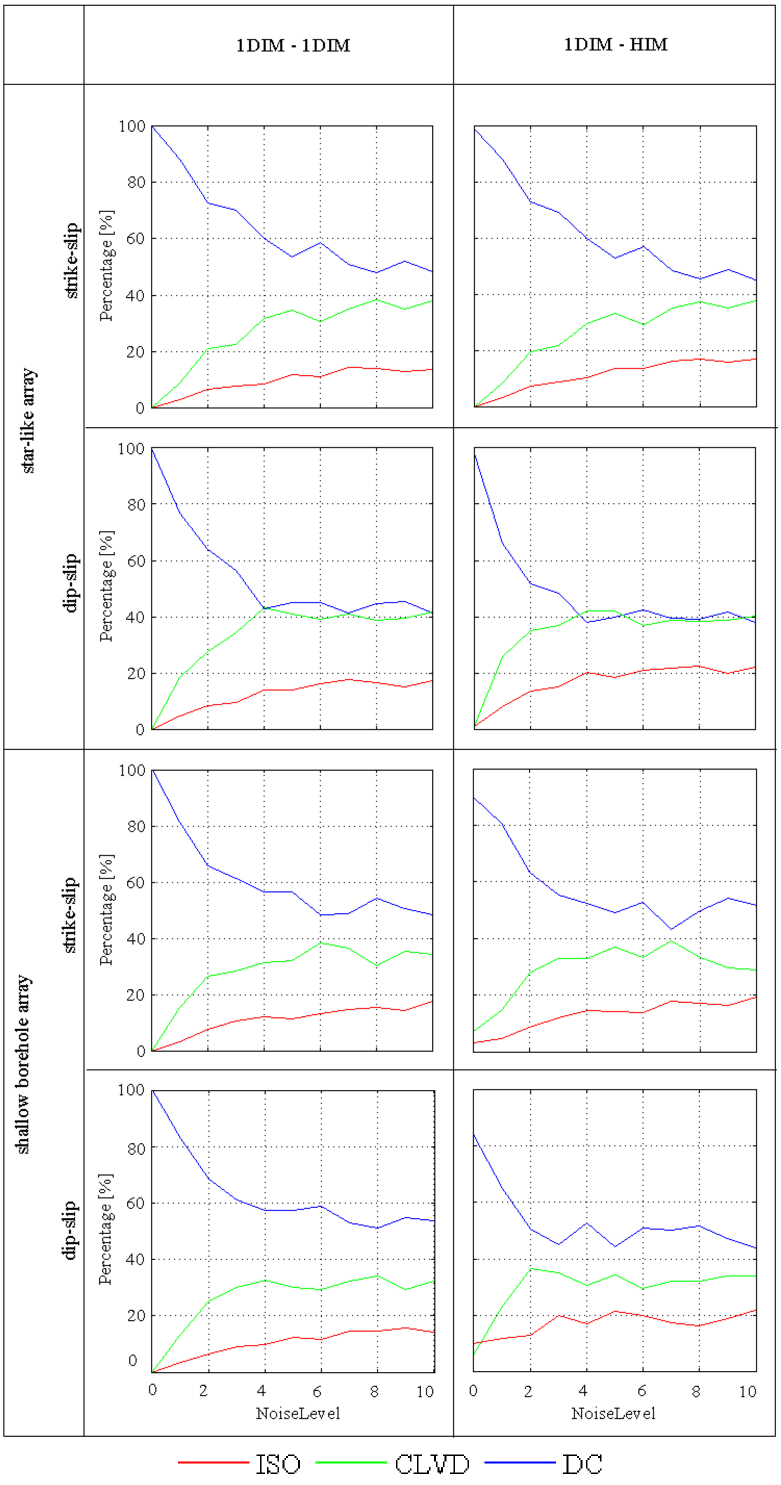

Figure 2.4b: Results of decomposition of mechanisms inverted from amplitudes computed in a laterally homogeneous isotropic model (1DIM) for both arrays. The rows correspond to a star-like array (top two rows) and shallow borehole array (bottom two rows) for two tested source mechanisms. Left column plots are results of an inversion in a true model (1DIM) and right column plots are the results using a fully homogenous isotropic model (HIM).

2.3 Results of synthetic tests

We get the true 100% DC component of the inverted mechanism only if we invert noise free amplitudes (*NoiseLevel* is 0) in a correct model. When we use an incorrect (simpler) model the non-shear components are always present. With a star-like configuration the velocity model causes only small non-DC components (only 1-3%) however for an array of shallow boreholes the spurious non-DC components are higher (up to 27% with noise-free data) as it is shown in Figure 2.4a,b.

The increasing noise level in the data causes a decrease of the DC component close to 50% independently on the model and mechanism and increase of the CLVD and ISO components with the CLVD component growing approximately two times faster than the ISO component. Note that in order to pick the source mechanism in raw data the *NoiseLevel* defined in this study must be smaller than 1. Hence our results show that for such *NoiseLevels* the inverted mechanism of pure shear should exceed a critical value 75% of DC component if a correct velocity model is used. The higher *NoiseLevels* considered in our study are important for simultaneous inversion of source mechanisms and location by migration-type algorithms (e.g. Zhebel and Eisner 2012). The deterioration from pure shear source occurs at a different *NoiseLevel* for different mechanisms and arrays. This is consistent with Eaton and Forouhideh (2011) who also observed increased ISO and CLVD components with increasing noise with inversion of the surface array. But the dependency of the inversion result on the source mechanism was not previously known (at least in the oil and gas industry).

As we can see in Figure 2.4a,b, for pure shear source input (100% DC) and inversion in a correct model (1DAM-1DAM or 1DIM-1DIM), the inverted DC component for dip-slip decreases faster with increasing *NoiseLevel* than for strike-slip. It means that the dip-slip source mechanism is more sensitive to noise than the strike-slip source mechanism. However, for buried receivers there is no major difference as for a star-like array.

The velocity model heterogeneity and anisotropy is significant only for *NoiseLevel* up to 2 while for higher *NoiseLevels* the error in obtained source mechanism is dominated mainly by the noise. This means that noise plays key role for the *NoiseLevels* exceeding 2 and effects of incorrect velocity are not important at those *NoiseLevels*.

The L2-misfit values measuring average difference of observed amplitudes and output amplitude sets computed as responses of inverted moment tensors are for star-like array practically independent of correctness of velocity model. The curves in upper part of Figure 2.5 show very fast increase from 0% (for inverted noise free amplitudes in a correct model) to more than 80% misfit already for *NoiseLevel* 1 and then slower increase to misfits close to 100%. For buried receivers, we observe higher dependency on used velocity model, when the difference between correct and incorrect model cause significant error (up to 67%) even for amplitudes without any noise. With increasing noise, the curves are gathering, correctness of used model is losing influence and results are controlled by the level of noise.

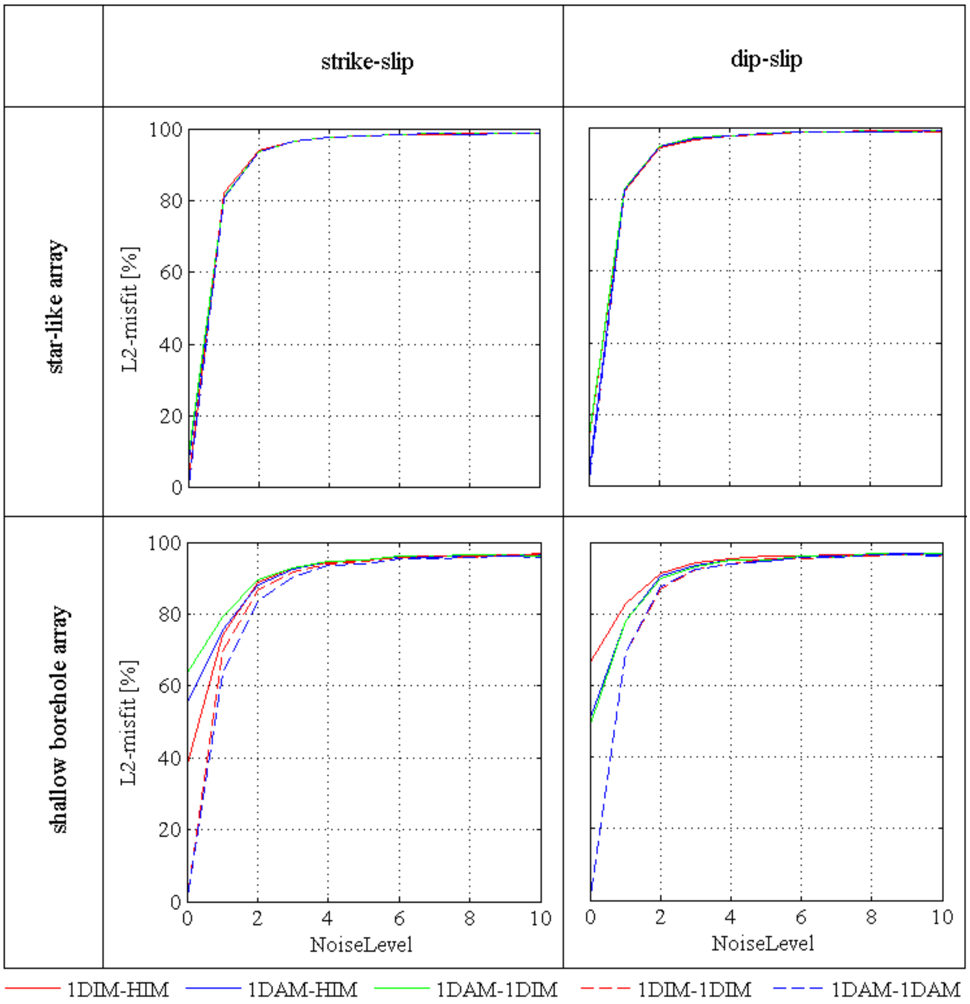

Figure 2.5: L2-misfits between input amplitude set and amplitude set representing inverted moment tensor computed for strike-slip and dip-slip monitored by star-like array and array of shallow boreholes.

The omega angles (Ω) increase with increasing noise as obtained fault planes start to significantly deviate from correct ones. The lowest values are obtained by inversion for a strike-slip with star-like array (Figure 2.6). With the same array for dip-slip, Ω grows roughly two times faster to 50° at *NoiseLevel* 10. With an array of shallow boreholes, we get higher Ω for strike-slip in comparison with Ω obtained with star-like array. The Ω angles of dip-slip inverted from amplitudes acquired with buried receivers are more sensitive to velocity model. However, the effect of neglecting anisotropy causes no major errors in Ω (i.e. orientations of the fault planes). Differences between using correct and simpler (incorrect) model are maximally around 10°, as observed for combination of dip-slip and shallow boreholes array in low *NoiseLevels*.

Finally, we show moment tensors in so called Hudson's diagram (Hudson, Pearce and Rogers 1989) showing contribution of decomposition components in an alternative representation from Figure 2.4, including signs of the inverted CLVD and VOL components. For the various tests carried above we observe a narrow trends of source types caused by the presence of noise or/and using simpler model. Figure 3.7 shows representative plots with the cloud of 50 mechanisms has clearly visible main tendency to grow from the centre of the diagrams (correct position for pure DC) in narrow trends between positive or negative CLVD and linear vector dipole. This trend is caused by the CLVD components increasing with noise faster than ISO component.

Generally, with higher random noise level the clouds of inverted mechanisms expand to other directions and become more scattered, however, in case of strike-slip and star-like array (previously noted as most stable combination) the mechanisms contaminated by noise or incorrect model are grouped around narrow trends and it would be easy to imagine that such grouping is interpreted as signal in the data (see for example Figure 2.8). These effects can play important role in interpretation of source mechanisms inverted from real data (e.g. Baig and Urbancic 2010) where the cloud of mechanisms might look similar to presented plots in our study (Figures 2.7 and 2.8). However, recall that the source mechanism in this study is the pure double-couple source contaminated by random noise and/or using incorrect model and all the non-shear components are false. Dip-slip mechanisms are the inverted mechanisms more scattered than for strike-slip mechanisms in the Hudson's plot, consistent with previous observation that strike-slips are more stable.

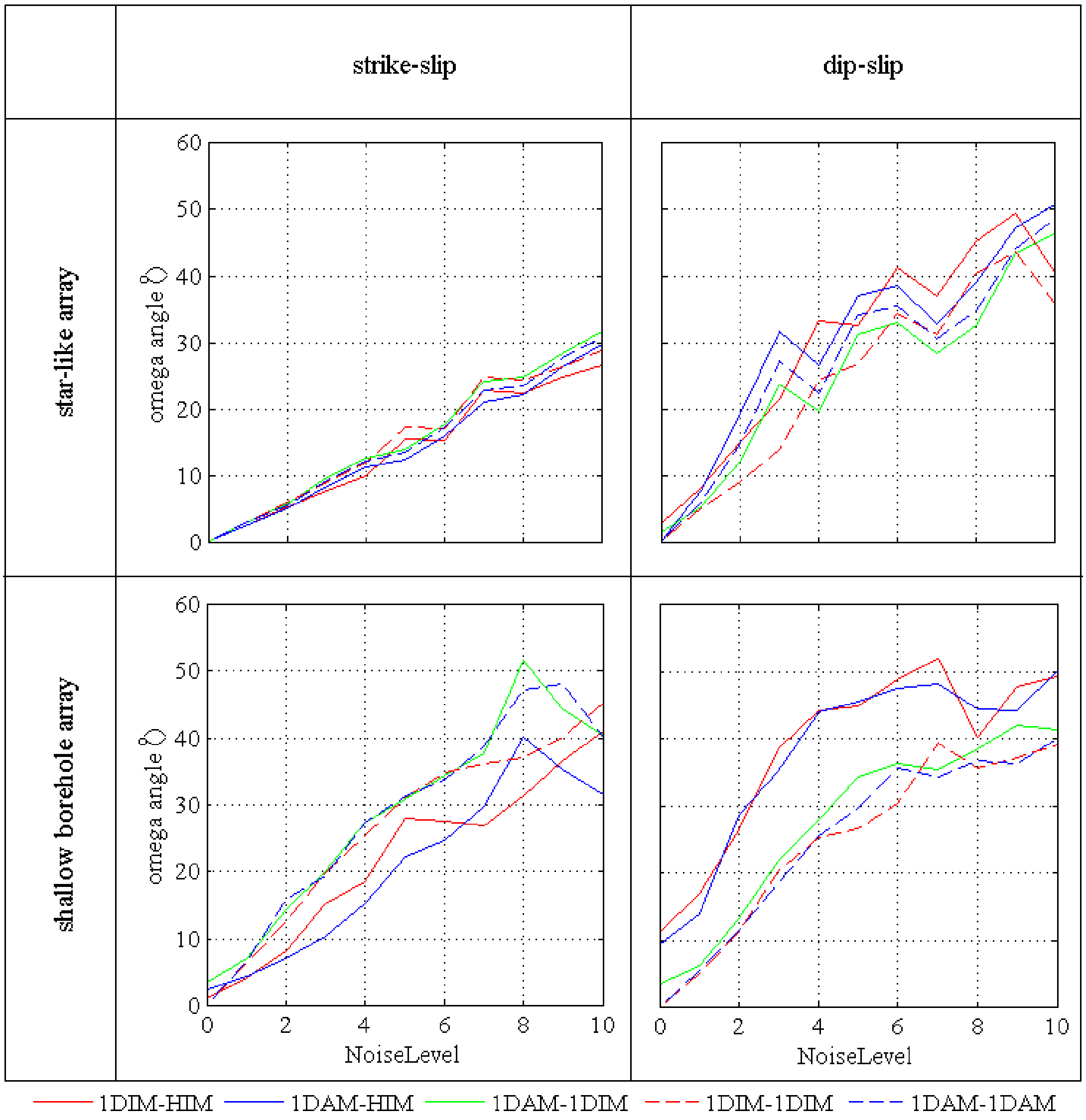

Figure 2.6: Omega angles computed as a difference between input and inverted orientation of the P-axis showing the maximum possible deviation of strike, rake or dip for strike-slip and dip-slip mechanisms inverted from amplitudes acquired with a star-like array and shallow borehole array. The type and colour of lines indicate the input and inverse models as explained in the legend.

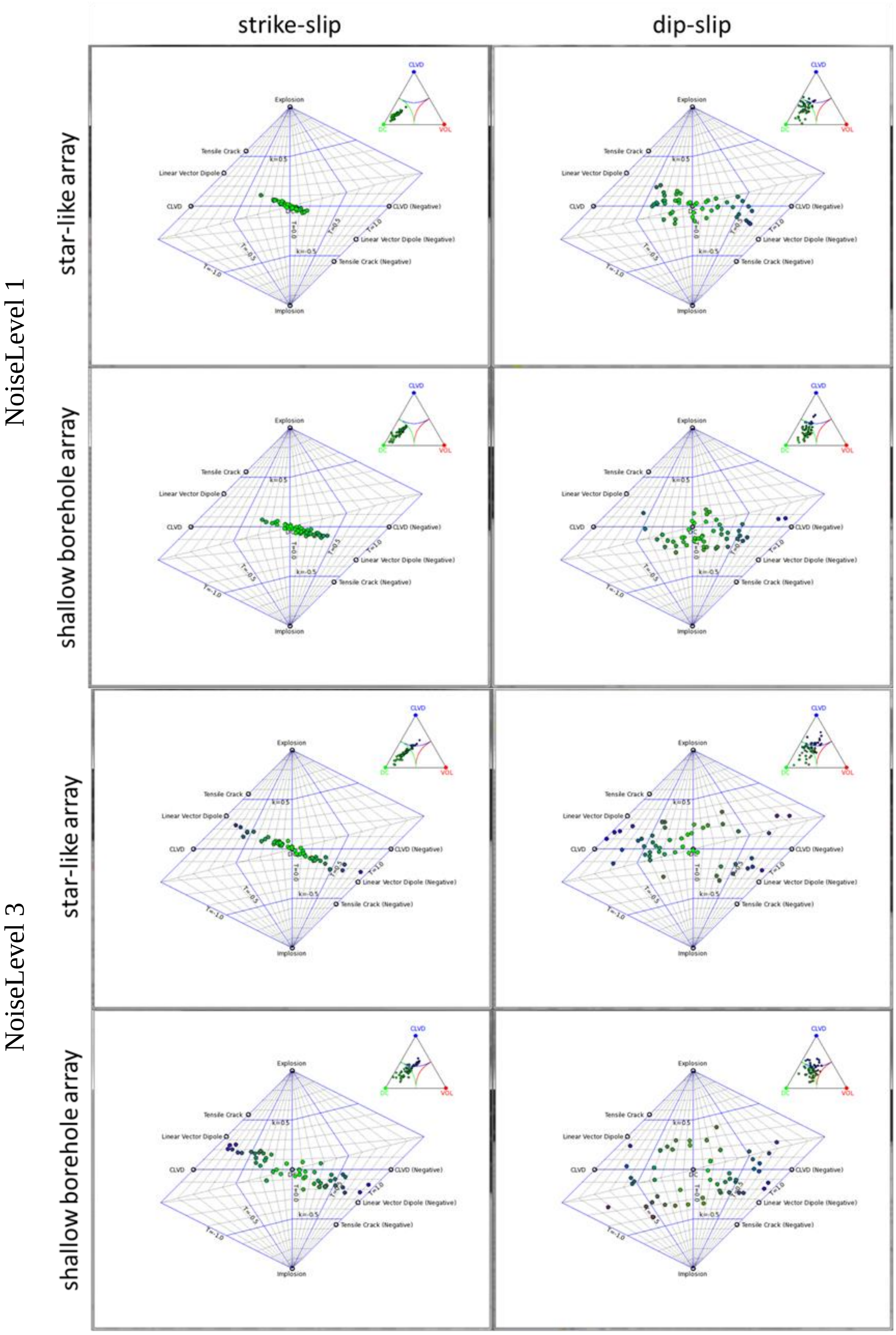

Figure 2.7: Source-type diagrams with 50 source mechanisms inverted from amplitudes computed for two pure shear source mechanism (strike-slip or dip-slip) and two types of array (star-like or shallow borehole). Amplitudes were modelled in 1DIM, contaminated with various realizations of noise with *NoiseLevel* 1 and 3 and inverted in simpler model HIM.

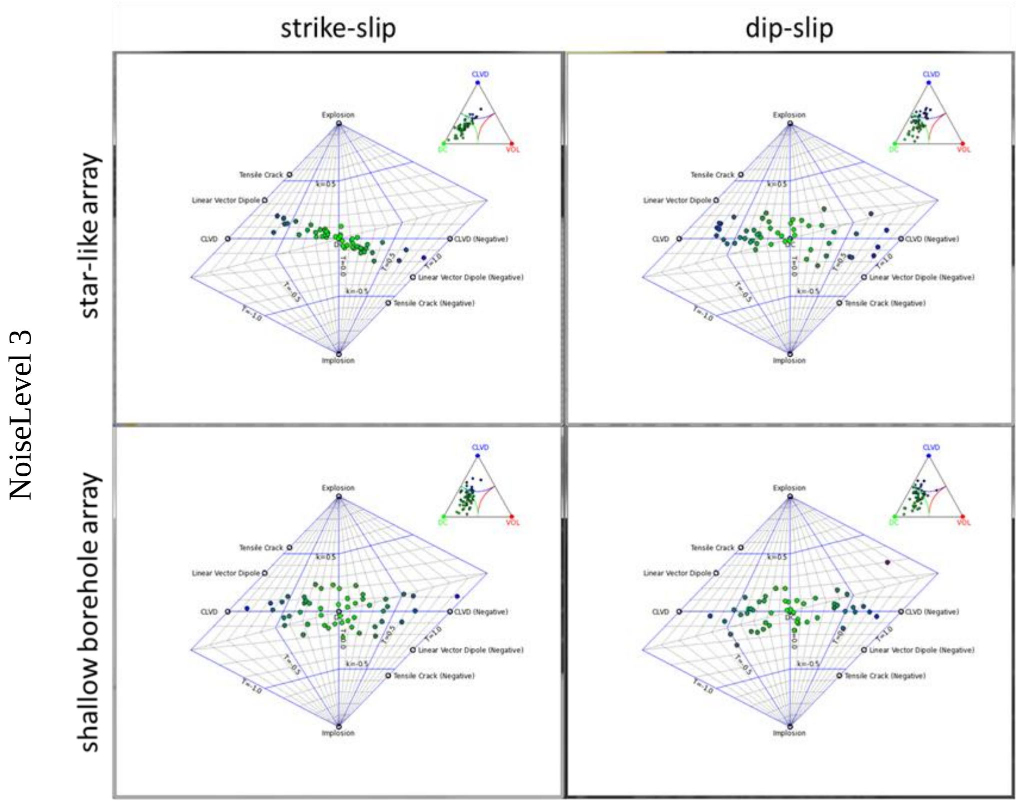

Figure 2.8: Source-type diagrams with 50 source mechanisms inverted from amplitudes computed for two pure shear source mechanism (strike-slip or dip-slip) and two types of array (star-like or shallow borehole). Amplitudes were modelled in 1DIM, contaminated with various realizations of noise with *NoiseLevel* 3 and inverted in correct model 1DIM.

2.4 Conclusions

This study shows the reliability of inverted source mechanisms from synthetic amplitudes computed for two configurations used in oil and gas industry. While the coverage of receivers is very good in both geometries the use of only P-waves on vertical components, correctness of the velocity model and noise limit the reliability of the source mechanism inversion. An interesting result is the dependency of inversion on source mechanism itself, i.e. the accuracy of the inverted mechanism is not simply described by one (condition) number for different source types. The differences between two receiver geometries are somewhat difficult to judge as velocity models and source locations differed between the configurations. While we could use the same models, we preferred to test real velocities appropriate for each location as these models will be used for inversion of observed microseismicity.

The most stable inversion from P-wave amplitudes is a strike-slip mechanism observed with a star-like array. We obtained very high values (approximately 80%) of the inverted DC component up to *NoiseLevel* 2 (corresponding to approximately SNR of 0.5) and the smallest of omega angles (Ω) independently on correctness of model generally consistent with previous study of Šílený (2009) and Eaton and Forouhideh (2011). The worst results are obtained for dip-slip mechanisms inverted from amplitudes monitored with an array of shallow boreholes neglecting the layered structure (i.e. inversion in homogenous isotropic medium from either layered isotropic medium or layered anisotropic medium).

Changes caused by neglecting anisotropy in propagation are smaller than the effect of neglecting velocity structure. The robustness of the inverted source mechanism for star-like configuration with respect to the velocity model is probably due to summing over a large number of geophones at multiple azimuths and offsets. Source mechanism inversion with an array of shallow boreholes configuration is more sensitive to the correctness of velocity model as well as presence of noise than the star-like configuration as we use fewer receivers deployed on a larger area.

Finally, Hudson's plots show that certain combinations of noise levels and/or simplifications in model may result in linear trends in obtained source mechanisms seemingly indicating some significant information related to the source. However, we show that these trends are purely artificial resulting from either noise or model errors. Hence, we recommend carrying out similar sensitivity study before interpreting Hudson's plots.

Chapter 3

Joint location and source mechanism inversion of microseismic events: benchmarking on seismicity induced by hydraulic fracturing

Published in *Geophysical Journal International*, in 2014,
Volume 198, No. 1, 249-258. doi:10.1093/gji/ggu126

Denis Anikiev[1], Jan Valenta[2], František Staněk[2,3] and Leo Eisner[2]

[1] *Saint Petersburg State University, Dept. of Earth Physics, Faculty of Physics, Saint Petersburg, Russian Federation*
[2] *Czech Academy of Sciences, Institute of Rock Structure and Mechanics, Dept. of Seismotectonics, Prague, Czech Republic*
[3] *Charles University, Faculty of Mathematics and Physics, Dept. of Geophysics, Prague, Czech Republic*

Seismic monitoring can greatly benefit from imaging events with a low signal-to-noise ratio (SNR) as the number of the events with a low signal grows exponentially. One way to detect weaker events is improvement of a SNR by migration-type stacking of waveforms from multiple stations. We have developed a new method of location of seismic events that involves stacking of seismic phases and amplitudes along diffraction traveltime curves to suppress noise and detect seismic events with a SNR lower than that on individual receivers. The stacking includes polarity correction based on a simultaneous seismic moment tensor inversion and detection algorithm on the stack function. We applied this method to locate microseismicity induced by hydraulic fracturing. First, we calibrated the velocity model by locating perforation shots at known locations. Then we processed 3 d of data from microseismic monitoring of shale stimulation and benchmarked migration-type locations of the largest events that were manually located. The detected and located events induced by hydraulic fracturing in this case study are mostly shear events forming narrow bands along the maximum horizontal stress direction approximately

100 m above the injection intervals. The proposed technique is fully automated and feasible for real-time seismic monitoring.

3.1 Introduction

Earthquakes (induced and natural) follow the scaling laws discovered by Gutenberg and Richter (1954). As a result, for every large seismic event with a high signal-to-noise ratio (SNR) there is an exponentially growing number of weaker events with a low SNR. One possibility of improving SNR is stacking of many recordings. Detection and location of seismic events by stacking may locate events with a low SNR and provide higher resolution. It is suitable for surface networks of receivers deployed by both academia (e.g., USArray) and industry (e.g., Duncan and Eisner, 2010). These weak events may provide crucial information for seismic hazard as well as new understanding of the earth processes such as hydraulic fracturing.

Passive microseismic monitoring has been used in the mining industry for more than a hundred years (e.g., Mendecki, 1993), in the exploration of water reservoir induced seismicity for at least five decades (Simpson *et al*., 1988) and in the geothermal industry (e.g., Pearson, 1981), but its application in the oil and gas industry is relatively new. The microseismic monitoring for oil and gas focuses on detection and location of seismic events caused by various reservoir activities, such as hydraulic fracturing stimulation, and recently even characterization of the mechanisms of induced microseismic events. This information can be used for assessment of the effectiveness of hydraulic fracture stimulation or identification of active faults and bypassed reserves (e.g., DeMeersman *et al*., 2009). For example, fracture size, stage spacing and well orientation are frequently assessed from microseismic monitoring (e.g., Maxwell *et al*., 2010).

Early location methods require picking of direct arrivals at individual receivers (e.g., Rutledge and Phillips, 2003). This approach requires high SNR of these body-wave arrivals on majority of the receivers. However, P- (or S-) wave arrivals from weak microseismic events (i.e., events with moment magnitudes smaller than -1) are not detectable on individual receivers at the surface (Duncan and Eisner, 2010). Hence, location techniques for surface monitoring of microseismic events usually use stacking or time-reverse modeling for propagation of the emitted seismic energy back to its origin (McMechan, 1982; Gajewski and Tessmer, 2005;

Artman *et al*., 2010). Kiselevitch *et al*., (1991) introduced an alternative technique called seismic emission tomography, where the maximum of semblance over space, time and sensors is used to locate microseismicity. Kao and Shan (2004) developed the Source Scanning Algorithm (SSA) in which the locations are obtained using a brightness function, which is created by stacking of the absolute amplitudes of normalized seismograms recorded at many receivers. The SSA approach was later improved by Kao and Shan (2007), Liao *et al*. (2012), Grigoli *et al*. (2014) and others. Gajewski *et al*. (2007) developed a migration-type approach with the back-projection of recorded seismic waveforms. Gharti *et al*. (2010) proposed to project seismic waveforms into the ray coordinate system, compute their envelopes, and stack along moveouts of P- and S- arrival times. Zhang and Zhang (2013) applied a semblance-weighted stack to extract the coherence of the P- and S-wave in the receiver array. They used a cross-correlation between different components in order to measure the similarity of stacked P and S waves. Finally, Haldorsen *et al*. (2013) suggested a migration-based approach with semblance-weighted deconvolution and applied the method to field data acquired with 3-C receivers in two wells.

The methods mentioned above do not require manual picking of arrivals, however, none of them consider polarity changes due to source mechanisms of microseismic events. Recently several authors have introduced location techniques that does consider polarity changes. Gharti *et al*. (2011) applied time-reverse imaging improved by simultaneous moment-tensor estimation and tested their approach on the synthetic data for a complex model of an ore mine. Rodriguez *et al*. (2012) proposed a method for simultaneous determination of origin time, location and seismic moment tensor of event based on a dictionary-based approach and sparse representation theory. Zhebel and Eisner (2012) introduced a migration-type location technique based on a waveform stacking combined with a source mechanism inversion and tested it for robustness in the presence of noise. Dricker *et al*. (2012) introduced a statistically optimal generalization of the seismic emission tomography method with simultaneous estimation of source mechanism based on grid search through possible source mechanisms. Another migration-type source mechanism imaging technique has been recently introduced by Chambers *et al*. (2013). In their work a norm of moment tensor components is used as a location indicator.

In this study, we develop further the technique introduced by Zhebel and Eisner (2012) to be able to process continuous datasets. We show how a generalized methodology of joint location and source mechanism inversion is able to locate several hundreds of microseismic events. We apply the methodology to a real dataset gathered during hydraulic fracturing of a gas shale reservoir in North America and provide benchmarking of both locations and source mechanisms. The main goal of this study is description and benchmarking of the newly developed methodology on a dataset, rather than presenting a case study.

3.2 Methodology

The methodology involves source imaging based on a diffraction stacking approach (Gajewski *et al.*, 2007; Anikiev *et al.*, 2009; Zhebel and Eisner, 2012; Anikiev *et al.*, 2013) together with moment tensor inversion (Sipkin, 1982). We will refer to the method as the diffraction stacking with the moment tensor inversion (DSMTI). We revise the implementation of this location technique and provide several improvements to event detection. We also generalize the location procedure in order to estimate uncertainty of located events.

At first, the subsurface volume of potential locations is discretized and each grid node is considered to be a potential source position or a so-called image point. The velocity model is derived from the processing of active source data or sonic logs and calibrated with sources at known positions. In this study the location technique uses a P-wave signal (which is usually recorded on vertical components), but it can be formulated for an S-wave signal as well. The velocity model is used for computation of a P-wave traveltime moveouts from each image point to all receivers. Afterwards, waveforms from all traces are stacked along the calculated moveout. As the origin time of a seismic event is unknown, the stacking must be performed for all possible origin times *t*:

$$F_0(r,t) = \left|\sum_{R=1}^{N_R} A_R(t+T_R(r))\right|, \tag{3.1}$$

where **r** is a vector that defines a spatial position (*x*, *y*, *z*) of the image point, (**r**) is the P-wave traveltime from the image point **r** to a receiver *R*, N_R is a number of receivers, A_R is an observed waveform at the receiver *R* and F_0 (**r**, *t*) is the image function.

We use an absolute value of the stack in eq. (1) in order to treat equally positive and negative phases of the stacked amplitudes since we want the positive maximum of the image function to be an indicator of a correct location and origin time of event.

However, microseismic events are usually non-explosive, which means that P-wave (or S-wave) radiation is not isotropic and the polarity depends on the direction of a take-off angle for each pair of the image point and receiver positions. As a result, the polarities of the amplitudes can be both positive and negative. For example, a pure double-couple strike-slip source has the stack value (i.e., the value of the function F_0 of eq. 1) equal to zero at the true source position and true origin time if the receivers are distributed symmetrically above it. It is possible to overcome this problem by using absolute values of the waveforms, what works for data with a high signal-to-noise ratio, but stacking of absolute values does not suppress noise (the noise suppression is the main advantage of migration techniques) as effectively as stacking both positive and negative valued waveforms. To resolve this problem, we propose to account for polarities of a signal while applying the stacking procedure. We invert the polarities of a potential microseismic event by computing the moment tensor at every image point and every potential origin time using the least squares inversion of the amplitudes corresponding to the traveltime moveout (i.e. the waveform amplitudes in eq. 1). Sipkin (1982) showed that the moment tensor can be efficiently computed by:

$$M(r) = \left(\sum_{R=1}^{N_R} G_R^T(r) G_R(r) \right)^{-1} d(r), \tag{3.2}$$

where $\boldsymbol{M(r)}$ is the vectorized moment tensor, $G_R(\boldsymbol{r})$ is the vectorized derivative of Green's function for receiver R and $\boldsymbol{d(r)}$ is

$$d(r) = \sum_{R=1}^{N_R} A_R(t + T_R(r)) G_R(r). \tag{3.3}$$

This inversion is done for each potential origin time *t* and each image point ***r*** as we know neither the location nor the origin time of a microseismic event. The moment tensor is then used to correct polarities of the stacked traces:

$$F(r,t) = \left| \sum_{R=1}^{N_R} \phi_R(r) A_R(t + T_R(r)) \right|, \tag{3.4}$$

where *F(**r**,t)* is an improved 4-D image function and $\Phi_R(\mathbf{r})$ are the weights

$$\Phi_R(r) = sign(M(r)G_R(r)),\ R = 1 \ldots N_R, \tag{3.5}$$

that reverse the sign of the amplitudes A_R when they are negative and allow constructive interference of signals corresponding to the inverted moment tensors. Hence, imaging of a non-explosive source (e.g., double-couple) with the function *F(**r**,t)* has an advantage of enhanced event signatures and improved noise attenuation.

The location and origin time of an event are set to the maximum of *F(**r**,t)*. However, data always contain scattered energy and noise which may result in multiple local maxima of *F(**r**,t)*. Therefore, we need to find out a criterion to identify the maximum corresponding to the first arrival (i.e., the true origin time and location) as well as to define resolution limits of multiple events in time. For this purpose, we developed a new methodology. For every time *t* we evaluate the maximum of the image function over all potential locations (i.e., we assume there is only one event at any given time):

$$F_t(t) = \max_r (F(r,t)). \tag{3.6}$$

The leading local maxima of the function $F_t(t)$ (we will refer to it as the maximum stack function later on) occur at the origin times of microseismic events. These local maxima can be found, for example, by an STA/LTA method [i.e., by measuring the ratio of Short Term Average to Long Term Average energy (Withers *et al*., 1998)]. As the seismic waves scatter at the near-surface or along the path, there can be multiple extrema in the maximum stack function corresponding to later arrivals. Therefore, we need to make sure that only the first (leading) maximum in a group is identified for event detection and location. Obviously, the number of picked events will depend on the SNR of the maximum stack function. The SNR is measured by an STA/LTA ratio. If an STA/LTA detection threshold is too high, too few events will be detected, but we will have a high certainty that the detected events are real. If a too low threshold is used, false events will be detected as real [so-called false positives (Thornton and Eisner, 2011)]. Discrimination of the real event from the false can be improved by additional information beyond SNR. To avoid high SNR values due to local spikes in the recorded waveforms, we validate picked events using semblance (Neidell and Taner, 1971; Kiselevitch *et al.*, 1991):

$$S(r,t) = \frac{\left[\sum_{R=1}^{N_R} \Phi_R(r) A_R(t + T_R(r))\right]^2}{N_R \sum_{R=1}^{N_R} \left[\Phi_R(r) A_R(t + T_R(r))\right]^2}. \tag{3.7}$$

High semblance values (close to 1) indicate that the event is likely to be real because its signal is recorded on majority of receivers and the high stack value does not result from several noisy receivers (common problem in surface monitoring).

After the event has been detected and its origin time t_0 has been determined, the location is obtained using the 3-D image function slice for t_0:

$$F_r(r) = F(r, t_0). \tag{3.8}$$

The maximum of $F_r(\mathbf{r})$ is associated with the location of detected event and the function $F_r(\mathbf{r})$ itself can be used for estimation of uncertainty as an approximation of the maximum likelihood function. However, the accuracy of this approach is limited by the grid step of location zone. To overcome this problem, we transform the image function slice $F_r(\mathbf{r})$ into a probability density distribution (e.g., Tarantola, 2005) as follows:

$$P(r) = C \cdot \exp\left[-\frac{(F_r(r) - \max_r(F_r(r)))^2}{2\sigma^2}\right], \tag{3.9}$$

where σ is a standard deviation of $F_r(\boldsymbol{r})$ and C is a normalizing constant. Event location coordinates are then defined as averages:

$$x_0 = \sum_x \left(x \cdot \sum_{y,z} P(r) \right), \tag{3.10}$$

$$y_0 = \sum_y \left(y \cdot \sum_{x,z} P(r) \right), \tag{3.11}$$

$$z_0 = \sum_z \left(z \cdot \sum_{x,y} P(r) \right). \tag{3.12}$$

An advantage of using the probability density function is that the location coordinates are not restricted to the nodes of a spatial grid. Another useful benefit is a possibility of estimation of the location errors as standard deviations:

$$\sigma_x = \pm \sqrt{\sum_x \left((x - x_0)^2 \cdot \sum_{y,z} P(r) \right)}, \tag{3.13}$$

$$\sigma_y = \pm \sqrt{\sum_y \left((y - y_0)^2 \cdot \sum_{x,z} P(r) \right)}, \tag{3.14}$$

$$\sigma_z = \pm \sqrt{\sum_z \left((z - z_0)^2 \cdot \sum_{x,y} P(r) \right)}. \tag{3.15}$$

Positional uncertainties are driven by an SNR of events. While the vertical uncertainty is more sensitive to noise due to the origin time-depth trade-off, both horizontal and vertical uncertainties decrease rapidly with an increasing SNR (Thornton and Eisner, 2011).

Finally, for each detected event it is possible to find its mechanism, i.e. determine the moment tensor using eqs (3.2) and (3.3) for the known location $\mathbf{r}_0$ and origin time t_0.

3.3 Case study

We applied the DSMTI to a case study of microseismic monitoring performed during the hydraulic fracturing of a Woodford gas shale reservoir in Oklahoma, USA. The case study is devoted to the benchmarking of the suggested technique. The detailed discussion of microseismic locations and source mechanisms as well as geological interpretations are beyond the scope of this paper.

3.3.1 The monitoring geometry

The geometry of microseismic monitoring is shown in Fig. 3.1. Ten lines of a star-like surface array of geophones recording a vertical particle velocity were used to gather passive seismic data. The number of geophones per arm varied between 54 and 122, with 911 geophones in total. The average distance between receivers was 23 m. The rectangular box in Fig. 3.1 shows the zone of interest around lateral parts of wells, where majority of events were expected to be located.

3.3.2 Velocity model calibration

For this case study, we were provided with a 3-D isotropic P-wave velocity model (Fig. 3.1) derived from an active seismic acquisition. The model was adjusted with sonic logs available in this region and provided a good image at the depth of the hydraulic fracture stimulation. The P-wave traveltimes from receivers to subsurface points were computed by a 3-D implementation of a Fast Sweeping Method (FSM) for the eikonal equation (Zhao, 2005).

In order to calibrate the provided velocity model and get more reliable event location results we applied the DSMTI method to data recorded for 4 perforation shots with known locations, corresponding to a single stage of a production well near the center of the array. Fig. 3.2 shows true locations with green circles, whereas locations obtained by the DSMTI are denoted with red crosses sized by the location uncertainty. Lateral deviations of locations from the true positions did not exceed 50~m, but the perforations were located deeper than wells. Hence, we decided to calibrate the velocity model by increasing velocity values in the whole model by 5%. The updated perforation shot locations for the calibrated model are also shown in Fig. 3.2 with blue crosses. Deviations of locations in the model with 105% velocity from the true positions are less than two sigmas indicating that the calibrated velocity model is reliable. The 5% velocity increase is significant considering usual accuracy of active seismic models; however the model is isotropic and the 5% increase may compensate for a possible VTI-type of anisotropy. The slight bias of the located perforations to the east (probably caused by complexity in the near-surface) can be eliminated by application of static time corrections. However, this step was skipped in this study as non-essential. The inverted moment tensors for each of the perforations were dominated by non-shear components of the source mechanisms, with a volumetric percentage close to 40%, a double-couple percentage around 30% and a compensated linear vector dipole percentage of 30%. This is consistent with the expected non-shear character of the perforation shot.

Unfortunately, information about exact origin times of perforations was not available, hence we were not able to estimate the accuracy of the determined origin times.

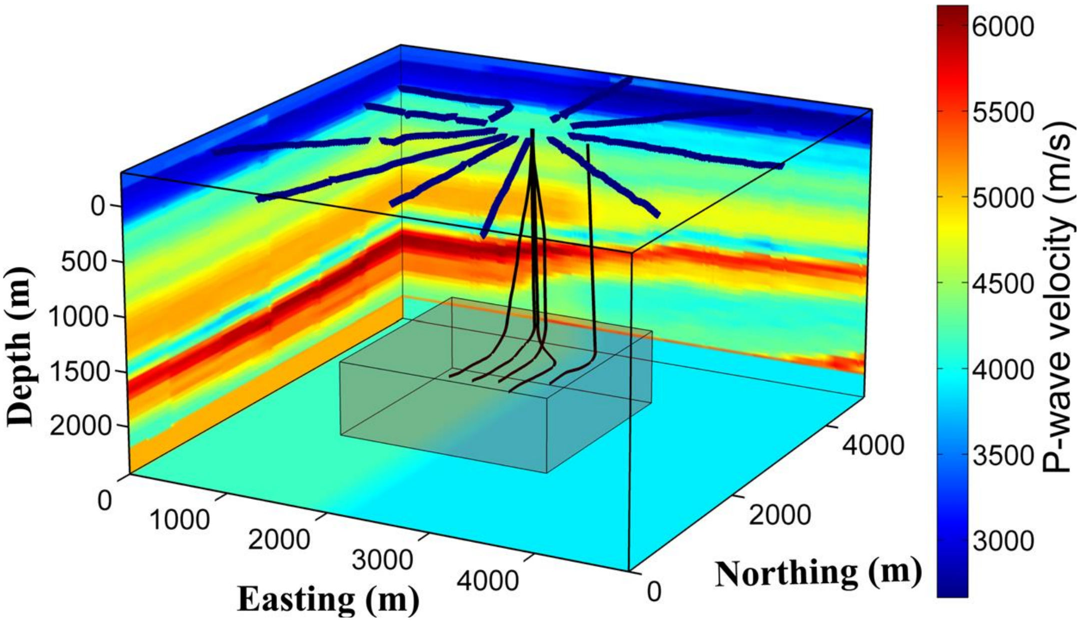

Figure 3.1. The geometry of microseismic monitoring involves the star-like surface array of geophones and production wells in the 3-D isotropic *P*-wave velocity model. The rectangular box shows the zone of interest around lateral parts of wells.

3.3.3 Benchmark analysis of locations and mechanisms for visible microseismic events

For the purpose of evaluating the accuracy of locations obtained by the DSMTI we designed a benchmark test for microseismic events that are visible on individual seismic traces. We selected 34 microseismic events of a highest SNR from the available data. Fig. 3.3 is an example of seismic traces with one of those microseismic events.

For each of the selected events we applied independently two location methods: the DSMTI method and a traveltime maximum likelihood (TML) method (Eisner *et al*., 2010a) based on minimization of a misfit between manually picked first arrivals and traveltimes calculated for a reference velocity model. Comparison of locations obtained with these two methods is given in Fig. 3.4, where red circles represent the TML locations and blue circles are the DSMTI locations. Two positions for each event are connected with a black line. The average lateral location difference is around 30 m and does not seem to show a systematic bias (i.e., appears to be random). As expected, the vertical accuracy is lower: the average vertical location difference is around 75 m [i.e., about 2.5 times greater which is consistent with Eisner *et al*. (2010a)] and the DSMTI locations appear to be shallower.

Detailed analysis of the dataset reveals that signals at greater offsets have peaks at lower frequencies consistent with direct body waves attenuation (Eisner *et al*., 2013). We propose that the signal attenuation results in the observed depth bias of the migration-based locations when compared to TML locations. The lower peak frequency of a signal at greater offsets causes a steeper moveout curve of the peak amplitudes, hence locations based on stacking along peak amplitudes (e.g. DSMTI) have shallower depths (corresponding to steeper moveouts). Note, that the green curve in Fig. 3.3 shows traveltimes computed for event's location and origin time determined with the DSMTI method. These traveltimes fit the largest amplitudes hence resulting in a slightly modified moveout (relative to the first arrivals) as the signal waveforms recorded by receivers with greater offsets have lower peak frequencies. Similar behavior of the diffraction stacking location technique was reported by Anikiev *et al*. (2009) who applied the method to synthetic low-frequency microtremor data and located the modeled seismicity shallower than the actual microtremor emission zone. The TML method based on manually picked first arrivals does not suffer from the same vertical bias since the attenuation does not affect (as severely) the onsets of the arrivals.

The velocity model calibration based on perforation shots does not fully account for the attenuation effect as the perforations and microseismic events have different frequency content (Einšpigel and Eisner, 2012, 2014). This could also explain that some DSMTI-located events in Fig. 3.4 do not have significant vertical bias relative to TML locations, as these events seem to have different frequency content. Further analysis is beyond the scope of this study and subject to further research. Finally, we conclude that the DSMTI locations may have systematic vertical bias up to 100 m (probably related to waveform attenuation and dispersion), but in the horizontal directions they are consistent with the locations derived from manual picks without any observable bias.

Comparison of shear parts of the inverted source mechanisms for both DSMTI and TML methods is shown in Fig. 3.5. Mechanisms were determined from the data amplitudes gathered along trajectories of the traveltime curves corresponding to located source positions (Eisner *et al.*, 2010b). For a double-couple part of the moment tensor decomposition we define the first plane as the plane with steeper dip, and for both methods first plane dip angles are close to 90° (see Fig. 3.5a). Dips of the second plane show greater scatter in the DSMTI results since the dip of the conjugate plane is constrained to a lesser degree as its nodal plane is not observed at the surface monitoring array. Disagreement in certain strike directions in Fig. 3.5b is explained by the fact that some of the determined mechanisms are strike-slip, for which the ordering of planes is not well defined (i.e., both planes are nearly vertical). However, overall the strikes of the steeper dipping plane are in a good agreement with mechanisms inverted from the manually picked amplitudes.

The stability of the source mechanism inversion is illustrated by the studies of Zhebel and Eisner (2012) and Staněk *et al.* (2014). We believe that the source mechanisms obtained by inversion of the manually picked amplitudes (the TML source mechanisms) are more precise than the DSMTI source mechanisms and the remaining differences between these mechanisms in Fig. 3.5 result from uncertainty of the automated migration-based inversion. Hence, we can conclude that the fault plane orientations inverted after the DSMTI are reliable for majority of the microseismic events and agree with the TML source mechanisms within 10 degrees. Determined rake angles are also in a good agreement with the TML mechanisms (see

Fig. 3.5c). Most of the inverted events (25 of 34 tested) were dominated by rakes close to +90° or -90° indicating the dip-slip reverse and normal faulting and the rest 9 events had rakes close to 0° indicating the strike-slip solutions. Furthermore, the non-shear part of the DSMTI source mechanisms reveals more instability compared to the inversion of manual picked amplitudes. Keeping this in mind, we conclude that the double-couple portion of the DSMTI source mechanisms is in a good agreement with the TML source mechanisms. A more detailed analysis of source mechanism types is beyond the scope of this study.

3.3.4 Automatic detection and location of microseismic events within continuous microseismic data.

The DSMTI has been applied to locate microseismicity during a period of three full days in 2008, when several stages of hydraulic stimulation at four production wells were carried out.

For automatic detection of microseismic events we applied the detection algorithm described Section 3.2. An example of a detection result for an interval of 65 seconds is given in Fig. 3.6. In Fig. 3.6 the upper curve is the maximum stack function (i.e. the function $F_t(t)$ defined by eq. 3.6). The STA/LTA algorithm was applied for triggering, so each detected event corresponds to a local maximum of the upper curve provided it is inside the triggered zone on the STA/LTA curve (in the middle of Fig. 3.6) plus it has a sufficiently high semblance (the semblance curve is shown in the bottom of Fig. 3.6). Therefore, in Fig. 3.6 four events were detected, as there were four local maxima (denoted with red dots) that fulfilled the trigger condition of STA/LTA > 2 and the semblance validation criterion $S > 0.1$.

Fig. 3.7 displays the injection data involving a calculated bottom hole pressure (BHP) and a slurry rate (SR) plotted against a histogram of detected events in 20 min bins for a period of 24 hours. Good correlation of injection curves with the number of detected microseismic events shows that majority of events were induced by the hydraulic fracturing, which is a reasonable result that proves reliability of the suggested detection algorithm. Furthermore, all visible events, i.e. the events visible on individual geophones across the array, were detected by this algorithm and had an STA/LTA values greater than 4.

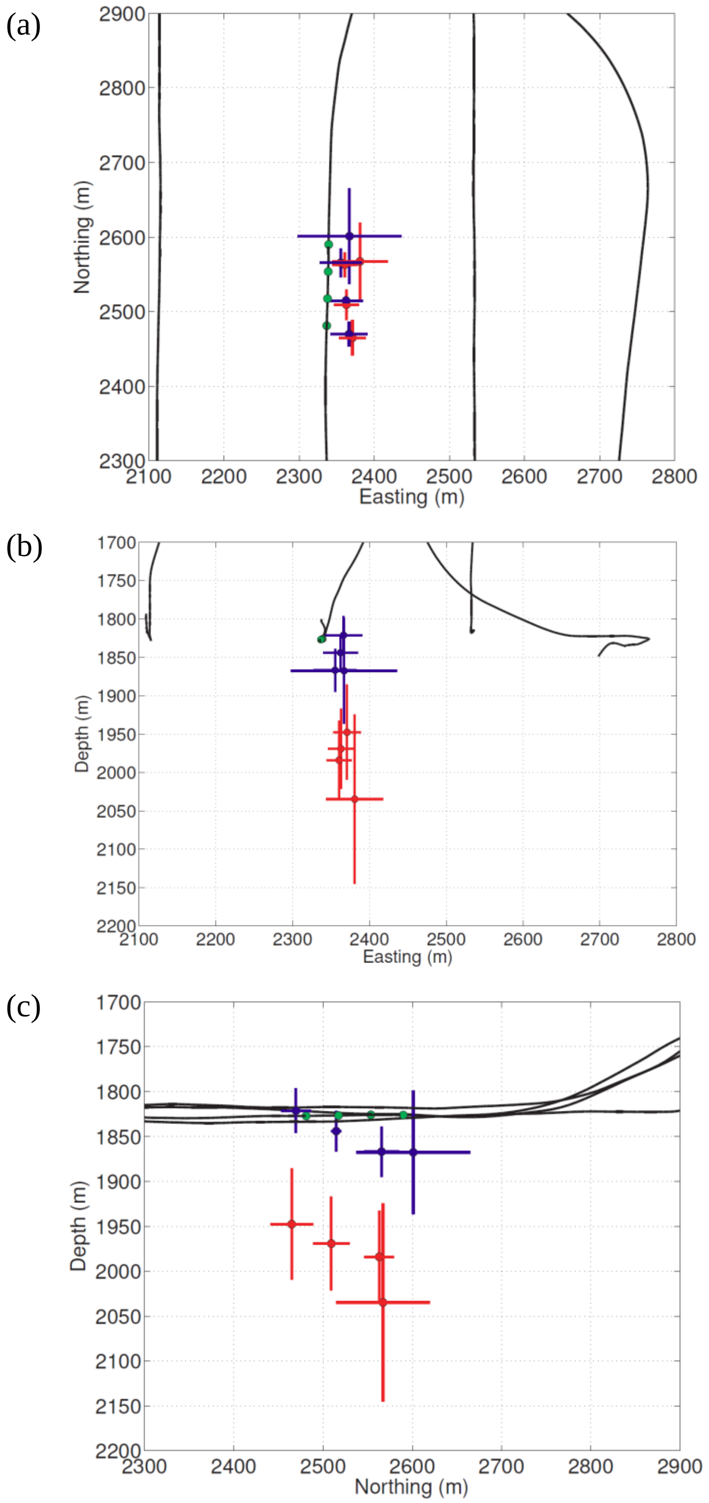

Figure 3.2. Locations of 4 perforation shots obtained by DSMTI: (a) top view; (b) view from the south; (c) view from the east. Actual locations of perforation shots are shown with green circles; shots located using initial uncalibrated model are shown with red crosses sized by uncertainty in the locations. Blue crosses show locations obtained using calibrated velocity model.

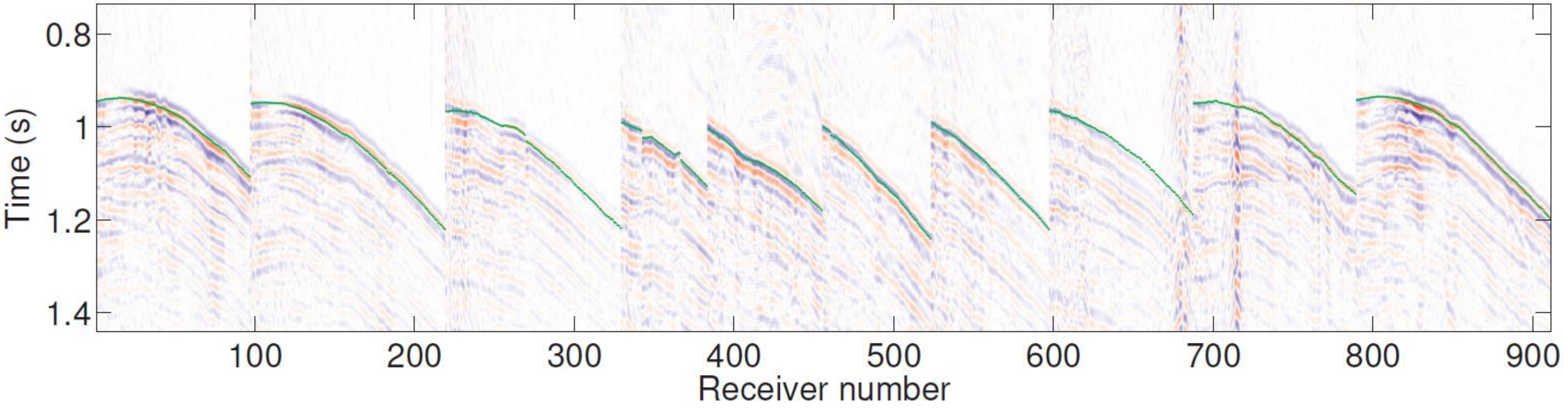

Figure 3.3. Seismic data set containing signal corresponding to one of 34 selected strong events. The green curve shows traveltimes computed for event’s location and origin time determined by DSMTI.

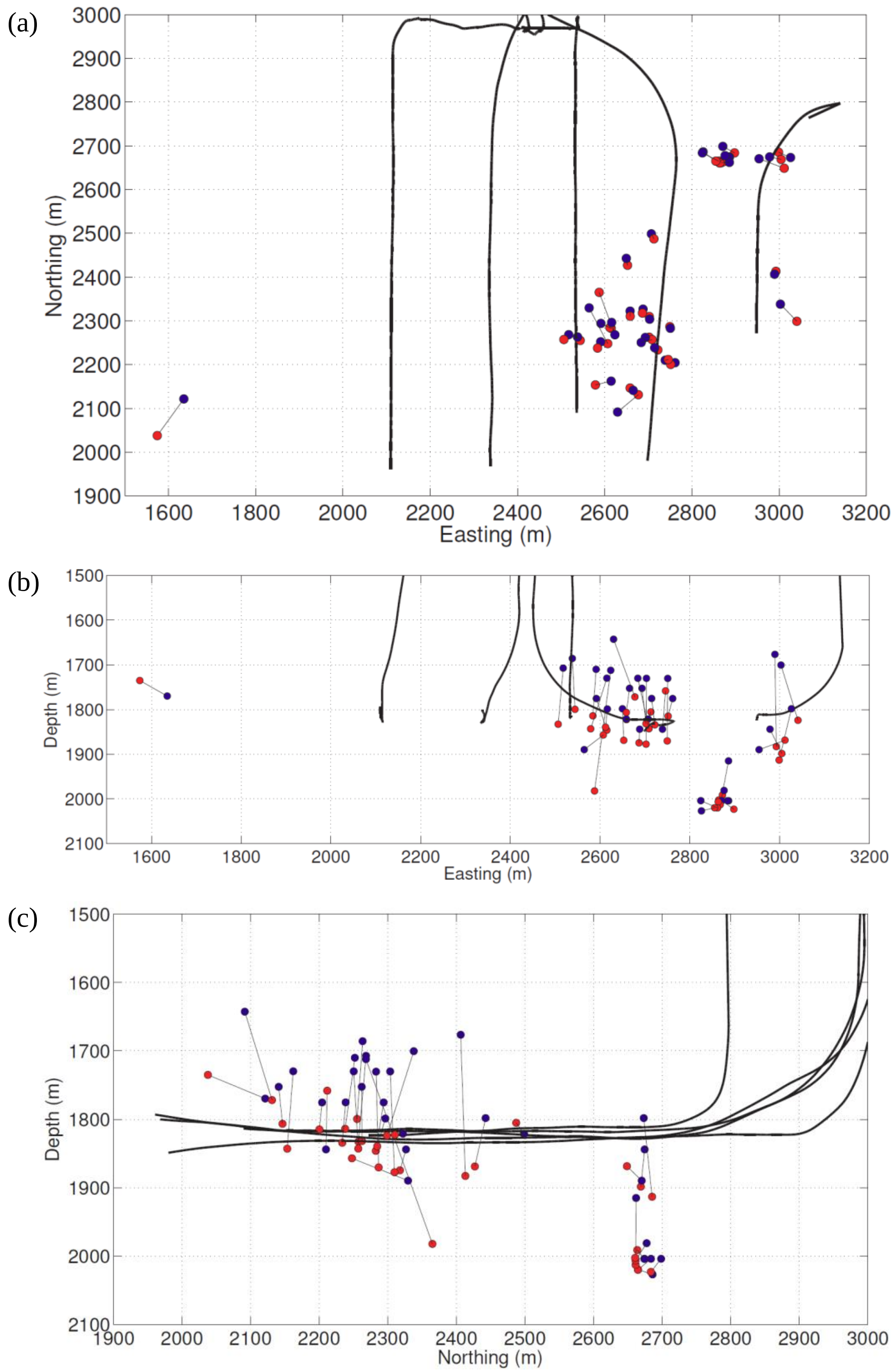

Figure 3.4. Comparison of locations of 34 events determined with two independent methods, TML (red circles) and DSMTI (blue circles): (a) top view; (b) view from the south; (c) view from the east. Circles corresponding to the same events are connected with lines for convenience.

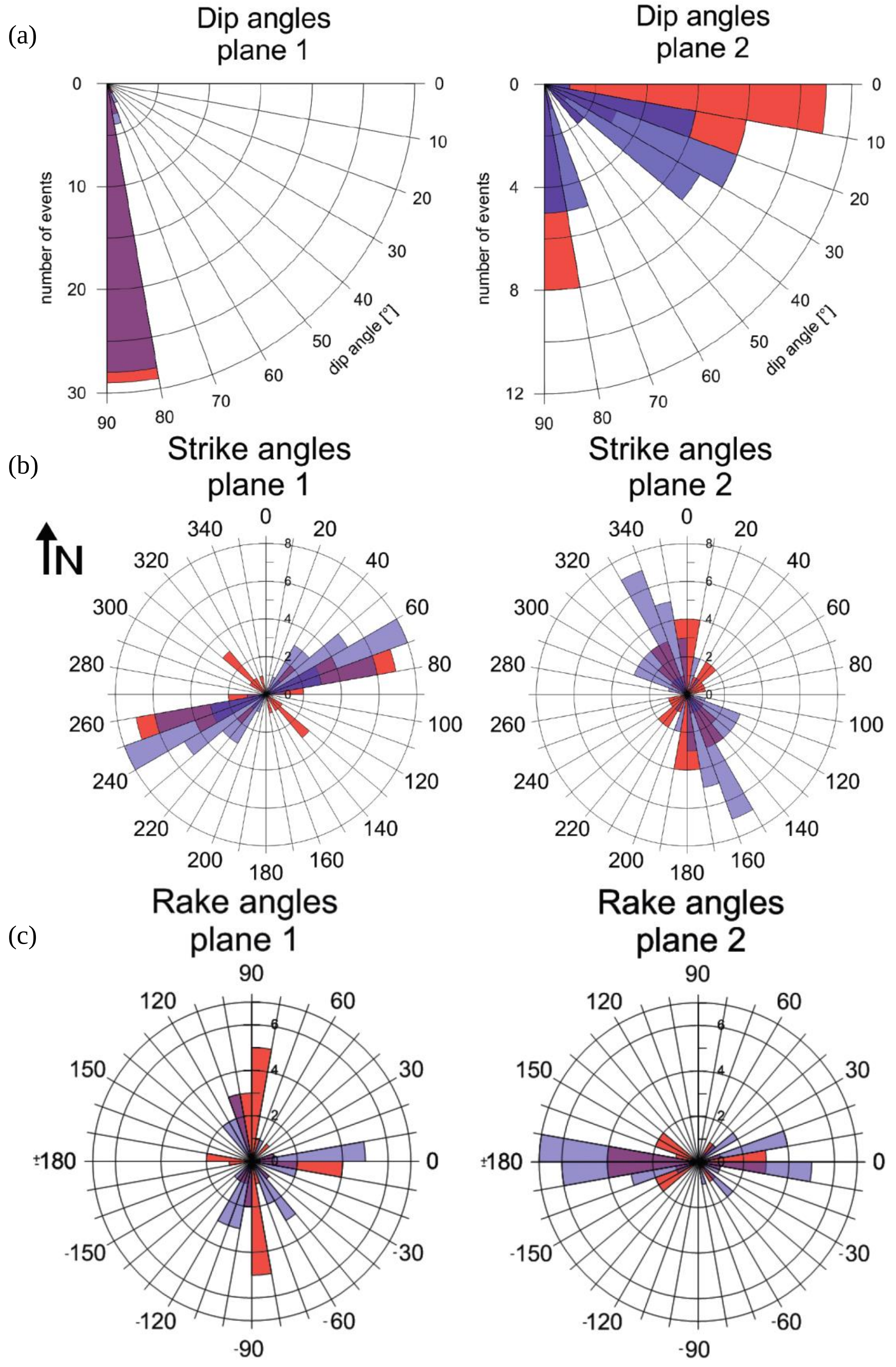

Figure 3.5. Mechanisms of 34 events determined with two independent methods, TML (red) and DSMTI (blue): (a) dip angles; (b) strike angles; (c) rake angles. First plane solutions correspond to steeper dips.

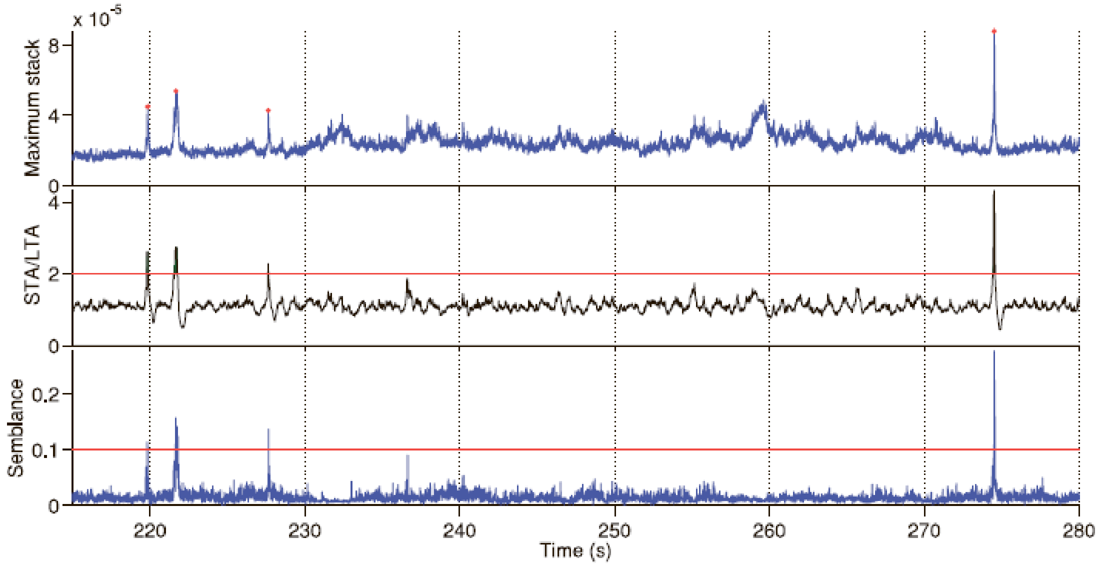

Figure 3.6. An example of detection of four microseismic events within 65 s time interval. Upper curve is the maximum stack function with local maxima denoted with red dots. Corresponding STA/LTA curve with green triggered zones is shown in the middle. Bottom curve displays the semblance of amplitudes involved in construction of the upper curve.

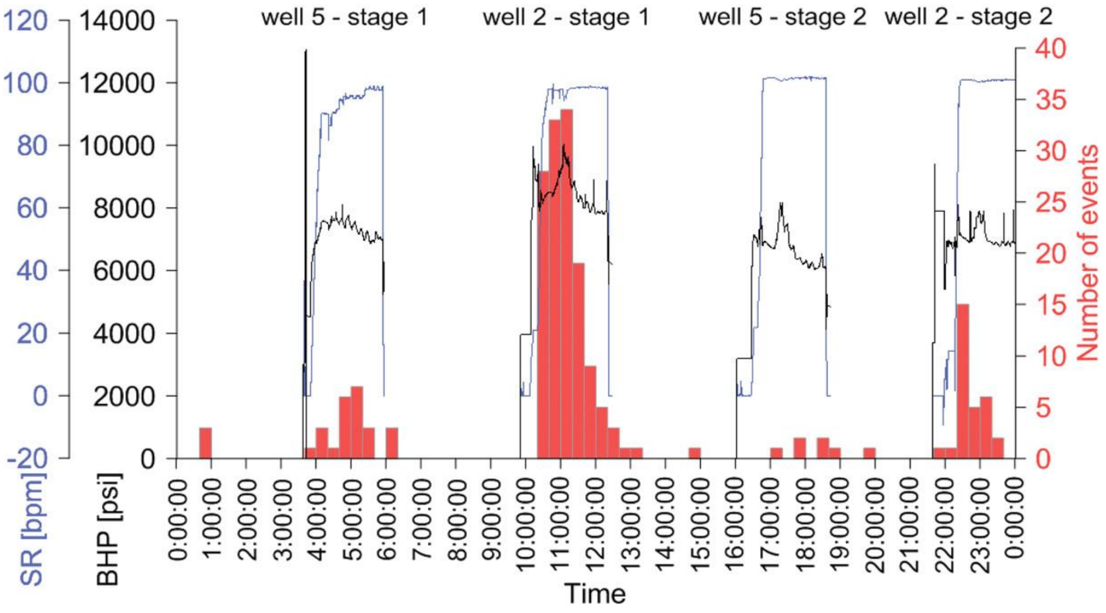

Figure 3.7. Injection data for a period of 24 hr represented by calculated bottom hole pressure (BHP, black) and slurry rate (SR, blue) plotted against the histogram of detected events in 20 min bins (red).

During detection, we considered events with semblances higher than 0.1 as reliable, so for a period of three days we have detected 313 reliable events. A relatively high semblance means that the event is more likely real, but in general it does not mean that its mechanism can be reliably determined. Magnitudes of the detected events varied from -0.3 to -1.7, whereas an average SNR on individual seismograms varied from 1.5 to 0.07 (a cumulative SNR for all stations varied from 45 to 2). Staněk *et al.* (2014) showed on synthetic data that it is possible to reliably invert the source mechanism even from a very noisy signal (i.e. of an individual seismogram SNR up to 0.05). It allows us to conclude that the source mechanisms determined by the DSMTI for majority of detected events are reliable.

Fig. 3.8 shows locations of these microseismic events color-coded by a day when they were detected. Thus, majority of events (223) occurred during day 2 (green), 60 events were detected within day 1 (red) and 30 events within day 3 (blue).

The group of green events corresponds to a period when the southern sections of the second and third well from the west were stimulated. These microseismic events formed trends at approximately 70° NE consistent with a regional direction of the maximum horizontal stress, displayed with gray arrow. We can distinguish several parallel trends suggesting at least three separate parallel fractures developed from this perforation cluster. The events seem to grow from the stimulated interval but they are located approximately a hundred meters above the stimulated wells, although this might result from the bias observed during the benchmark test.

Fig. 3.8(c) shows a group of blue events located deeper than the others. The analysis of mechanisms showed that this group had mainly strike-slip type of mechanism, whereas other groups were described mainly by dip-slip mechanism.

Fig. 3.9 shows polarities and amplitudes as well as beach-ball diagrams for two events representing shear parts of the inverted source mechanisms. Fig. 3.9(a) corresponds to a dip-slip source mechanism type. On the other hand, Fig. 3.9(b) shows a strike-slip source mechanism type, which is common for the group of blue events from day 3 located at a greater depth and shown in Fig. 3.9(c).

The described methodology involves joint detection, location and source mechanism inversion and clearly implies that extensive computations are necessary. However, we were able to optimize computations so that processing of one day of continuous microseismic data took approximately two days on a computer with 32 cores (including traveltime computations in the 3-D velocity model). Roughly estimated, 64 cores will enable almost real-time processing, and what is especially important, this processing is fully automated and does not require any human interaction. This makes our approach feasible for an on-site monitoring during the stimulation.

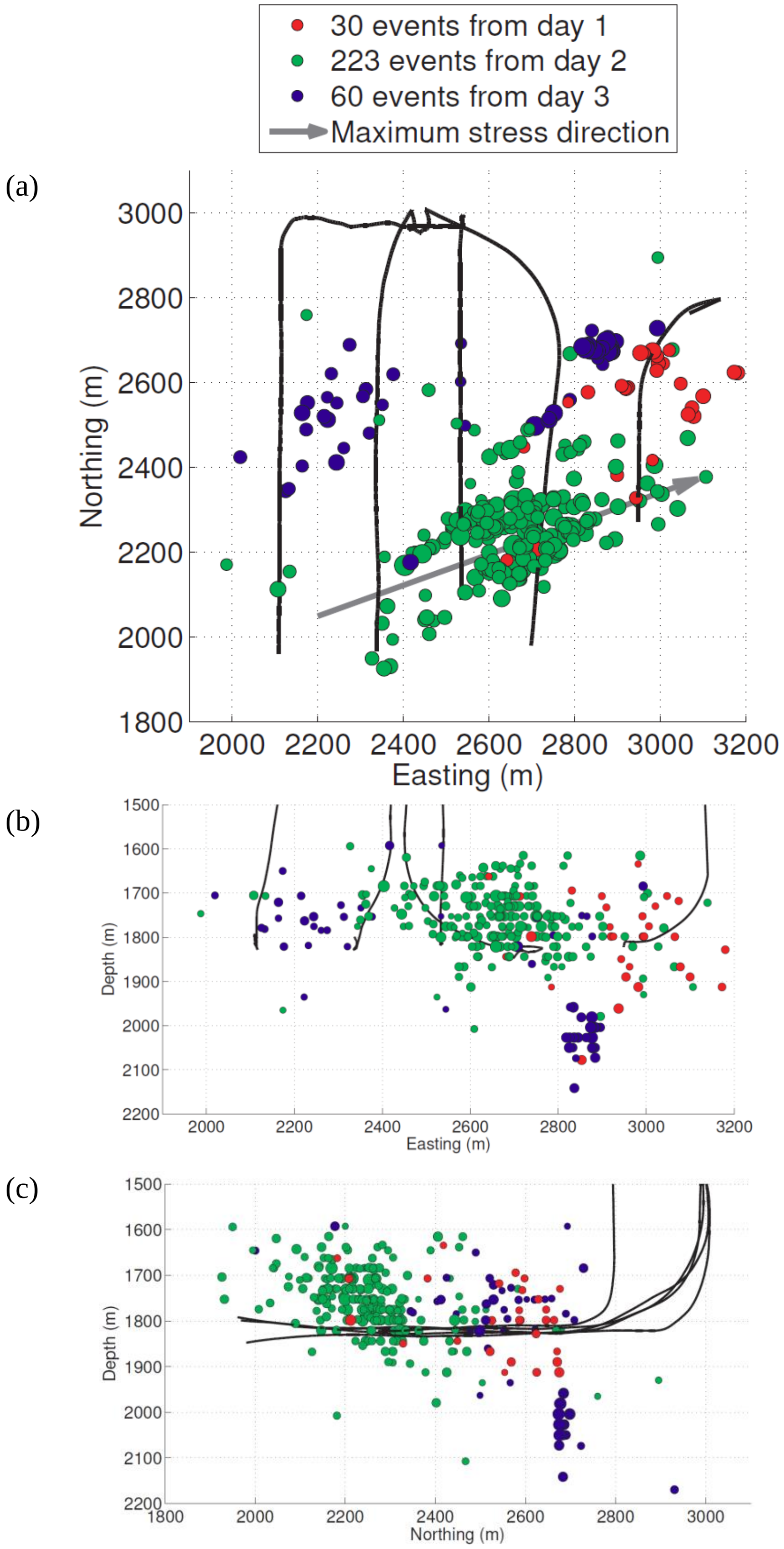

Figure 3.8. Locations of 313 events detected by DSMTI during a period of 3 d: (a) top view; (b) view from the South; (c) view from the East. Event locations are color-coded by a day when events were detected. Grey arrow shows the direction of maximum horizontal stress.

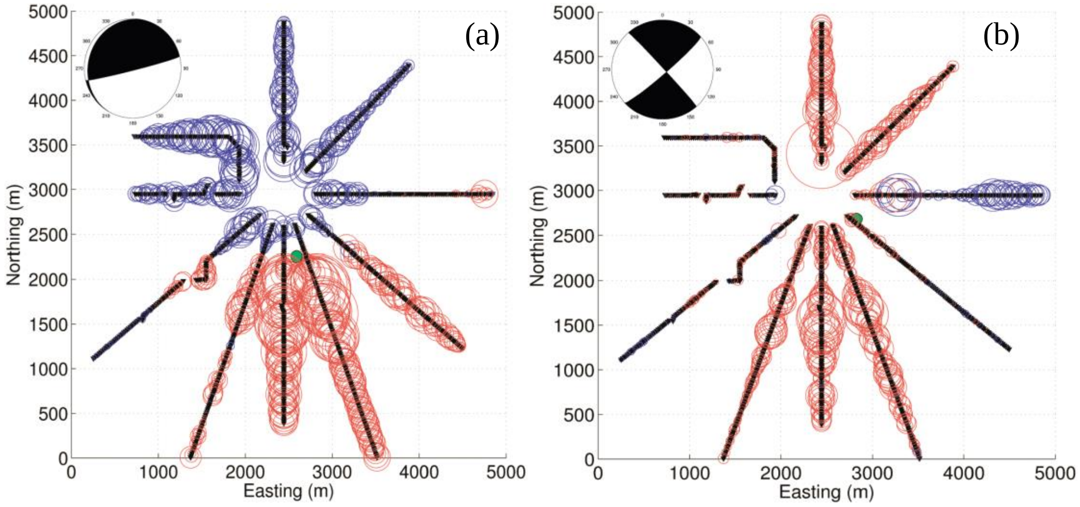

Figure 3.9. Polarity and relative amplitudes corresponding to the moveout of the located event with the highest STA/LTA (≈45.5). Green circle indicates the event's epicenter. Blue circles represent downward motion, red circles represent upward motion, and circle sizes are proportional to the relative sizes of the observed amplitudes.

3.4. Conclusions

A new migration-type automatic location technique has been developed and benchmarked for continuous data processing. The technique involves stacking of seismic amplitudes along traveltime moveouts corresponding to potential origin times together with polarity correction by a seismic moment tensor inversion. We generalized the concept of location to include detection and uncertainty in order to process real seismic data which contain signals from multiple events. For this purpose, we implemented the STA/LTA detection algorithm on a stacked trace and improved location accuracy by evaluating the probability density function for each event.

The locations obtained by the suggested method were consistent with manually located events with an accuracy of 30 m in horizontal positioning and 100m in vertical positioning.

Application to the real continuous dataset showed the realistic microseismic events in a vicinity of the stimulated interval with several trends along the maximum horizontal stress direction. Various types of source mechanisms are automatically detected and reliably inverted by the proposed methodology. The approach is implemented efficiently enough for a real-time on-site monitoring during the stimulation.

Chapter 4

Semblance for microseismic event detection

Published in *Geophysical Journal International*, in 2015,
Volume 201, No. 3, 1362-1369. doi:10.1093/gji/ggv070

František Staněk[1,2], Denis Anikiev[3], Jan Valenta[1] and Leo Eisner[1]

[1] *Czech Academy of Sciences, Institute of Rock Structure and Mechanics, Dept. of Seismotectonics, Prague, Czech Republic*

[2] *Charles University, Faculty of Mathematics and Physics, Dept. of Geophysics, Prague, Czech Republic*

[3] *Saint Petersburg State University, Dept. of Earth Physics, Faculty of Physics, Saint Petersburg, Russian Federation*

Microseismic monitoring from large arrays using migration-based detection and location techniques is limited by detections of false positive events, i.e. the interpretation of spurious/noisy signals as real events. Therefore, semblance has been considered to differentiate between false positive and true events. However, semblance by itself is not suitable for variable signals such as those caused by shear source radiation. We present a new methodology for event detection and location using semblance of amplitudes corrected by a source mechanism. Our method is suitable for multichannel processing of microseismic datasets acquired with large arrays. The amplitudes are corrected by the radiation pattern of the inverted source mechanism before the semblance computation. We show that the source mechanism correction is the key factor in maximizing the value of semblance and makes the detection based on semblance superior to simple stacking. We apply this method to a dataset recorded by a large surface star-like array on synthetic as well as on field data.

4.1 Introduction

Passive seismic methods are now widely used in microseismic monitoring of hydraulic fracturing where large arrays of receivers deployed at the surface, buried in shallow boreholes or installed in monitoring wells are used to map induced seismicity. The goals of microseismic data processing usually include event detection, estimation of hypocenter locations, inversion of source mechanisms and magnitudes characterizing induced events. These results are then used for creation of geomechanical models or simple computation of stimulated rock volume representing a response of the reservoir to stimulation (e.g. Shapiro, 2008; Neuhaus *et al.*, 2013; Staněk and Eisner 2013; Williams-Stroud *et al.*, 2013).

In microseismic monitoring the exact origin time of an event is not known in advance thus we need to acquire data continuously. Hence, we must implement triggering routines to detect events in the data. To do so, we utilize multichannel processing of large datasets where events are represented by the P- or/and S-wave arrivals on each receiver trace. However, these arrivals might have a low signal-to-noise ratio (SNR) which makes event detection on unstacked gathers difficult. While generally the background noise is higher for surface arrays than for arrays in boreholes, both monitoring techniques benefit from overcoming of the low SNR by stacking. The lower amplitude arrivals on both surface and downhole arrays can be usually compensated for by stacking of a large number of receivers covering a wide range of offsets and azimuths, typically for use with migration techniques (Duncan and Eisner, 2010). Such stacking is used to detect microseismic events in passive seismic monitoring, including weak events that are not visible on unstacked gathers.

Migration-based detection techniques usually rely on obtaining a high value of the stack along the moveout curve computed from a hypothetical source position improving the SNR of the unstacked data (Duncan and Eisner, 2010, Chambers *et al.,* 2010, Gharti *et al.,* 2010, Bradford *et al.,* 2013). But typical microearthquakes (or earthquakes in general) do not radiate symmetrically like explosions as the radiated energy and polarity is strongly directional and have specific signatures due to variations in the radiation pattern of various source mechanisms. Recorded amplitudes from a single event have different polarities and amplitudes on different receivers that differ markedly from simple geometrical spreading. Hence, if we simply stacked these positive and negative amplitudes we would get a very low value. This may be overcome by taking absolute values of amplitudes at the cost of reducing the SNR of the stack function. Recently, Zhebel and Eisner (2012), Rodriguez *et al.* (2012), Anikiev *et al.* (2014) or Chambers *et al.* (2014) presented algorithms capable of simultaneously determining the locations and source mechanisms of events. They employ a moment tensor inversion of P-wave (or/and S-wave) amplitudes taken along the moveout for every potential point in 3D subspace and then correct the polarity of amplitudes with the inverted moment tensor before stack. Thus, they obtain the highest stack value at the correct event location and with correctly inverted source mechanism. For detailed discussion of the migration based locations used in this study see Anikiev *et al*. (2014).

A challenge in stacking is that only few or even one high amplitude noisy trace may result in high stack amplitude indicating a spurious detection, the so called “false positive” (Thornton and Eisner, 2011). Such false positives can be avoided by semblance computation which increases for events with similarity of amplitudes on all samples (traces) of the monitoring array included in the stack gather. In comparison to simple stack methods this approach can also detect lower SNR events as it is based on signal coherency and not on the SNR itself. However, we show that the source radiation pattern of dominantly shear events results in relatively low semblance values of direct P-waves. Only when these amplitudes are corrected for the source radiation pattern can we achieve high semblance values. Furthermore, source mechanisms inverted for each potential location can serve as a prediction for the selection of traces with higher SNR and eliminating traces that do not contribute to the stack due to low signal.

Semblance as a useful tool for microseismic events has already been published by Eaton *et al.* (2011) and Chambers *et al.* (2014). It is a relatively new method in microseismic community however in reflection seismic data processing semblance has been used for a long time. We present a new way of using semblance for microseismic detection which is different than in previously published papers.

4.2 Methodology

Under the semblance in this study we understand the simple definition:

$$S(\mathbf{A}) = \frac{\left(\sum_{R=1}^{N} A_R\right)^2}{N \cdot \sum_{R=1}^{N} A_R^2} \quad . \tag{4.1}$$

Here, A_R represents one sample of waveform (amplitude) from R^{th} trace and S is the semblance of all N samples taken from N traces. In this study we follow the methodology of Anikiev *et al.* (2014) and select A_R amplitudes along a moveout corresponding to a potential location of a seismic event, i.e. $A_R = U(R,t(R,O)+t_0)$, where U is the recorded waveform at receiver R, $t(R,O)$ is a traveltime between source O and receiver R and t_0 is origin time. Equation (4.1) is a simplified definition of semblance introduced by Niedell and Taner (1971) who showed that semblance represents ratio of signal energy to total energy for dataset with white noise. Semblance values range from 0 to 1. The minimum semblance value 0 is obtained for the set of amplitudes with zero sum (or zero average of these amplitudes), for example when amplitude set $\mathbf{A}$ consists of random Gaussian noise or a symmetrically (around the nodal lines) sampled radiation pattern of an event with double-couple source mechanism. Semblance S reaches maximum value 1 when the set of samples A_R is uniform, i.e. all A_R are equal. However, this means that the semblance computed from amplitudes corresponding to sources with directionally dependent polarity and amplitude can never reach the maximum value of 1. Hence, we propose a new application of semblance where the samples A_R are neither raw amplitudes nor amplitudes with corrected polarity, but amplitudes fully corrected by source radiation pattern in both polarity and size.

The difference between the semblances computed from uncorrected P-wave amplitudes and from amplitudes corrected by source mechanism is shown in Fig. 4.1. We compare synthetically computed uncorrected amplitudes and amplitudes with corrected polarities based on the source mechanism:

$$A_R = a_R \cdot \mathrm{sign}(b_R) \tag{4.2}$$

and amplitudes corrected in both polarity and size:

$$A_R = a_R \cdot \frac{1}{b_R} \tag{4.3}$$

where A_R is corrected amplitude, a_R is an observed (uncorrected) amplitude and b_R is a synthetic amplitude modeled for an R^{th} receiver due to a moment tensor inverted from all amplitudes a_R. The full moment tensor can be obtained by the linear least-squares inversion of amplitudes (Staněk *et al.* 2014, Anikiev *et al.* 2014).

The semblance of amplitudes without any correction (see example on the left in Fig. 4.1) is close to 0 as these raw amplitudes have an average close to 0 across the array. The semblance for a set of amplitudes with corrected polarity (equation 4.2) is significantly higher and reaches a value 0.657 as the amplitudes are mostly positive. Finally, we show an example of amplitudes corrected in size as well as in polarity (equation 4.3) due to inverted source mechanisms from the original amplitudes. In this case the semblance does not reach exactly the maximum value of 1 only because we did not correct for the effect of geometrical spreading and did not include it in normalizing amplitudes b_R. The numerical test shows that main increase in values of semblance is driven by radiation pattern correction in both polarity and absolute amplitude and amplitude changes due to geometrical spreading account only for a negligible difference of 0.009.

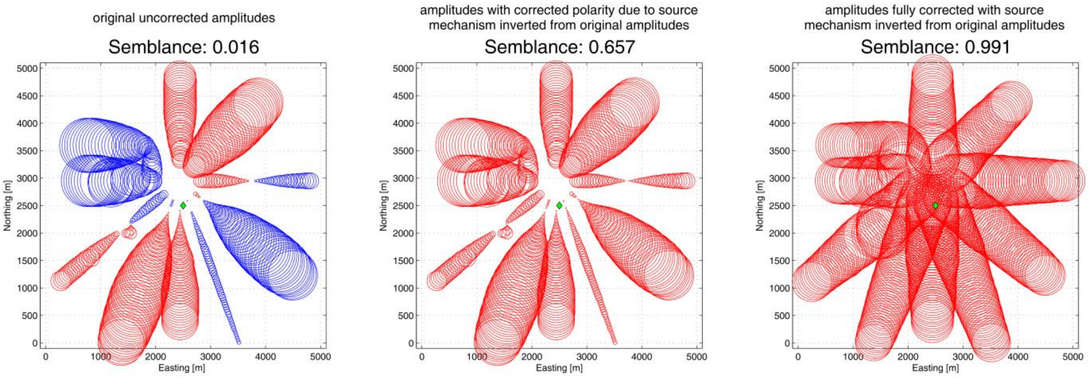

Figure 4.2. Comparison of semblances for noise-free synthetic event amplitudes. Red or blue circles represent negative or positive amplitudes for each receiver. The size of each circle is proportional to the amplitude. The green diamond in the middle shows the event epicenter.

However, in a field dataset (with some level of noise) the receivers in the vicinity of the nodal lines contain no or very little signal and some other receivers may be very noisy due to a local noise such as injection pumps or roads. Such receivers have low SNR and deteriorate the semblance values as the noise is scaled up. This is particularly obvious for receivers on and close to nodal lines where predicted signal amplitude is 0 or very low (using far field approximation). The signal there is dominated by a noise which is further increased by low amplitudes predicted by the radiation pattern (small b_R value compare to a_r value in equation 4.3). Also, the latter case, the seismic noise from pumps, roads etc., could seriously affect results. To avoid this situation, we do receiver selection in two steps. First, we select only the receivers where we expect high signal amplitudes (far from nodal lines) and afterwards to remove noisy traces we select the receivers with small difference between observed and expected amplitudes (i.e. small difference between a_R and b_R in equation 4.3) as it is shown in the workflow diagram in Fig. 4.2. This effectively eliminates receivers where the signal is dominated by noise (example in Fig. 4.3), but still all receivers contributed originally to estimation of the source mechanism.

To find out how the semblance of corrected amplitudes is sensitive to level of noise in data and if it is applicable to detect real events in field data we provided few tests. At first, we tested the method on noise-free synthetic amplitudes. Then we continued using synthetic data contaminated with field noise amplitudes at various SNR and finally we tested field data examples and applied the proposed method to a continuous field dataset. For detection of microseismic events from continuous data we use joint location and inversion of mechanism of Anikiev *et al.* (2013, 2014) and correct both the amplitude polarity and size before the semblance computation (although this step might be also used during post-processing to verify true positive events).

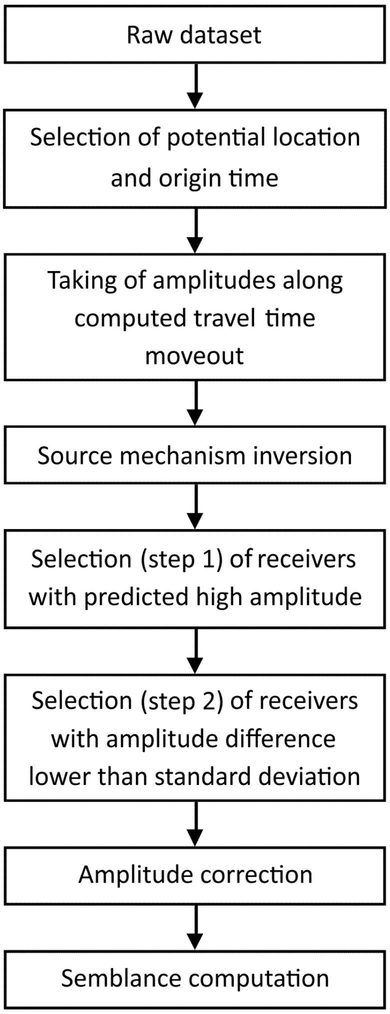

Figure 4.2. Workflow diagram

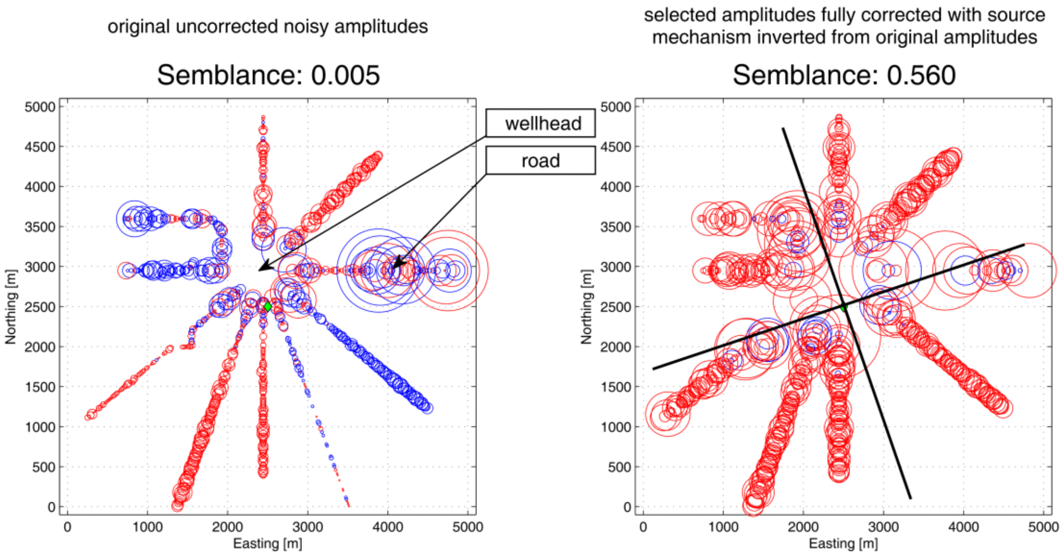

Figure 4.3. Example demonstrating an effect of radiation pattern correction and aplied receiver selections. On the left there are synthetic amplitudes with added noise amplitudes from real data. There is the same color coding as in Fig. 4.1. The Arrows show the artificial sources of noise. On the right, there are amplitudes after their correction and selection. Black lines highlight nodal planes of inverted strike-slip source mechanism.

4.3 Synthetic tests

We created synthetic amplitude gathers for the field array of 911 surface vertical geophones deployed in a star-like pattern with 10 arms. We modeled P-wave amplitudes with a strike-slip source mechanism (strike 70°, dip 90° and rake 0°) of an event located in the middle of array at a depth of 2100 m and the raypaths were modeled through a 1D velocity model derived from a 3D active seismic survey in a real field dataset (see Staněk *et al.* (2014) for more details). The noise-free amplitudes were then contaminated with various levels of real noise taken from the field dataset recorded by an array with exactly the same geometry. The level of noise is defined as a root mean square (RMS) of noise amplitudes divided by the RMS of actual signal amplitudes. Therefore, the range of tested noise levels from 1 to 10 is similar to range of SNR values from 1 to 0.1.

In Fig. 4.1 we show an ideal case using the semblance of corrected amplitudes on an example of noise-free (noise level 0) amplitudes. For noise contaminated synthetic amplitudes we need to consider the elimination of receivers with low signal strength as mentioned earlier. For this particular array, we propose to select receivers for semblance computation in 2 steps. Initially we select 75% of receivers with expected high SNR according to amplitudes modeled for inverted source mechanisms and then we reject receivers with high difference between observed and modeled amplitudes. In the second step, we compute standard deviation of amplitudes differences for remaining receivers and reject all receivers with difference greater than the standard deviation. This eliminates receivers around the wellhead in the middle of the array which are contaminated by noise, some individual noisy receivers and also receivers around the nodal lines for the inverted source mechanism where the noise amplitudes are significantly higher than signal amplitudes (see example in Fig. 4.3). The receiver selection gains importance especially in the case of higher noise as illustrated in Fig. 4.3 where receivers with high amplitudes are removed. If we did not limit ourselves to amplitudes where strong signal is expected, semblance would be computed from amplitude sets including high noise and the semblance values would be lower.

We computed semblances for 50 realizations of each tested noise level to determine the representative values. The results are shown in the box plots in Fig. 4.4. As expected, we observe decreasing median values of semblance with increasing noise level. Median of semblances decreases exponentially from ideal semblance 1 for the noise-free amplitudes to approximately 0.06 for a noise level of 5 and 0.02 for a noise level of 10.

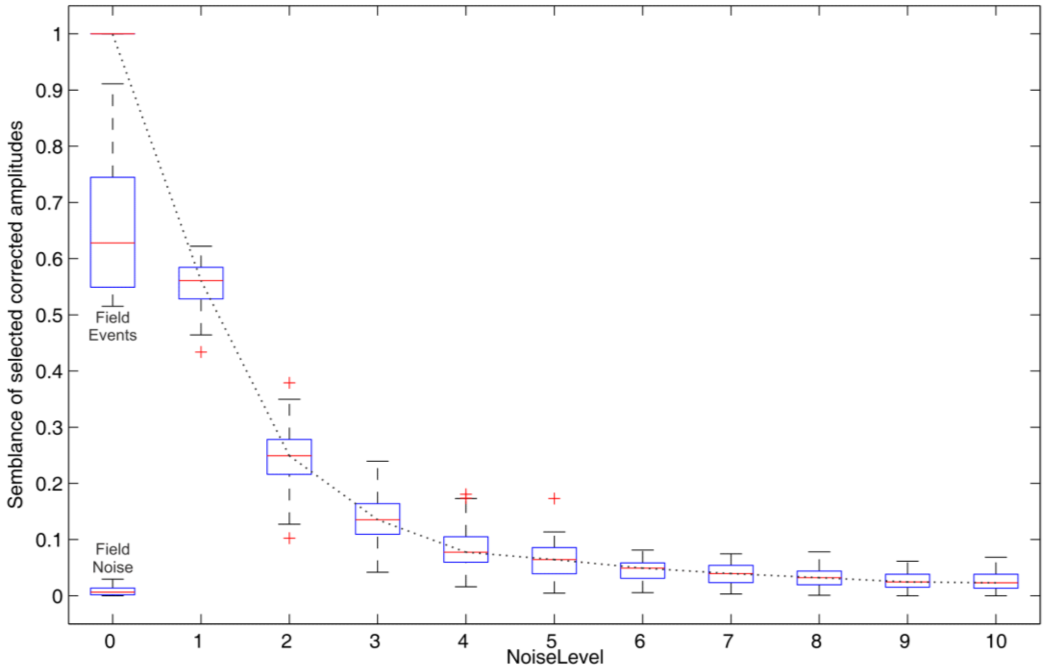

Figure 4.4. Comparison of semblances of corrected synthetic amplitudes with variable noise levels and semblances of field noise amplitudes and field events. Each box plot represents semblances of 50 different amplitude sets. The red lines represent medians, blue edges of boxes define 25 and 75 percentiles, black lines connected with boxes by dashed lines show 5 and 95 percentiles and red plus marks represent outliers.

4.4 Field data examples

We also tested this approach with input field data which was acquired with a surface star-like array during hydraulic fracturing in a shale formation in North America. First, we computed the semblance for randomly chosen amplitudes with field noise to identify a threshold differentiating between noise and an event and then for amplitudes of selected strong microseismic events. The semblance results computed from fully corrected real amplitudes are presented together with the results for synthetic amplitudes in Fig. 4.4. We get a median semblance lower than 0.01 and a maximum value below 0.03 for semblances computed from noise. According to the synthetic tests this means that we are able to detect events with noise as much as 3 times higher than signal for which the minimum semblance is still higher than 0.03. For this level of noise, we should detect no false positive event. For higher noise levels, we may detect false positive events because minimum semblance is in the range of possible semblance values of noise but still the majority of the semblance realizations would result in high semblance.

For our selected field microseismic events with average SNR of approximately 1 and higher (corresponding to noise level 1 and lower), we get the median semblance value 0.62. That is expected value according to previous results from synthetic test for events with similar SNR and proof of reliability of synthetic tests. The minimum semblance is 0.51 and the maximum is 0.91 (see the box plot for field events in Fig. 4.4). Therefore, there is 0.59 (or 59%) semblance value difference between the median of these selected strong events and median of the noise. Furthermore, there is 0.48 or a 48% difference of semblance value between the maximum of noise and minimum semblance values for field events and so we are sure that we can clearly distinguish between noise and strong real event.

4.5 Field dataset

To show that the semblance can be successfully applied in processing a real continuous microseismic dataset we implemented the approach described above within a fully automatic joint detection, location and source mechanism inversion procedure called diffraction stacking with moment tensor inversion (DSMTI) published in Anikiev *et al.* (2014). Semblance is used as a quality control procedure after stacking polarity corrected amplitudes and STA/LTA detection.

The DSMTI involves a search in 3D subspace for the best location and source mechanism which corresponds to the maximum stack of polarity-corrected amplitudes picked along the pre-computed moveout. An example of maximum stack function for a 5-minute file of continuous data is shown in the top panel of Fig. 4.5. The middle panel shows an STA/LTA detection curve which is a commonly used detection approach (Withers *et al.,* 1998). The STA/LTA is applied here to the maximum stack function at each time sample. The lower panel shows the semblance of amplitudes, taken along the moveout curve computed from the image point, that form the maximum stack after their selection and correction by radiation pattern as described in this study.

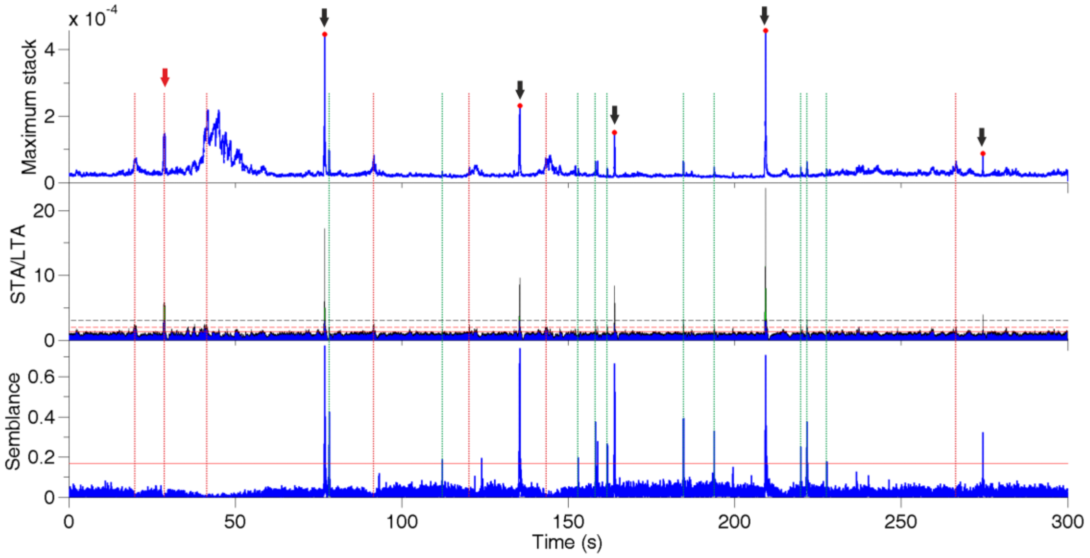

Figure 4.5. Detection results for a 5-minute portion of the field data. The black arrows show clear events detected by STA/LTA applied to the stack function and validated by semblance. The red arrow shows clear false positive. The red vertical lines represent other false positives and the green lines represent additionally found events based on semblance. The horizontal lines show thresholds for STA/LTA 1.3 (red solid line), 2.0 (red dashed line) and 3.0 (black dashed line) and threshold for Semblance 0.17 (red solid line).

With these three functions, we demonstrate how semblance helps us distinguish between false positives and real events and find even weaker events which have not been detected by STA/LTA itself in Fig. 4.5. Real event detections have high stack and high STA/LTA values of this stack function validated by a high semblance. False positives have high stack, and may even have high values of STA/LTA values of the stack above threshold but semblance values are low and do not exceed a threshold. This means that we stack only noisy amplitudes which are not coherent. It is obvious that number of detections depends on setting of threshold values. First, we set STA/LTA threshold to 3 which is adequate to our large surface array (Thornton and Eisner, 2011). With this limit, we get six very high STA/LTA value detections but only five of them are real with semblance above threshold 0.17 (highlighted with black arrows in Fig. 4.5). The threshold 0.17 is a conservative value based on our synthetic tests which should definitely eliminate any noise. Fig. 4.6 shows that with a lower semblance threshold we get events with high location error and we also get random source mechanism orientation inconsistent with orientation of strong events. The remaining detection is consistent with being a false positive event because of low semblance value (highlighted with red arrow). If it was a real event with such a high STA/LTA value, it would have to have a high SNR and a high semblance. We use semblance as a conditional factor after the STA/LTA detection to be able to lower the threshold for detections based on STA/LTA of the stack function. With the lower STA/LTA of the stack function threshold set to 2.0 we get more real events but also more false positives (highlighted with red vertical dashed lines). With even lower STA/LTA of the stack function threshold set to 1.3 we detect many false positive events as would be predicted based on statistics (see Thornton and Eisner, 2011; these false positive detections are not highlighted in Fig. 4.5). However the semblance threshold allows us to eliminate false positive and detect more real events (green vertical lines). These 10 events are weak but real with coherent corrected amplitudes. We also visually inspected the detected weak events and we can observe on some receivers weak coherent signals consistent with microseismic events. The other peaks in semblance are potentially very low SNR events and their selection depends on the threshold choice and tolerance to false positive detections. In our case, lower STA/LTA threshold does not help us to get significantly higher number of validated events.

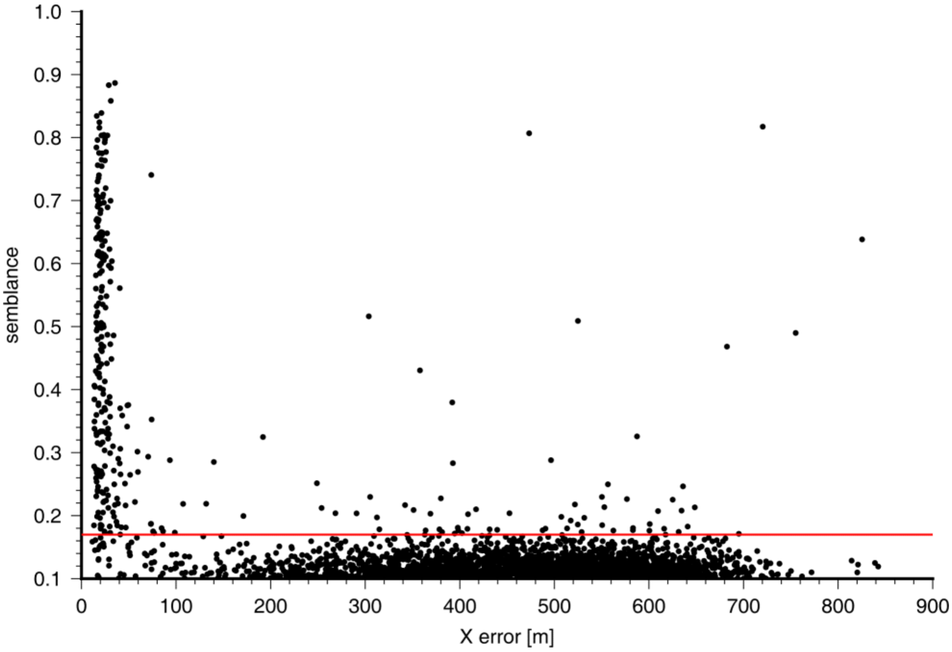

Figure 4.6. Horizontal location error vs. computed semblance of detected events. The black dots represent events and the red line shows conservative lower limit for semblance 0.17.

Using the developed algorithm we processed one day of continuous microseismic data. We show a comparison of results obtained with and without using semblance in Fig. 4.7. On the left side of Fig. 4.7 there is a map view and a histogram of strikes of source mechanisms of events detected only by STA/LTA with threshold 3 without any condition on semblance. On the right side of Fig. 4.7 we show the results with STA/LTA threshold of 1.3 and semblance threshold of 0.17. Map views show that with simple STA/LTA we detected 214 events including 76 false positives (red mechanism plots) with random source mechanism orientations shown in red in the left rose diagram. This result is consistent with the test field data example of Fig. 4.5. With semblance we can effectively eliminate the false positive events and identify an additional 161 events (blue mechanisms) which are weaker. We observe more events in the most active area located along trends in direction with azimuth 70° which is the direction of maximum horizontal stress in the monitored area. Furthermore, the trends are also consistent with orientations of strikes of the inverted source mechanims which would not happen if the events resulted from a random noise. The additional condition semblance helped us to detect 299 real events in one day. Significant false positives seems to be results of noise corelated along linear arms of receivers and harmonic noise on individual traces. That produce relatively high stack amplitude and so naturally high STA/LTA but the semblance is low because amplitudes along the moveout from hypotetical event location are incoherent.

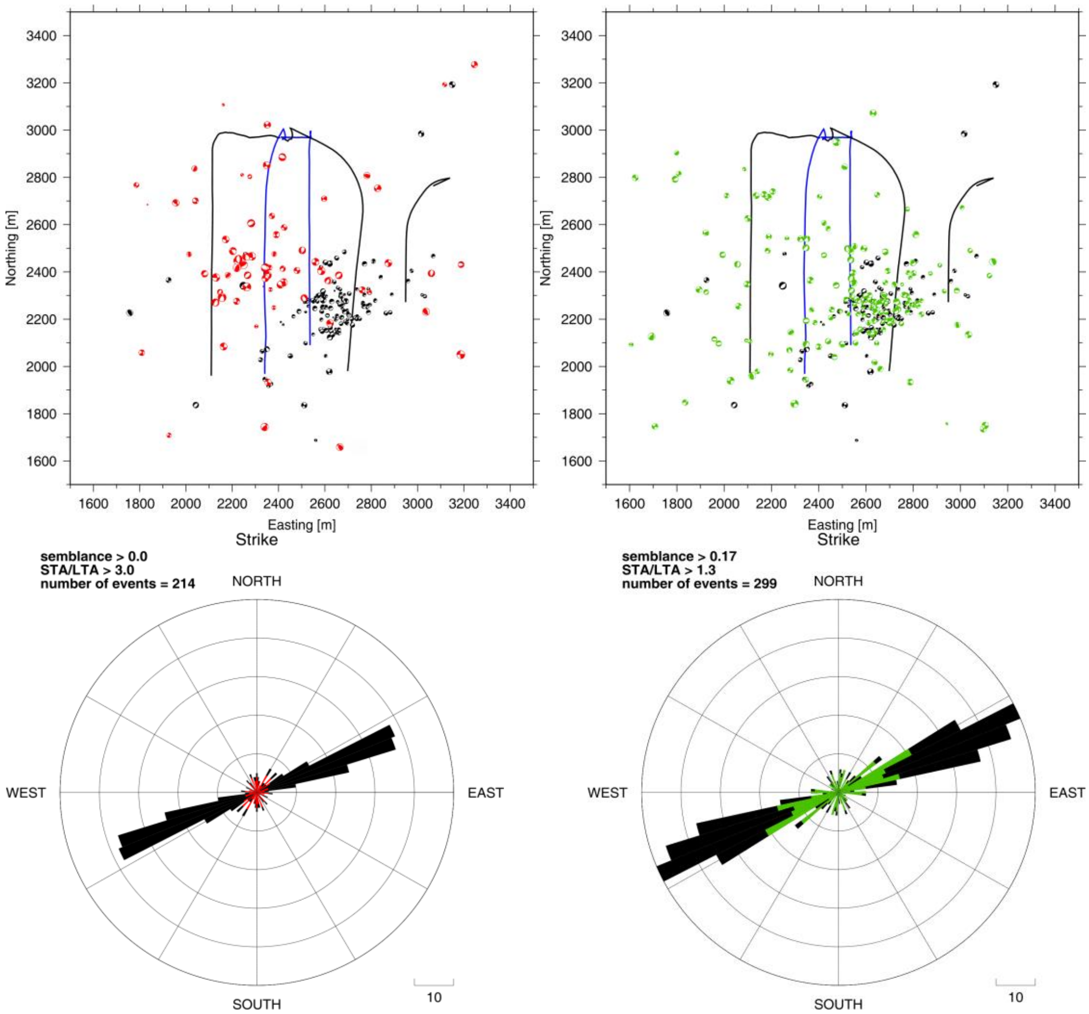

Figure 4.7. Comparison of microseismic events obtained without using semblance on the left and with semblance on the right. The map views show source mechanisms with the event locations. The size of the mechanism is proportional to the magnitude. The black source mechanisms are common for both types of detections: red are false positives and green are additional weaker events. The black and blue lines represent non-stimulated and stimulated horizontal wells. The rose diagrams show strike angles of steeper planes of source mechanisms.

4.6 Discussion

The implemented methodology using semblance as additional criterion for separation of true and false positive events provides a reliable workflow. We have also tested detection and location based on semblance alone without stack, but found that semblance alone was not sufficient and resulted in locations inconsistent with observed data (arrival times on strong visible events were not consistent with the semblance locations). Additionally a very low values of semblance resulted in probably correct detection but poor location of the microseismic events. The condition resulting from the need of excluding receivers close to nodal lines (elimination of receivers with very small b_r values in equation 4.3) or inconsistent b_r and a_r values results in non-linear stacking: the receivers with low SNR or receivers with very high noise are not included in the semblance calculation and therefore we improve semblance by using the most useful receivers. However, to select the right receivers we need to use the correct source mechanism. To do so we use all available receivers as described in Anikiev *et al.* (2014) and we know that the source mechanism is very robust methodlogy for large arrays as shown in Staněk *et al.* (2014). Therefore we may assume the source mechanisms used for semplance computation are correct. The most useful recievers in this sense are those that are consistent with some type of seismic source mechanism and (velocity and density) model. In this paper, we present synthetic tests and results of using P-wave amplitudes only, however the methodology is more general and can be used for S-wave amplitudes (together with P-wave amplitudes or separately) as well.

The selected thresholds are suitable for the particular type of noise and receiver distribution. Threshold selection should be done for each dataset independently as noise condition and receiver configurations differ. However, we have found out that the particular thresholds compensate each other, for example if we select too many receivers close to nodal lines with low SNR we eliminate those receivers as their predicted amplitudes differ from modeled in the second step. In our case, we selected very conservative values, however if a user is willing to tolerate false positive detections a lower threshold may be set.

4.7 Conclusions

We showed how to use semblance for detection and location of microseismic events with complex radiation patterns monitored with large multichannel monitoring arrays. We demonstrate the need for the correction of amplitudes before computation of semblance itself. Only receivers with expected higher signal are selected for semblance computation to avoid contamination from noisy traces. These steps help us to maximize the semblance value for any field dataset with the goal of monitoring of seismic sources. The difference in semblance values for synthetic P-wave amplitudes with various levels of noise and field events is sufficiently high to detect events with SNR as low as 0.3 without any false positive detections for approximately 1000 receivers. With the semblance approach, we are able to eliminate detection of false positives caused by noise and detect more real events which would not be found by simple use of STA/LTA (or would result in a high number of false positives).

Chapter 5

Reservoir stress from microseismic source mechanisms

Published in *The Leading Edge,* in 2015,
Volume 34, No. 8, 890-893. doi:10.1190/tle34080890.1

František Staněk[1,2], Zuzana Jechumtálová[3] and Leo Eisner[2,3]

[1] *Charles University, Faculty of Mathematics and Physics, Dept. of Geophysics, Prague, Czech Republic*
[2] *Czech Academy of Sciences, Institute of Rock Structure and Mechanics, Dept. of Seismotectonics, Prague, Czech Republic*
[3] *Seismik s.r.o., Prague, Czech Republic*

Microseismic monitoring allows an inversion of advanced parameters characterizing a reservoir such as a stress field orientation in addition to usual locations and source mechanisms. We have inverted the source mechanisms of microseismic events induced by hydraulic fracturing in a shale reservoir and using these mechanisms we have obtained the stress field. We have compared stress field inversions using source mechanisms inverted from manually and automatically picked P-wave arrival amplitudes. The stress fields determined from manual and automated P-wave arrival amplitudes are consistent. This implies that we can use the automated inversion of source mechanisms to reliably determine the stress field. The resulting stress fields are stable and consistent with the regional stress field measured in the region (world stress map). We have obtained a maximum regional stress in the vertical direction, which is typical for most of the sedimentary basins, and a maximum horizontal stress oriented approximately 75° from the direction of the drilled lateral sections of wells. Finally, we have also used inverted shape ratio to plot Mohr diagrams illustrating the most likely fault planes activated through the hydraulic fracturing.

5.1 Introduction

Microseismic monitoring is a crucial tool for observing and mapping reservoir response to hydraulic fracture stimulation. Locations of microseismic events determine basic information about the fracture geometry such as a direction of fracture propagation, its length and height. Recently, additional fracture characterization using source mechanisms of induced microseismic events is being provided. Locations and source mechanisms allow building many reservoir models such as discrete fracture network, stimulated rock volume or propped volume. Additionally, the source mechanisms allow also determination of the stress orientation.

Observed source mechanisms of microseismic events induced by hydraulic fracturing in shales are dominated by shearing; non-shear components usually result from noise in data or mismodeling (Staněk and Eisner, 2013). Therefore, we use the shear component of the source mechanism. Each source mechanism of a shear event represents an (micro-) earthquake with two potential fault planes and a slip on these planes. A type of the source mechanism (e.g. strike-slip, normal or reverse) depends on a type of the stress regime in the source area (Anderson, 1942). Every source mechanism causes a specific directional dependent pattern of seismic waves radiated from the event hypocenter. Therefore, we have observed variable amplitudes and amplitude polarities across receiver arrays either at the surface, near surface or in the borehole. We use these directional dependent patterns of seismic waves to determine source mechanisms. Finally, we use the obtained source mechanisms to invert the most suitable orientation of stress field consistent with these source mechanisms.

The idea of estimating the stress field orientation from source mechanisms was developed in early 1980's. The later generalized method by Angelier (2002) uses a set (or a subset) of source mechanisms to obtain the best fitting stress state consistent with a majority of the slippages on fault planes constrained by these source mechanisms.

We apply stress inversion to microseismic events observed during and after the hydraulic fracture stimulation in a shale reservoir. We use results of Staněk and Eisner (2013) and Anikiev *et al.* (2014), i.e., source mechanisms inverted from manually and automatically picked P-wave arrival amplitudes, and compare the stress fields inverted from these two sets of source mechanisms.

5.2 Methodology

We have adopted a methodology of Angelier (2002) and inverted the stress field that fits the best to a set of double couple source mechanisms described by strike, dip and rake angles. However, the complete stress field is described by a stress tensor with six independent components. Unfortunately, the methodology of Angelier (2002) does not allow for determination of all six components, i.e. the exact magnitudes of the principal stress axes and the trace of a stress tensor. We can only determine a simplified stress tensor consisting of the direction (plunge and azimuth) of the three principal stresses (maximum stress σ_1, intermediate stress σ_2 and minimum stress σ_3) and the ratio between the principal stress differences. The ratio $R = \frac{\sigma_2 - \sigma_3}{\sigma_1 - \sigma_3}$, ranging from 0 to 1, has only a relative meaning, while it does not tell anything about the stress magnitudes.

The inversion works with the assumption of a homogeneous stress field being consistent with the selected source mechanisms in the inverted set. However, if the stress field is heterogeneous or subject to temporary changes, we can divide the microseismic events (i.e. their source mechanisms) into the smaller areas and to detect such a stress variation. Creating several subsets of source mechanisms in different locations can be used when stimulating more than one formation or multiple stages and we wish to know if the stress fields are perturbed. But each subset should have a sufficient number of microseismic events with reliably inverted source mechanisms. In theory, only four mechanisms are sufficient to carry out the inversion, but in practice we need more than four source mechanisms due to the uncertainties in a source mechanism inversion and an improved spatial constrain on the stress orientation. The methodology also requires various orientations of faults of seismic events, i.e. we are not able to constrain the stress from repeated slips along exactly the same fault plane. However, it is not clear how different the fault planes should be and how homogeneous the stress field needs to be. Therefore, we have carried out the uncertainty analysis before the interpretation of the results.

In this study, the uncertainty of the inverted stress parameters is estimated with the jack-knife technique. We have computed the orientations of the principal stress axes and the shape ratio from various subsets of the data that have one or several source mechanisms removed. The number of used source mechanisms varies from a complete set of all mechanisms down to a minimum of four. We have repeated the inversion and a random removal of source mechanisms to estimate the stability in determination of the orientation of σ_1, σ_2 and σ_3, and the error in the shape ratio. The scatter of obtained solutions is an estimate of the uncertainty.

Significant advantages of this methodology are short computation time and the fact that we do not need to determine the activated nodal plane of each mechanism. In other types of stress field inversion one of the two possible fault plane solutions has to be determined (each source mechanism has two potential fault planes which explain seismic data equally well).

5.3 Microseismic data application

We have applied the stress field inversion to source mechanisms of events observed during the microseismic monitoring (Staněk and Eisner, 2013; Anikiev *et al.,* 2014). The processed dataset was acquired during four days of hydraulic fracturing in a shale reservoir at the approximate depth of two kilometers. Microseismic monitoring was carried out with a large surface star-like array consisting of almost thousand vertical geophone groups installed around the wellhead in ten lines, each nearly two kilometers long.

The parameters of seismic sources were retrieved using the moment tensor formalism from P-wave amplitudes for selected 75 (out of more than 600 detected events) manually picked microseismic events with a high signal to noise ratio (Staněk and Eisner, 2013) – in this study we call it Group 1. We have also used another set of 299 events with automatically located and inverted source mechanisms from the same dataset – the Group 2. The source mechanisms of Group 2 were obtained by an automatic processing with the Diffraction Stacking Moment Tensor Inversion algorithm (DSMTI). DSMTI is capable to simultaneously detect, locate and invert source mechanisms of microseismic events (Anikiev *et al.*, 2014). Both groups and source mechanisms are shown in maps in Figure 5.1. The Group 1 represents the strongest events from all four days of stimulation, while the Group 2 represents events from only one (the most active) day. Both groups contain mainly dip-slip type of source mechanisms with one nearly vertical and one nearly horizontal nodal plane and a high percentage of shear component. For example, the Group 1 contains 62 dip-slip and 13 strike-slip events shown in the left panel of Figure 5.1.

The uncertainties in the inverted source mechanisms of the Group 1 are very low as the selected events have a high signal-to-noise ratio and we were able to pick P-wave amplitudes and polarities on the wide range of offsets and azimuths (Staněk *et al.*, 2014). The Group 2 includes events with higher noise levels. Amplitudes used for the source mechanism inversion in the Group 2 are automatically picked amplitudes implying a higher uncertainty in the inverted source mechanisms. It is also highly probable that the greater scatter in input amplitudes for the Group 2 have resulted in larger non-shear components of inverted source mechanisms (volumetric and compensated linear-vector dipole) but their orientations of the nodal planes remain very stable and robust (Staněk *et al.*, 2014). Note that only orientations of the nodal planes are used for the stress field inversion. Obviously, the Group 1 source mechanisms are more reliable than the Group 2 source mechanism, but generally, source mechanisms of both groups are consistent (Anikiev et al, 2014).

We have inverted stress field separately from source mechanisms of each group: manually picked events – the Group 1, and automatically processed events by DSMTI – the Group 2. Both obtained principal stress orientations are similar (see Tab. 5.1 or middle panel in Fig. 5.1). The consistency of the stress field inversion results from the consistency of source mechanisms in both of these groups. We have obtained the maximum stress axis σ_1 in a nearly vertical direction with a high plunge (the vertical direction is with a plunge 90°) as it is usually observed in sedimentary basins. The intermediate stress axis σ_2 is very close to the horizontal plane (a plunge close to 0°). The minimum stress σ_3 is also close to the horizontal plane and is perpendicular to σ_2.

The solution for all events in each group shown in the middle panel of Figure 5.1 is highlighted by a yellow triangle. The other stress orientations presented are results of the jack-knife test. As explained, a jack-knife test is used to estimate the uncertainty of the orientation of the stress field. An orientation of the maximum vertical stress axis σ_1 is elongated towards the intermediate stress axis direction. This uncertainty direction results probably from the strike-slip source mechanisms in the Groups 1 and 2 which are caused by a maximum stress in horizontal direction.

Orientations of the maximum horizontal stress σ_2 and the minimum horizontal stress σ_3 are also stable. As these directions are very close to the horizontal plane, the stress directions appear on both sides of the spherical plot in Figure 5.1 with azimuthal difference 180°. Azimuth of the intermediate stress axis σ_2 ranges from

63° to 87°. The minimum horizontal stress σ_3 is the most stable. In general, the relatively small variation in the stress orientations shows a robustness and stability of the stress field inverted from the source mechanisms induced by hydraulic fracturing. It also implies only a small temporal or spatial variability of the stress field. Perhaps, only the elongated uncertainty of the vertical stress may be an indication of the spatial or temporal variation of the stress field.

An interesting observation is that strike-slips and dip-slips are consistent with a single stress field. It means that both types of source mechanisms can be explained by an Andersonian stress regime between normal and strike-slip, a situation fairly common through many regions of the Earth (Zoback and Zoback, 1980).

Another surprising result is the fact that a large number of weak events (with a low signal to noise ratio) found by DSMTI do not cause any significant deviation or scatter in the inverted stress field orientation. It means that we can use automated inversion of source mechanisms to determine the stress field orientation.

Although the principal stress directions are similar for both groups, there is a notable difference in their shape ratios, i.e. ratios between the principal stress differences, shown in Table 5.1. For the Group 1 with manually picked strong events, we get a lower shape ratio than for the Group 2 with automatically proccesed events. This difference is clearly visible in unscaled Mohr diagrams (see the lower panel in Fig. 5.1) that we have constructed using just the shape ratios. The shape ratio of the Group 1 implies a small difference between minimum (σ_3) and maximum horizontal (intermediate regional) stress ($\sigma_{2.}$). The maximum stress axis σ_1, which is in the vertical direction, is much higher. The shape ratio of the Group 2 has the magnitudes of a maximum horizontal stress axis σ_2 and the vertical stress axis σ_1 closer to each other. Note that the shape ratio is the least stable parameter of the inversion. Therefore, we do not try to interpret this difference as it may simply be affected by a noise.

Table 5.1: Inverted stress fields for all source mechanisms in both groups

Group	parameter	azimuth	plunge
Group 1 75 events	σ_1	63.5°	81.8°
	σ_2	245.5°	8.2°
	σ_3	155.4°	0.3°
	R	0.161	
Group 2: 299 events	σ_1	349.7°	75.0°
	σ_2	82.0°	0.6°
	σ_3	172.1°	15.0°
	R	0.664	

The azimuth of the maximum horizontal stress is in direction of the propagation of hydraulic fractures (Anikiev et al, 2014). Newly created (vertical) fractures due to a hydraulic stimulation have propagated in the direction of σ_2 and they have opened against the minimum stress σ_3 which is perpendicular to σ_2. Our stress field orientation also agrees with the direction of regional maximum horizontal stresses found in the world stress map (Zoback and Zoback, 1980). The closest available measurements are from distances of approximately 110 km from our locality but most of the maximum horizontal stresses determined from borehole breakouts are highly similar to our results with a similar range of azimuths from 57° to 95°.

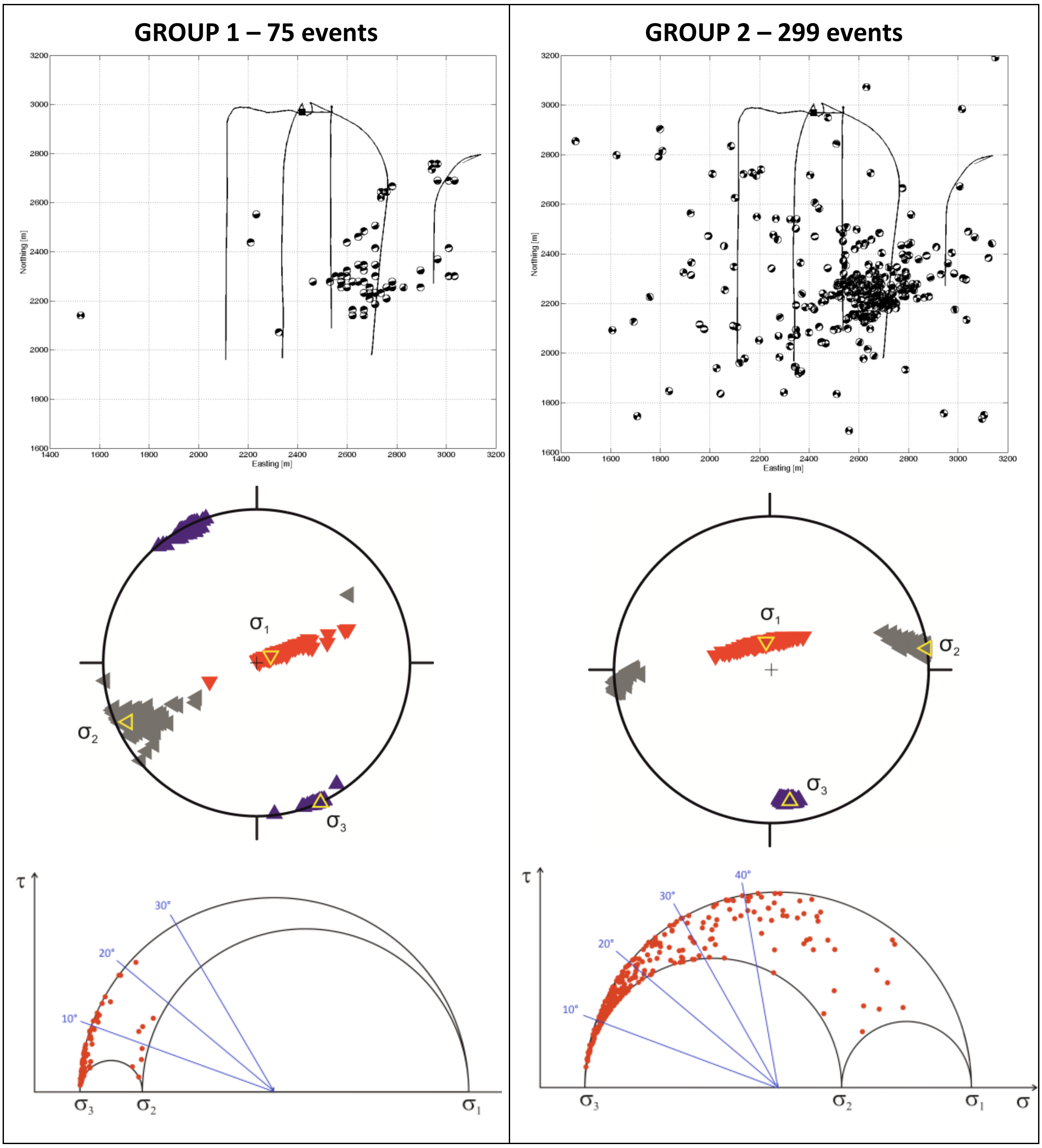

Figure 5.1: Upper panel - Maps with source mechnaisms in event locations. Lines represent stimulated horizontal wells. Middle panel – Principal stress field orientations plotted on a unit sphere. Red, grey and blue triangles show maximum, intermediate and minimum stress orientations inverted for each group of source mechanisms. The best fitting results for all the inverted mechanisms are highlighted by yellow triangles. The jack-knife test of stability of the solutions is displayed. Lower panel - Unscaled Mohr diagrams with normal stress σ on a horizontal axis and shear stress τ on a vertical axis. The orange points represent events. The blue lines show the angles between the stress direction and a fault plane.

5.4 Geomechanical interpretation

Apart from the shape ratio, Mohr diagrams show a normal to shear stress ratio for each event (the orange dots in Mohr diagrams in Fig. 5.1). A coefficient of friction determines a fault plane orientation which is the most predisposed to slip. If we define α as an angle between an arbitrary fault and a maximum stress axis, in the Mohr diagram we have plotted events with an angle 2α from the normal stress axis σ. Considering the usual coefficient of friction 0.6, the most predisposed fault to slip has $\alpha = 30°$.

The angle α is lower than 30° for all the events in the Group 1. We have got most of the events with the angle α even smaller than 10°. However, there are also events having an angle α ranging from 10° to 25°. Such faults are theoretically more predisposed to slip in our stress field and they may be interpreted as a reactivation of pre-existing faults.

The events in the Group 2 have angles α spread from very low (similarly to events in the Group 1) to relatively high (around 40°). A wider range of angles is consistent with more uncertain source mechanisms due to more noise in the data and automated inversion.

Even though we have inverted the stress field, it is difficult to judge which one of the two nodal planes of the prevailing dip-slip source mechanisms is the fault plane. Dip-slip events have one nearly vertical and one nearly horizontal fault plane. In the stress field with a maximum stress axis in the vertical direction the vertical plane may be activated only under the assumption of a very low coefficient of friction due to a low angle between the plane and the stress direction. The horizontal planes should be geomechanically very stable. However, we note that the events occur in a shale formation with naturally weak bedding planes (i.e. potential fault planes with a low coefficient of friction) in a horizontal direction. Therefore, we speculate that the slip might have occurred on the weak horizontal bedding planes with a small dip relative to the maximum vertical stress direction.

5.5 Conclusions/Discussion

We have presented an application of the stress field inversion from the source mechanisms of induced events detected during the microseismic monitoring of hydraulic fracturing in a shale reservoir. We have used two groups of mechanisms, one with mechanisms inverted from manually picked amplitudes and one with mechanisms from automated processing. We have shown that obtained principal stress directions are very similar in both groups. It implies that an automatically processed surface microseismic monitoring dataset may be routinely used to get stable stress field orientation. The maximum principal stress axis is in vertical direction and the maximum horizontal stress axis is oriented with the 75° azimuth consistent with the expected stress field typically observed in the sedimentary basin in the studied region. Neither the presence of the strike-slip mechanisms in the Group 1 nor the automatically processed low signal-to-noise ratio events do significantly increase the uncertainty of the inverted stress orientation. We have observed a relatively small scatter in the inverted stress field orientation consistent with the stress regime between normal and strike-slip. The difference in stresses inverted for two studied groups of mechanisms is in the shape ratio which is the least stable parameter of the inversion and the most sensitive parameter to the noise. Finally, we have observed most of the events with relatively low angles between the fault planes and the stress orientation. This implies a low coefficient of friction for the observed events with dip-slip mechanisms. Such a low coefficient of friction probably results from hydraulic fracturing and/or weak bedding planes. Observed events with strike-slip mechanisms are more favorably oriented to the stress direction and we may interpret them as a reactivation of pre-existing faults or fractures.

Conclusions

Seismicity Induced by Hydraulic Fracturing in Shales: Bedding Plane Slip Model

Published in *Journal of Geophysical Research: Solid Earth*, in 2017,
122, 7912–7926. doi:10.1002/2017JB014213

František Staněk[1,2] and Leo Eisner[2,3]

[1] *Charles University, Faculty of Mathematics and Physics, Dept. of Geophysics, Prague, Czech Republic*
[2] *Czech Academy of Sciences, Institute of Rock Structure and Mechanics, Dept. of Seismotectonics, Prague, Czech Republic*
[3] *Seismik s.r.o., Prague, Czech Republic*

Passive seismic monitoring of microseismic events induced in oil or gas reservoirs is known as microseismic monitoring. Microseismic monitoring is used to understand the process of hydraulic fracturing, which is a reservoir stimulation technique. We use a new geomechanical model with bedding plane slippage induced by hydraulic fractures within shale reservoirs to explain seismicity observed in a typical case study of hydraulic fracturing of a shale gas play in North America. Microseismic events propagating from the injection point are located at similar depths (within the uncertainty of their locations), and their source mechanisms are dominated by shear failure with both dip-slip and strike-slip senses of motion. The prevailing dip-slip mechanisms have one nearly vertical nodal plane perpendicular to the minimum horizontal stress axis, while the other nodal plane is nearly horizontal. Such dip-slip mechanisms can be explained by slippage along bedding planes activated by the aseismic opening of vertical hydraulic fractures. The model explains the observed prevailing orientation of the shear planes of the microseismic events, as well as the large difference between seismic and hydraulic energy.

C.1 Introduction

Hydraulic fracturing is a process in which a liquid is pumped through a well down into a formation under a pressure high enough to cause cracks in the rock formation. The injection pressure must exceed the minimum principal stress at the injection point to achieve an opening mode within the fractured formation (Hubbert & Willis, 1957). Such a stimulation process creates hydraulic fractures that propagate perpendicular to the minimum principal stress against the direction of the maximum principal stress. Within oil and gas reservoirs (unlike for geothermal reservoirs), the hydraulic fractures are bounded by layers of sedimentary rock, subsequently resulting in horizontal propagation against the maximum horizontal stress. This technique is routinely used to increase the permeability of both conventional and unconventional oil and gas reservoirs (e.g., Economides & Nolte, 2003) or to create flow paths in geothermal systems (e.g., Pearson, 1981). Furthermore, in most oil and gas reservoirs, solid particles known as proppant, which are suspended in the injected fluid, are pumped into the opened fractures to keep the fractures from closing. These particles are incompressible (e.g., sand and ceramics) and therefore limit the minimum size of the open fractures and the volume inside the fractures.

Reservoir stimulation, such as hydraulic fracturing, is accompanied by induced seismicity resulting from the reactivation of preexisting fractures or the creation of new fractures. Typical microseismic events connected with the creation of new fractures possess moment magnitudes lower than 0; hence, they are too small to be felt at the surface (Maxwell, 2014). When hydraulic fractures activate preexisting natural faults, this activation may result in seismicity that can be felt (e.g., Clarke *et al.*, 2014). We can monitor induced seismic activity using either (near-)surface geophone arrays (Duncan & Eisner, 2010) or borehole geophone arrays (Maxwell *et al.*, 2010). Such monitoring is used to map the fractures. Locations of microseismic events are then used to map the fracture geometry: the direction of fracture propagation, fracture length, and height.

The observed seismicity contains additional information—the source mechanisms. The injection of the fluid and creation of fractures that can store large volumes of incompressible proppant particles suggests that seismicity induced by hydraulic fracturing may have a volumetric component. However, observed microseismic source mechanisms are dominated by shear double-couple sources (e.g., Pearson, 1981; Rutledge & Phillips, 2003). Furthermore, the identified fault planes of these shear sources are consistent with the natural fracture orientations observed in these sedimentary rocks (Williams-Stroud *et al.*, 2010). However, there are doubts as to whether the nonshear components of microseismic events induced by hydraulic fracturing are real. For example, Baig and Urbancic (2010) reported observing mostly tensile closing and opening mechanisms. The difficulty in determining the nonshear component of the source mechanisms is a consequence of the limited resolution of downhole microseismic monitoring arrays (Vavryčuk, 2007) and the low signal-to-noise ratio (SNR) of surface monitoring data sets (e.g., Chambers *et al.*, 2010). Staněk *et al.* (2014) addressed this issue by testing the limits of a surface monitoring synthetic data set on the SNR of microseismic events with typically observed source mechanisms induced by hydraulic fracturing.

Another important parameter used to characterize the microseismic events is size, which is usually measured by a magnitude (or the seismic moment) that represents the total energy released by a microseismic event (Cieplicki *et al.*, 2014). The source mechanisms allow us to interpret the determined seismic moments; that is, shear event moments (moment magnitudes) are proportional to the sizes of fractured planes (assuming a constant stress drop), while volumetric event moments (moment magnitudes) represent the amount of volumetric change (e.g., Eaton & Mahani, 2015). Thus, a complete source mechanism characterization is crucial for the correct interpretation of the interaction between microseismicity and hydraulic fracturing.

Early interpretations of microseismic activity induced by hydraulic fracture treatments (Aki *et al.*, 1982; Pearson, 1981) concluded that microseismic events result from shear failure induced by fluid percolation along preexisting fractures due to diffusion. These conclusions were mostly deduced from observations limited to a few offsets and azimuths from one or two monitored boreholes. A major limitation of borehole-based source mechanism inversions was identified by Nolen-Hoeksema and Ruff (2001) or by Eaton and Forouhideh (2011), who noted that data from a single (vertical) array of receivers in a 1-D velocity model do not constrain inversion of the volumetric component of a source mechanism. Vavryčuk (2007) showed theoretically that a single-azimuth data set (as in a single vertical monitoring well) cannot resolve the dipole perpendicular to the plane of stations and the hypocenter. Thus, single-azimuth data cannot resolve tensile opening associated with volumetric changes of microseismic events. Current studies of source mechanisms of microseismic events induced by hydraulic fracturing monitored using boreholes seem to observe both shear and nonshear mechanisms. Some studies concluded that all induced events are pure shear, for example, Phillips *et al.* (1998), Rutledge and Phillips (2003), and Rutledge *et al.* (2015), while other studies concluded that induced events are associated with both shear and volumetric changes, for example, Jechumtálová and Eisner (2008), Nolen-Hoeksema and Ruff (2001), and Šílený *et al.* (2009). For example, according to results of Baig and Urbancic (2010), the source mechanisms of microseismic events vary substantially in the orientation and the percentage of the volumetric component. These authors explained microseismicity as a combination of fracture opening, closing and shearing on various fault planes due to local changes in stress orientation caused by hydraulic fracturing. Similarly, Julian *et al.* (2007) observed some tensile opening events during hydraulic fracture stimulation, some tensile closing events after hydraulic fracture stimulation, and some shear events before, during, and after stimulation.

Later, Eisner *et al.* (2010) took advantage of large surface arrays monitoring hydraulic fracture stimulation within a sedimentary basin and inverted the source mechanisms of several microseismic events characterizing the observed induced seismicity. These authors found that the observed microseismic events can be explained by pure shear dip-slip failure. Furthermore, the dip-slip mechanisms with one steep (nearly vertical) plane show shear failure along a vertical (or horizontal) plane in both the normal and reverse sense. Reverse mechanisms along less steeply dipping planes do not show similar reversals. As the normal and reverse motion along the same fault plane cannot possibly be explained by simple tectonic loading, the normal and reverse mechanisms of events characterized by dip slips must be induced by hydraulic fracture, while reverse faulting along less steeply dipping planes can be caused by the reactivation of a preexisting fault. This finding implies that the characterization of source mechanisms allows the differentiation of microseismic events induced by hydraulic fracturing from events induced along preexisting natural faults.

In this study, we analyze the shear and nonshear components of the source mechanisms in a typical case study using a large surface microseismic monitoring array. We invert stable source mechanisms from P-wave amplitudes and carefully test the reliability of nonshear components. Based on the observed data, we show that the geomechanical model of bedding plane slip proposed by Staněk and Eisner (2013) and Rutledge *et al.* (2013) explains the observed source mechanisms during the hydraulic stimulation of shale reservoirs.

C.2 Case study – typical microseismicity induced by hydraulic fracturing

In this study, we analyze a microseismic data set acquired continuously for 4 days during the hydraulic fracture stimulation of a shale gas reservoir in the Arkoma Basin in the United States. The Arkoma Basin is one of the most prominent gas production areas within the territory of the United States and represents an E-W elongated sedimentary basin stretching through Oklahoma and Arkansas. Among the members of the Arkoma sedimentary sequences, the Woodford formation (called also the Chattanooga formation in Arkansas) clearly produces the most gas and oil (Spötl *et al.*, 1998). The thickness of the Woodford varies between 15 and 67 m in the Arkoma Basin (Agrawal, 2009), while according to Cardott (2013), it can exceed 90 m in the Anadarko Basin. The thickness is generally the smallest in the center of the basin and increases toward the edges, while the SW part is thicker. The depths of the formation range between 2,000 and 4,000m (Guo *et al.*, 2010).

Outcrops of the Woodford exhibit black to gray brittle shales with three distinct natural fracture sets. Within the production area at depth, two main fracture systems are found—the primary E-W system and the secondary ENE-WSW system (Waters *et al.*, 2009). The secondary fracture system indicates the ENE-WSW direction of the maximum horizontal stress (σH). The induced fractures revealed by image logs and microseismic imaging of hydraulic fractures also show this orientation (Waters *et al.*, 2009).

The Woodford shales are generally considered slightly overpressured reservoirs (e.g., Agrawal, 2009) with a pressure gradient between 0.0108 MPa/m and 0.0124 MPa/m. However, Neuhaus and Miskimins (2012) observed a lower gradient—between 0.0079 MPa/m and 0.0101 MPa/m—leading to a slightly underpressured reservoir. Nevertheless, these low numbers could be due to local variations in physical properties. These authors (Neuhaus & Miskimins, 2012) also reported other physical properties at a depth of 2,397 m (perforation depth), including a total stress of 42 MPa and a fissure opening pressure of 4.48 MPa.

Our case study addresses four horizontal wells that were drilled into the Woodford shale formation at true vertical depths of approximately 2,100 m. All the wells start at the surface from one pad (i.e., a site where multiple wellheads are located), and each well is stimulated in three stages (Figure C.1). The first stimulated well, well 4, is stimulated from tip to toe, followed similarly by well 3, and finally, a zipper-frac method is used for wells 5 and 2 (i.e., the first stage is stimulated in well 2, followed by a first stage in well 5, followed by the next stage in well 2, and so on). Lateral parts of the wells are drilled nearly perpendicular to the maximum regional horizontal stress. The vertical (overburden) stress at the depths of the source formation is also the maximum principal in situ stress, as it is common throughout most of the sedimentary basins; however, the vertical and maximum horizontal stress may be close to each other in terms of magnitude. The verticality of the maximum stress was also confirmed by the stress inversion of Staněk, Jechumtálová, *et al.* (2015) using the shear components of the observed microseismic events.

Microseismic monitoring was performed with a large star-like array with a total of 911 single-component vertical geophones deployed at the surface. The receivers were spread out along 10 radial lines centered around the wellhead. The minimum number of receivers per line was 54, demonstrated by line number 4, and the maximum number was 122 for the longest lines, lines 2 and 10. With an average distance between receivers of 23 m, the array covered approximately 25 km2. Such a configuration guaranteed a wide coverage of azimuths and offsets with a receiver offset-to-depth ratio of approximately 1, which is ideal for any surface monitoring array. Noise present within this type of acquisition is successfully eliminated by stacking the signal over all the receivers (Anikiev *et al.*, 2014; Duncan & Eisner, 2010). Using a large number of receivers and a sampling frequency of 2 ms for the radiated energy allows us to perform a very robust inversion for the source mechanisms (Staněk *et al.*, 2014).

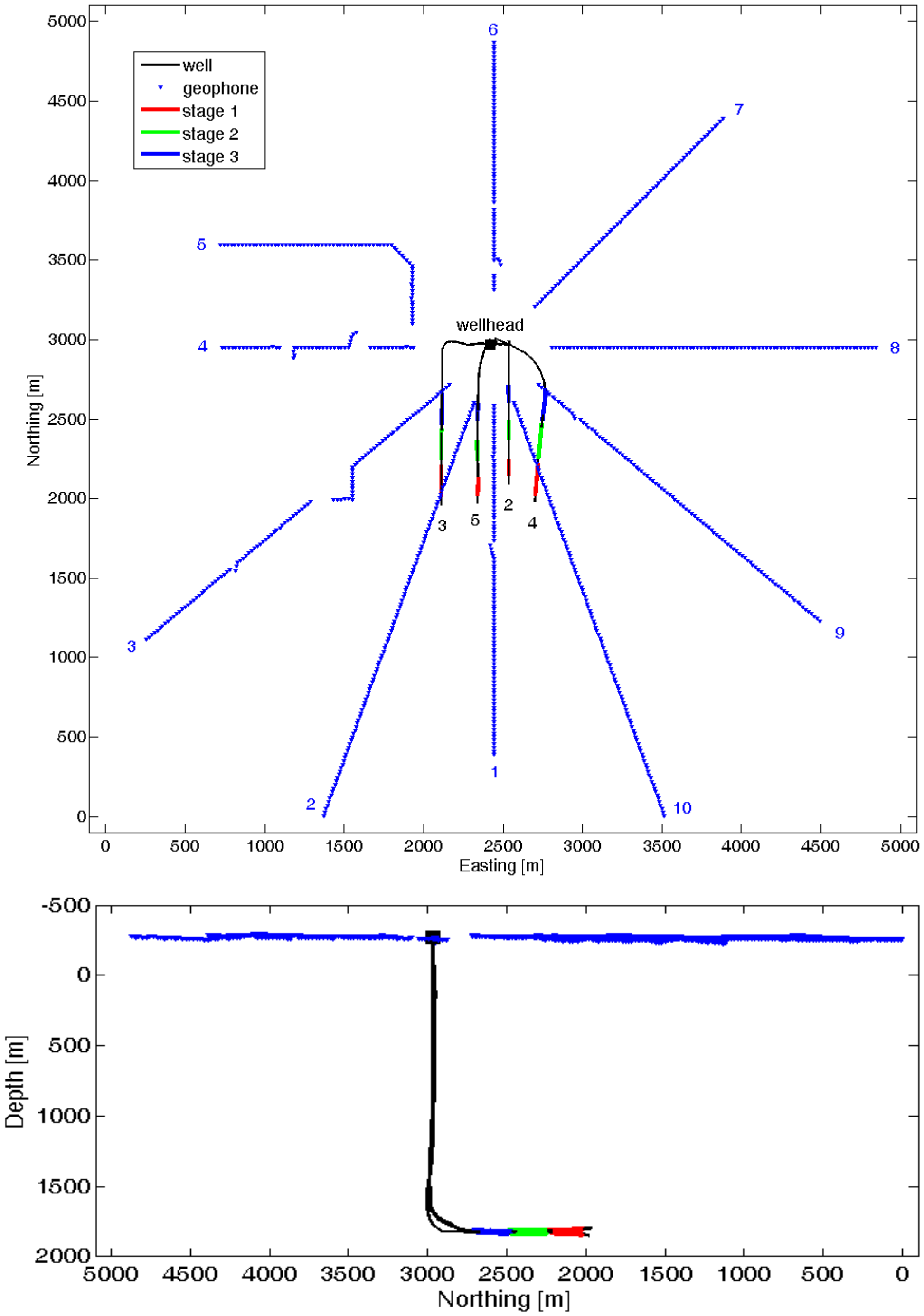

Figure C.1. Four stimulated wells (numbered from 2 to 5) with highlighted stimulation section corresponding to the 12 stages and 10 lines of 911 receivers. Black lines show 4 wells 2, 3, 4, and 5. Red, green and blue parts of horizontal wells represent the first, second and third stage, respectively. Blue triangles are receivers at the surface.

More than 600 events with minimum magnitude -1.7 were detected and located during and after the pumping (Anikiev *et al.*, 2014; Staněk, Anikiev, *et al.*, 2015), all of which are considered induced by the stimulation process. Figure C.2 shows the time evolution of the pumping pressure with the cumulative number of detected events. It is obvious that most of the activity occurred during the fracturing of the first stage of well 2 (2HS1). During this stage, nearly 200 events were induced, which is approximately one third of the total number of events. On the other hand, the stimulation of well 3 did not induce any significant number of events, and the cumulative number does not rise sharply. For further detailed analyses, we chose the 75 strongest events from all detected events that are clearly visible within the raw data without signal enhancement, that is, the events with high SNR. Therefore, we are sure that we used only real events and not weak events, which might be false-positive detections resulting from a random stack of seismic noise (Kushnir *et al.*, 2014). This choice of events allowed us to manually pick the arrivals from individual receivers at the surface, and at the same time, the set of 75 events is sufficiently large to characterize the induced seismicity. The selected microseismic events have moment magnitudes from -0.5 to 0.3, with an average of -0.2. Although these values are relatively high, and we use the strongest events, the magnitudes do not exceed the range of magnitudes regularly induced by hydraulic fracturing (Warpinski *et al.*, 2012).

The time of occurrence for each of the selected events is shown in Figure C.2. Most of the selected events (44 of 75) were induced during the stimulation of well 2, 41 of which were induced during the first stage as discussed above. We also studied 11 events that occurred after the stimulation, during the so-called flowback, that is, during the time when the wellhead was open and the fluids were flowing back to the surface. For all the selected events, we manually picked the maximum amplitude of the P wave arrival on as many traces as possible (of a maximum of 911). Since the receivers had been deployed very close to each other, consistency of the picks was the main criterion of checking the quality of the picks. The picked amplitudes smoothly varied in size between neighboring receivers, and the polarities changed only across nodal lines (an example is shown in Figure C.3), as expected for a continuous seismic wavefield. This approach helped us to find the correct amplitudes even for relatively noisy traces where we could hardly have picked the first arrival if it had only been recorded by a single receiver. When we were not able to reliably recognize the first arrival, for example, on traces recorded by geophones lying close to nodal lines or on very noisy traces, we did not pick the amplitudes and consequently did not use these traces in the source mechanism inversion. The main sources of noise were the pumps and the road cutting across the receiver lines in the east part of the array. On these traces, we might have picked the amplitudes affected by noise but with correct polarity coherent with less noisy traces of geophones placed nearby. In this way, we obtained 75 sets of P-wave arrivals (one set for each selected event) with different magnitudes and polarities, which we used as inputs for the inversion of the source mechanisms.

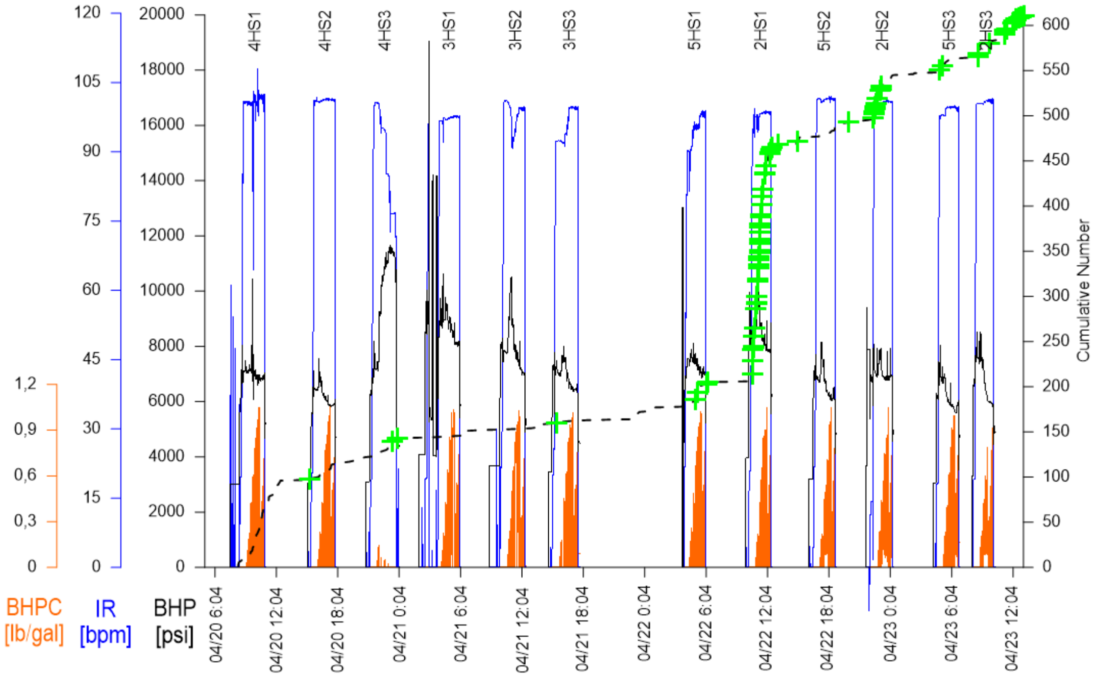

Figure C.2. Computed bottom hole pressure (black - BHP), injection rate (blue - IR), borehole proppant content (orange - BHPC) measured during the hydraulic fracturing of 12 stages on the wells 2, 3, 4 and 5 and cumulative number of detected events (dashed black line). Green crosses show origin times of the 75 events selected for detailed analyses in this study.

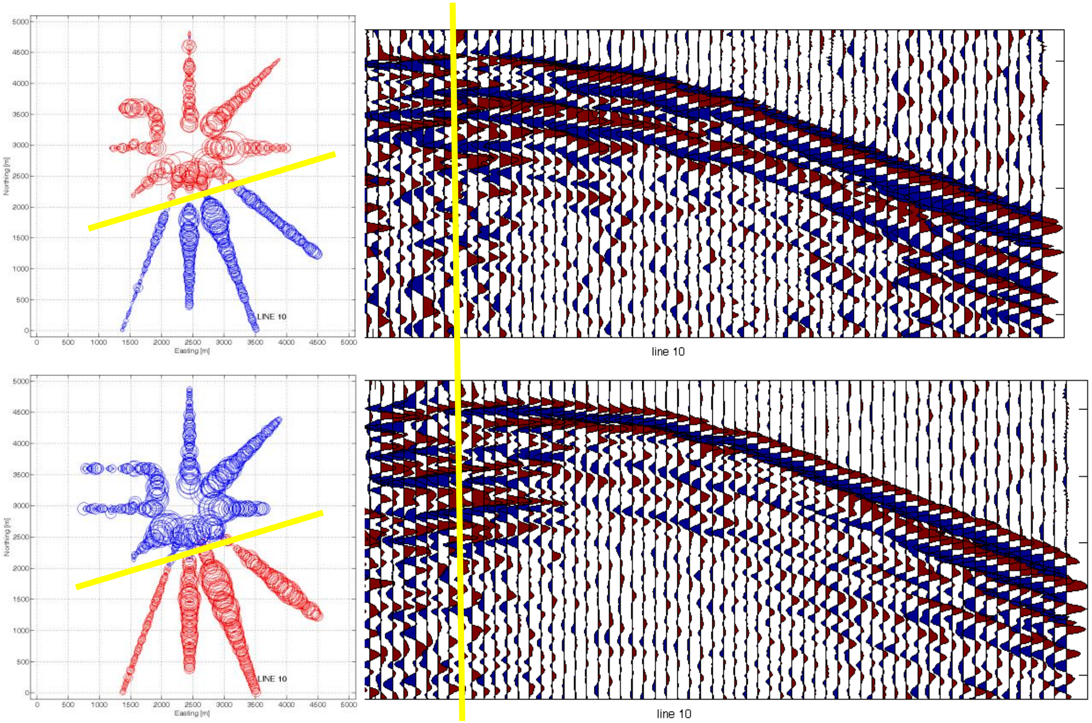

Figure C.3. Manually picked amplitudes of P-wave arrival (on the left) and raw data example recorded on line number 10 for two opposite source mechanisms. Blue and red circles indicate first motion up and down, respectively. Size of circles is proportional to amplitudes. Yellow lines represent approximate position of the nodal lines.

C.3 Moment tensor inversion

We employ wavefront tracing to model the propagation effects through a general 3-D anisotropic media. The rays are computed in an isotropic model with a smoothed 1-D P-wave velocity profile derived from an active 3-D seismic survey. The velocity model is also calibrated using the perforation shots. The velocity is increasing with depth, which affects the raypaths traveling from a source point to the receivers, as is shown in Figure C.4. Using ray parameters, such as the traveltime, trajectory, and slowness vectors, we construct the impulse response of the media, the derivative of the Green's function (Staněk *et al.*, 2014). We use two types of moment tensor inversions for the direct P-wave amplitudes: the first type of inversion is for the full moment tensor, while the second type of inversion is for the pure shear mechanism. The full moment tensor can describe any type of source mechanism ranging from volumetric (e.g., explosion) to pure shear (e.g., a common earthquake). The second type of inversion is restricted to finding a pure shear mechanism that best generates a least-squares fit of the P-wave amplitude and phases. The pure shear mechanism is found using a grid search with a 5° step in all three of the angles—strike, dip, and rake. The obtained source mechanisms are described by the strike, dip, and rake angles of two equal-potential fault planes (the fault plane and auxiliary plane) and by the scalar seismic moment. Obtained full moment tensors are furthermore decomposed into isotropic (ISO), double-couple (DC), and compensated linear vector dipole (CLVD) components following Vavryčuk (2001). In this decomposition, the mechanisms inverted using the second type of inversion, which constrains the source to pure shear with 100% DC components. Finally, we compute an L2 norm misfit to express the quality of the inversion for the resulting moment tensor.

We invert the moment tensor from the P-wave amplitudes alone. The stability and feasibility of the source mechanism inversion for this data set (including the geometry of the receivers) were studied by Staněk *et al.* (2014), who showed that the method provides very stable results even for events with low SNR. Although an inversion utilizing S-waves may further stabilize the moment tensor inversion, it may also introduce significant errors due to unknown S-wave velocity and attenuation models.

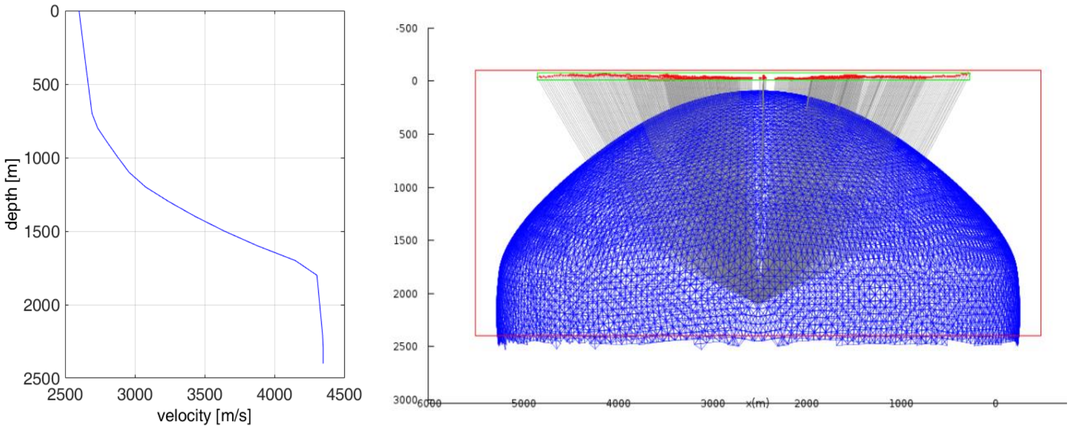

Figure C.4. 1D P-wave velocity profile and modeled rays through the 3D medium. Ray trajectories (grey lines) travel from a point source in depth of 2100 m to receivers (red dots) at the surface. The blue triangulated surface represents a wavefront.

C.4 Results of source mechanisms inversion

Inverting 75 amplitude sets, we obtained 150 mechanisms; one full moment tensor (FMT) source mechanism and one pure shear source mechanism (DC) for each event.

C.4.1 FMT source mechanisms

Figure C.5 shows a map view of the double-couple components of the FMT source mechanisms. Sixty-two of these mechanisms can be characterized as dip-slip mechanisms, while the remaining thirteen mechanisms can be characterized as strike-slip mechanisms. Eleven of these strike slips occurred during the flowback following the completion of hydraulic stimulation for all of the wells. The dip slips are not all the same, as we observe two groups with opposite senses of motion along the fault plane. For an assumed vertical fault plane, one group demonstrates a northern half with the first motion down, while a second group exhibits a northern half with the first motion up. An example of the observed amplitudes with opposite dip slips is shown in Figure C.3. This means that both groups of dip slips have very similar strike and dip angles but differ in rake by approximately 180°. The dip-slip events show both reverse and normal faulting. The strike-slip events seem to have their shear components oriented more favorably toward the regional stress field.

The orientation of the shear components of the FMT mechanisms is summarized in the rose diagrams of Figure C.5. The upper diagram shows the dominant orientation of strike angles of the steeper planes (i.e., planes with greater dip angles) along an ENE-WSW direction. This trend is consistent with the regional maximum horizontal stress direction retrieved from breakouts measured in wells adjacent to the locality (Heidbach *et al.*, 2008; Waters *et al.*, 2009). The dip angles shown in Figure C.5 range mostly from 80° to 90° for the steeper dipping planes and from 0° to 20° for the lower dipping planes. For dip-slip events, this means that either the real fault or auxiliary plane is nearly vertical or nearly horizontal. The strike-slip events are characterized by planes that are both nearly vertical—see the set of 14 events with both nodal planes displaying 80° to 90° dips.

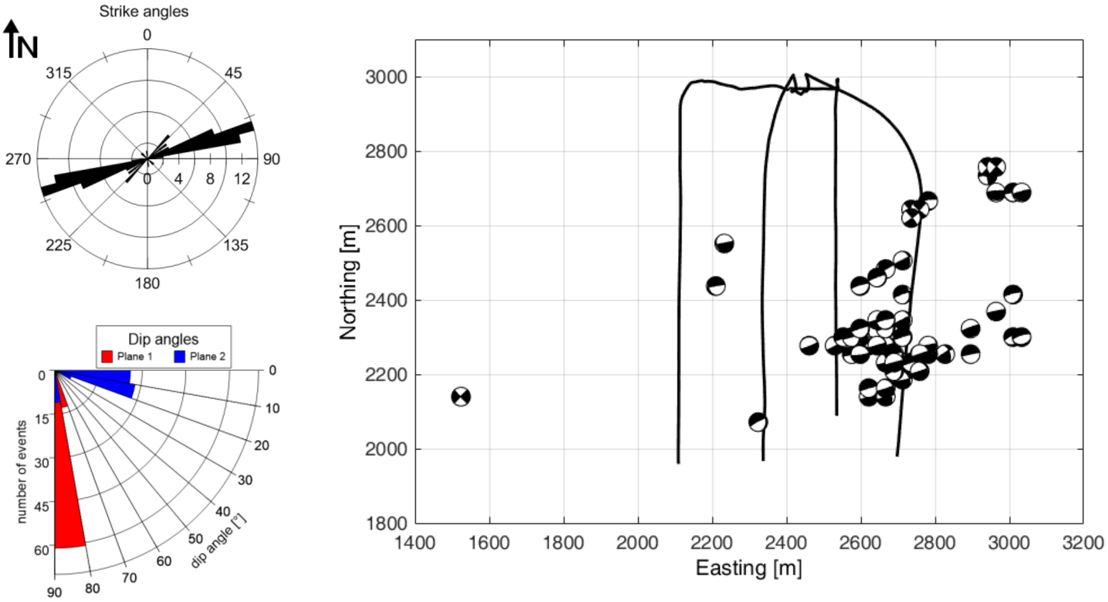

Figure C.5. Rose diagrams and Map view of the selected 75 FMT mechanisms – only the DC component of the FMT is shown. Rose diagrams on the left show strike and dip angles of the steeper dipping plane (plane 1) and shallower dipping plane (plane 2).

FMT mechanisms have DC, CLVD, and ISO components. The percentages of these components are represented by 75 tricolored columns in Figure C.6. We use the absolute values of percentages to get 100% in sum. The DC component dominates most of the inverted FMT mechanisms, indicating that the least squares inversion reveals the events to be more shear than nonshear. The CLVD component is, in most cases, larger than the ISO component. There are seven events with ISO plus CLVD, that is, the non-DC components, that together are greater than the DC components. While these events may seem to be the results of shearing combined with tensile opening or closing, a more detailed analysis suggests that these results can also be explained by noise.

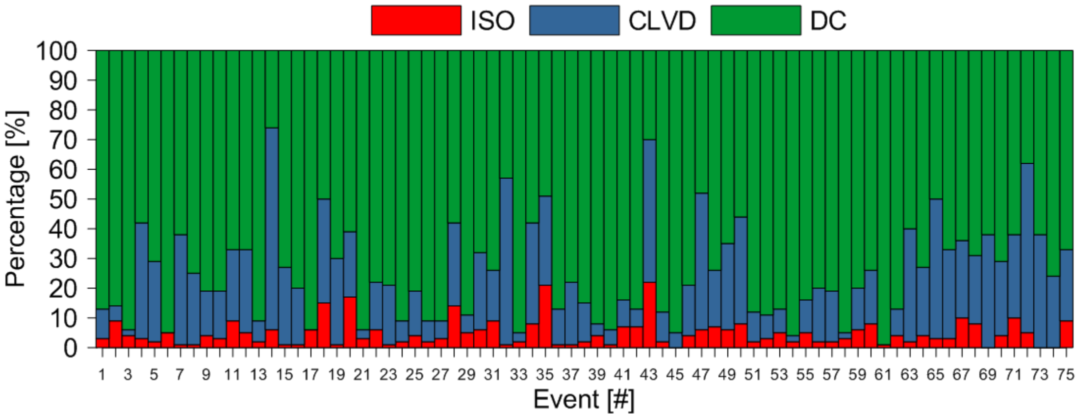

Figure C.6. Decomposition components of FMT mechanisms.

C.4.2 Stability of source mechanisms

Figure C.6 suggests that some microseismic events induced by hydraulic fracturing are mostly shear and that some are a mixture of shear and nonshear mechanisms. However, such an impression may result from an inversion of noisy data sets, and it is well known that noise contributes to the nonshear components of the FMT mechanisms (Dufumier & Rivera, 1997; Staněk *et al.*, 2014). We want to explain the observed data and to separate the real source parameters from artifacts due to noise in the data, poor knowledge of the source location, or assumptions and simplifications throughout the entire inversion procedure. One particular question is whether the non-DC components of the FMT mechanisms are real. The systematic biases in the inversion may also affect the orientations of shear components of the FMT mechanisms. There are many uncertain inputs that might have an effect on the final result, that is, the source mechanism. We discuss the most important of these inputs: mislocation, mismodeling, and noise effects.

The problem of mislocation was stated as less important in comparison with mismodeling by Šílený (2009), who tested a source mechanism inversion with data from a sparse surface network installed to monitor an enhanced geothermal system. We use event locations based on a migration-type technique (Anikiev *et al.*, 2014), which is accurate and precise in a horizontal plane. In the vertical direction, the location uncertainties are lower than the mislocations (470 m) tested by Šílený (2009). Therefore, we do not expect the presence of any significant effects of mislocation on the inverted source mechanisms.

The effects of an incorrect velocity model were investigated by Staněk *et al.* (2014) by inverting the same sets of P-wave arrivals in different models. This study shows that we can obtain reliable FMT mechanisms even when we use the simplest homogeneous velocity model (ignoring weak anisotropy and layered velocity structure) instead of an anisotropic VTI model. The authors also investigated the effects of noise and showed that realistic noise levels are the main limitation for surface arrays. Their study showed that we can retrieve reliable FMT mechanisms for events above certain levels of SNR on individual receivers. With a low SNR, the stability is driven mainly by noise, which causes an increase in the non-DC components. For events with SNR > 1 on individual receivers, the authors showed that the nonshear components due to noise are lower than 20%. Staněk *et al.* (2014) also demonstrated a dependency of the inversion stability on the type of source mechanism and found that the inversion of strike-slip mechanisms is more stable than the inversion of dip-slip mechanisms.

We test the stability of the FMT solution in two ways. First, we compare the potential increase of an L2 misfit between a FMT mechanism and a DC mechanism to estimate whether the additional degrees of freedom in the FMT mechanisms fit the data significantly better. Second, we estimate the spurious non-DC components due to noise for the inverted pure shear components of the FMT mechanism. These tests are designed to determine whether the observed non-DC components of the FMT mechanisms are real.

C.4.3 Comparison of FMT mechanisms with DC mechanisms

Both source mechanisms, that is, the FMT and DC mechanisms, are the results of an inversion of one amplitude set (for each event). When the DC source mechanism provides statistically similar L2 misfit data as the FMT source mechanism, we can state that the nonshear components are not required to fit the data and that the source mechanism is predominantly shear or nearly pure shear. The difference in the orientation of two source mechanisms can be measured using the 3-D rotation angle (the Kagan angle in this study) (Kagan, 1991). The Kagan angle is the minimum rotation angle needed to rotate one double couple into another arbitrary double couple in 3-D. Figure C.7 shows the results of such a comparison of L2 misfits and orientations. There are 34 events (i.e., 45% of the data set) with differences in the L2 misfits lower than 2% in addition to differences in the orientation lower than 5°. Because these differences are very small, we consider these events to be pure shear, and the nonshear components of these events are most likely false. There are only dip slips among them, and therefore no strike slips (i.e., more than 55% of the dip-slip events are pure shear). The other mechanisms display higher differences, indicating at least partly real nonshear components for the FMT mechanisms. Note that we observe a very low Kagan angle when an L2 misfit difference is lower than 2%. However, a low Kagan angle does not result in a low difference in the L2 misfits probably because higher L2 misfits may be caused by random noise without affecting the stable DC components of the FMT mechanisms. We note that the FMT mechanism always fits observed data better than the pure shear mechanism since it has 2 additional degrees of freedom with which to fit the data. These results give us a way of checking whether the non-DC components of the FMT mechanisms are real.

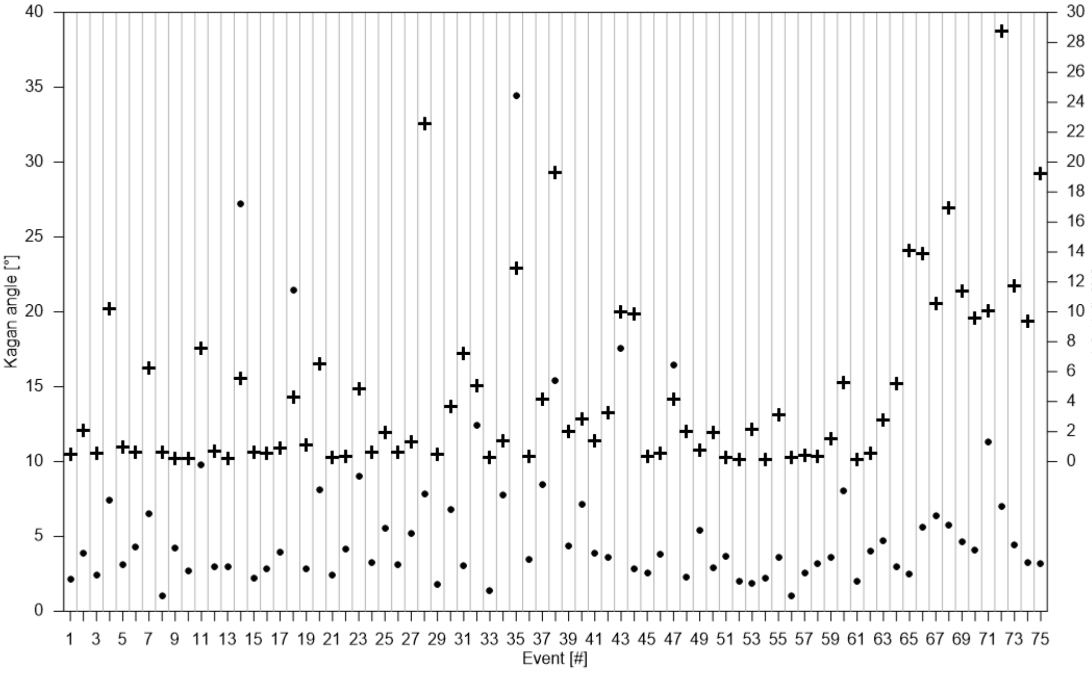

Figure C.7. Kagan angles (dots) and difference of L2-misfits (crosses) between FMT mechanisms and DC mechanisms.

C.4.4 Estimation of spurious non-DC components of FMT mechanisms

In the second test, we assess the effects of the presence of real noise in the data and the type of source mechanism. We model the amplitudes according to the pure shear source mechanism of the FMT, add real noise amplitudes, and again invert for the FMT mechanisms. The non-DC components of such FMT mechanisms are estimates of spurious nonshear components due to real noise. To add the appropriate level of noise, we take 50 samples of waveforms before the picked arrival and add them to the synthetic amplitudes. In this way, we create 50 synthetic amplitude sets with different random noise amplitudes for every source mechanism. Among all the 50 FMT inversions of modeled synthetic amplitude sets, we compute an average and take the minimum and maximum of the possible nonshear components for each source mechanism. These values are subsequently the limits of the expected nonshear components for the pure shear source mechanism inverted from our real data. Note that we test the effects of noise and the mechanism type only, not the effects of mismodeling or mislocation.

Afterward, we compare the non-DC components of the FMT mechanisms inverted from the real data to the non-DC components estimated for the pure shear source mechanism due to a given noise level and source mechanism type. When the obtained non-DC components are similar to the average value or are at least in the range between the maximal and minimal values of the non-DC components due to noise, we consider such a microseismic event as pure shear because the non-DC components can be fully explained to be a result of noise. On the other hand, when the value is out of this range, the event is at least partly nonshear.

In Figure C.8 we show the limits (i.e., the maximum values of ISO and CLVD and the minimum value of DC) of the percentages of spurious non-DC components, as well as the percentages of the FMT mechanisms for real events. There are 12 events for which the percentages are within the limits for pure shear mechanisms. Another 17 events are within the nonshear limit created by merging the ISO and CLVD limits together. We primarily observe the DC component, as the decomposition of ISO and CLVD is not reliable, and we can therefore conclude that 29 of the observed events are most likely pure shear. The remaining events have at least a small portion of nonshear components that were caused by something other than the noise within the data.

A large number of source mechanisms have a significant part of nonshear components that are explainable as spurious and therein primarily caused by noise. To demonstrate this, we subtract the estimated spurious level of non-DC components from the FMT mechanisms inverted from the picked P-wave amplitudes (Figure C.9). In this graph, the ISO and CLVD components are presented together as nonshear components. All 75 tested events exhibit, on average, 89% of the observed amplitudes as a consequence of a pure shear source (including the effect of noise), wherein 63 dip slips have 92% DC on average, and 12 strike slips have 69% DC on average. Nearly half of the dip slips are pure shear, 82% of which have DC percentages higher than 80%. The source mechanisms colored by the corrected DC percentage are shown in Figure C.10, where the hotter color indicates a higher DC.

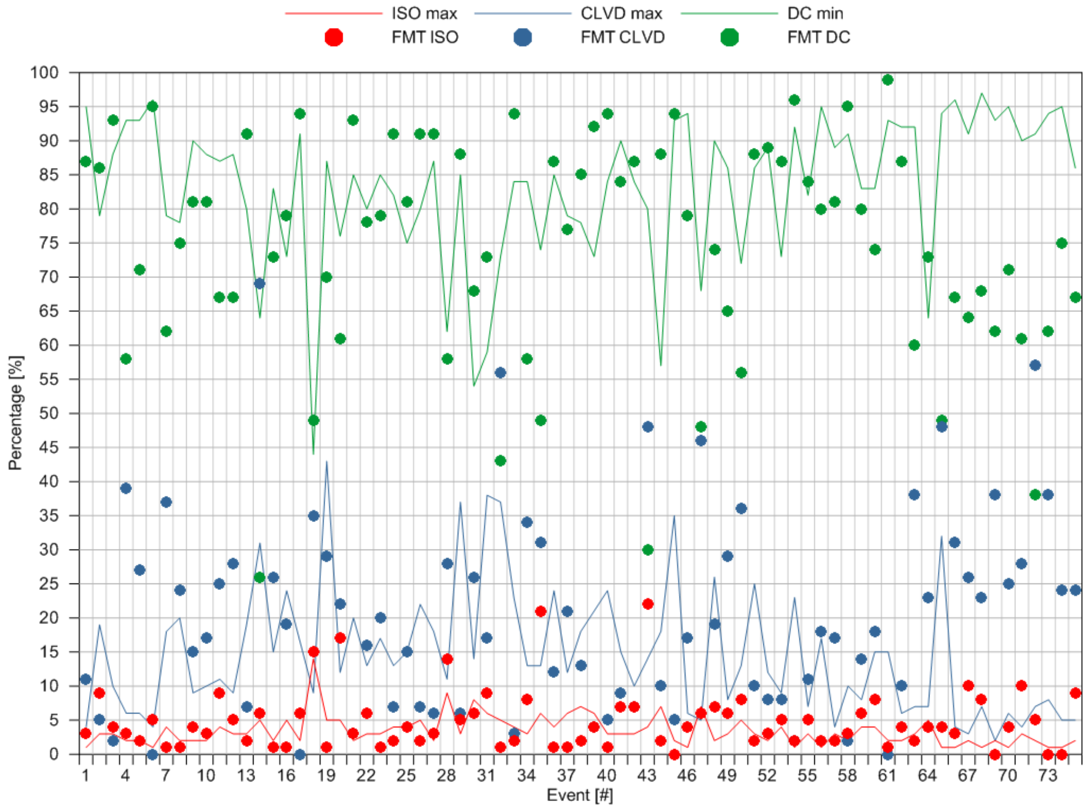

Figure C.8. Limits of expected percentages for DC mechanism (lines) and obtained percentages (points) of FMT mechanism.

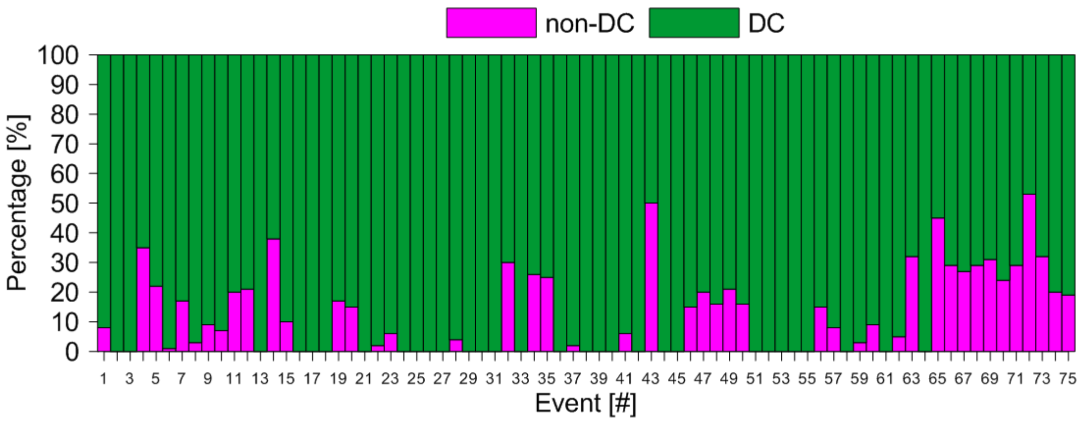

Figure C.9. Decomposition components DC and non-DC of FMT for the studied events.

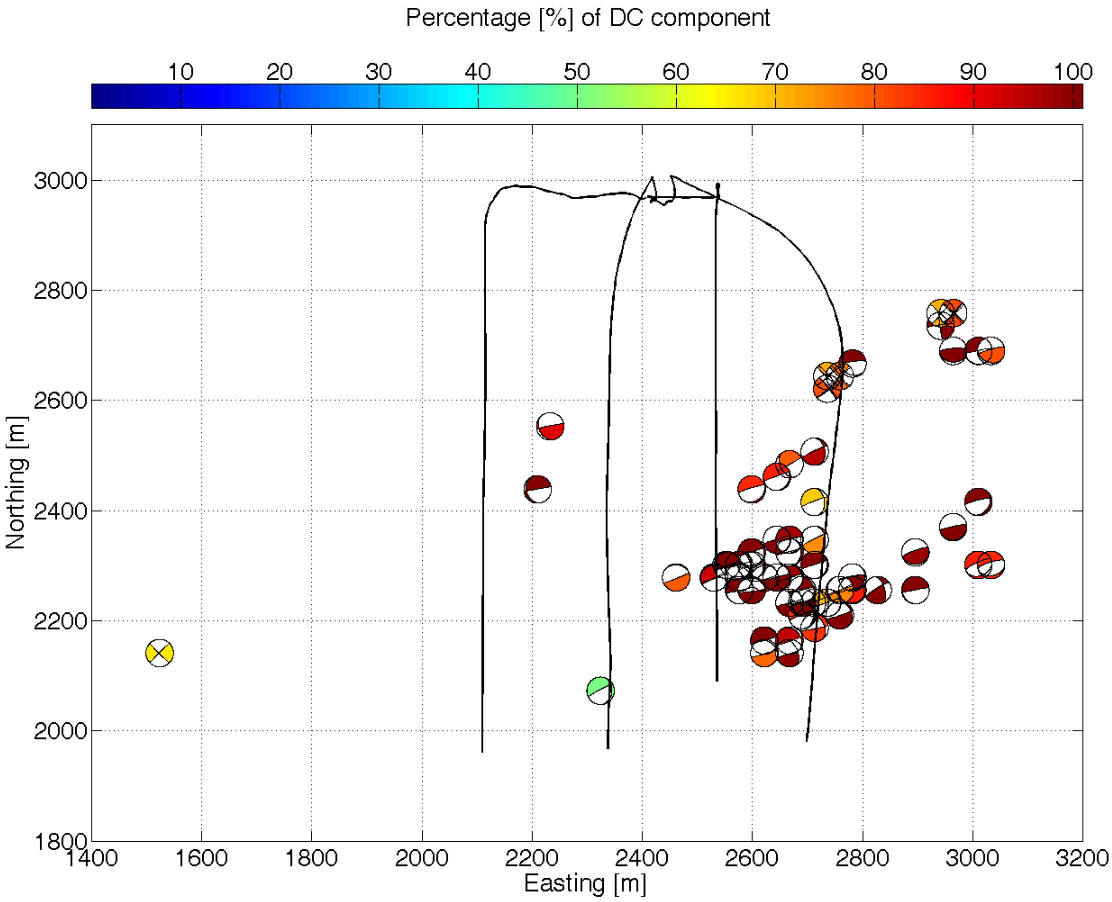

Figure C.10. Map view of 75 source mechanisms color coded dependently on corrected DC percentage.

C.5 Interpretation – the bedding plane slip model

The induced seismicity is interpreted with models that use event locations, source mechanisms, geological knowledge, and the state of stress at the given locality. For example, the source mechanisms are used to create a discrete fracture network, for example, Williams-Stroud *et al.* (2013). We know that the source mechanisms of shear events can constrain the orientations of fault planes and the direction of slip. The locations of events determine the direction of fracture propagation and the fracture length.

There are five widely accepted models that describe the relationship between seismicity and hydraulic fracturing:

1. The first model interprets microseismicity as the product of failure along preexisting fractures, in which pore pressure was elevated by a diffusion process surrounding the hydraulic fracture (e.g., Pearson, 1981; Shapiro *et al.*, 2006; Warpinski *et al.*, 1998). In this model, microseismicity is a cloud of events around a hydraulic fracture induced along preexisting natural fractures ready to slip (shear). Microseismic events are driven mainly by tectonic stresses.
2. The second model can be called fracture loading (Hill, 1977; Rutledge *et al.*, 2004). It assumes that the opening of the hydraulic fractures is aseismic but that microseismic events originate along preexisting natural fractures connecting the aseismic hydraulic fractures that are also loading their strike-slip shearing. This model explains the observed opposite polarities on fault planes slightly inclined relative to the stress field.
3. The third model is based on tensile opening and closing that directly result from hydraulic fracture opening characterized by source mechanisms that have variable orientations due to heterogeneous stress changes in both space and time (e.g., Baig & Urbancic, 2010). The evidence of tensile opening during hydraulic fracturing was also presented by other studies, e.g., Eaton *et al.* (2014), Pesicek *et al.* (2016), and van der Baan *et al.* (2016).
4. The fourth model of Eisner *et al.* (2010) explains that dip-slip events with opposite mechanisms are a result of the aseismic opening of horizontal fractures. Dip-slip events occur along nearly vertical fault planes, forming

mini grabens. Such source mechanisms have a dominant shear component but require that the hydraulic fracture pressure must overcome the vertical stress.

5. The last model is a model of bedding plane slip. It is a geomechanical model proposed by Staněk and Eisner (2013) and Rutledge *et al.* (2013) to explain microseismic dip-slip mechanisms as the product of slippage along bedding planes. This model was also discussed by Tan and Engelder (2016), who concluded that their observations are broadly consistent with the model. These studies used observed data to create their models, while the theoretical model for bedding plane slip was proposed by Chuprakov and Prioul (2015), Gu *et al.* (2008), and Harper and Last (1990).

The bedding plane slip model is based on geological characteristics common for most shale reservoirs. Shale is a sedimentary rock, and it has a dominant horizontal bedding structure with many layers with various thicknesses. In addition, the connection between these layers is well known to be the weakest plane. Outcrops of the Woodford formation (Vincent, 2010) exhibit visible layers of organically-rich brittle shales with two distinct sets of natural fractures—one continuous fracture parallel to the dip direction of the bedding plane and one represented by poor continuity in the vertical direction within the more compact and uniform layer. The vertical fracture orientations correspond to the current maximum stress direction in this region as reported by the World Stress Map project (Heidbach *et al.*, 2008).

Figure C.11 illustrates the bedding plane slip model with an aseismic opening of the vertical fracture and subsequent bedding plane slippage. A vertical rupture is opened by hydraulic fracturing against the minimum horizontal stress. This opening is done aseismically—we do not detect it because the tensile opening is too weak (e.g., Cornet & Jianmin, 1995). The newly created fracture propagates from the injection point along the direction of the maximum horizontal stress, which is consistent with the observed event locations. Such fractures can be hundreds of meters long. The microseismic events are located along the aseismically opened fracture. This hydraulic fracture perturbs the stress field in its immediate vicinity and creates shear loading on the weak bedding planes. This finding is consistent with the fact that we observe the dip-slip events located within the reservoir layer during the hydraulic fracturing stage. The hydraulic fractures load the bedding planes to slip against the minimum horizontal stress, which accounts for the strike angles of the steeper planes that parallel the direction of the maximum horizontal stress. We propose that the horizontal plane is the fault plane, since it is oriented (within the location uncertainty) along the weak bedding planes in the shale. The slippage along these planes is caused by accumulated stress created only by the slow opening of the vertical fractures, which limits the microseismicity to occur only within the vicinity of the hydraulic fracture because there is no regional shear stress on these planes. Additionally, the Woodford shale and generally all successfully producing shale formations are considered overpressured reservoirs (e.g., Agrawal, 2009); therefore, the minimum horizontal stress is close to the vertical stress. It is possible that hydraulic fractures locally perturb the vertical stress and induce bedding plane slippage. The shear motions may also occur along the two faces of hydraulic fractures due to the pressure applied to materials with slightly different stiffness parameters, resulting in stress discontinuity. The bedding plane slip model also explains commonly observed repeated events (multiplets) in a similar location in the vicinity of the opened fracture with very similar source mechanisms. Although the horizontal fault plane is less likely to slip using a simple geomechanical model (Zoback, 2007), the weak bedding planes can explain why this plane can slip, as has been shown in many geomechanical models: Chuprakov and Prioul (2015), Gu *et al.* (2008), and Harper and Last (1990).

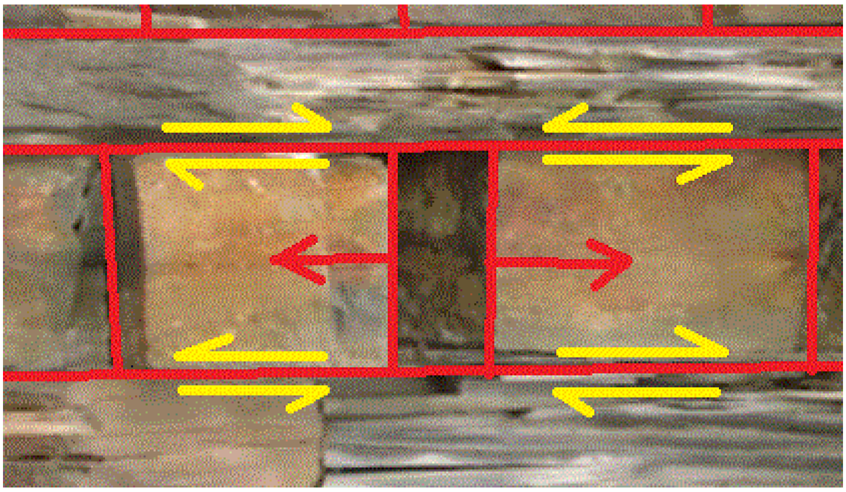

Figure C.11. Model of aseismic opening of the vertical rupture and subsequent bedding plane slippage

The observed strike-slip events following hydraulic stimulation are probably resulting from the reactivation of preexisting faults, as they are more favorably oriented along the current stress field. Strike-slip events are located deeper and farther away from the injection point. The fact that we observe nonshear components in these events supports the idea that the fracture intersected a preexisting natural fracture (e.g., Gu *et al.*, 2011; Keshavarzi & Jahanbakhshi, 2013). The non-double-couple components also imply that the hydraulic fracturing pressure is comparable to the maximum stress, as the injection pressure exceeds the maximum horizontal stress.

The bedding plane slip model also explains the low amount of total radiated seismic energy or low seismic efficiency (Maxwell, 2014). The total input energy, computed as the cumulative product of the injected fluid volume and pressure, is usually much higher (105 times) than the energy of the observed seismicity. Our model is consistent with the majority of the injected energy being spent toward the aseismic opening, and the bedding plane slip is only a side effect of this opening. This model fits with the fact that a significant amount of proppant is pumped down into the fracture system to keep it permeable, which is stored mainly within the vertical fracture.

C.6 Conclusions

We studied the source mechanisms of microseismic events induced by hydraulic fracturing of a typical shale formation. We observe mainly dip-slip types of events induced during the stimulation, and a few strike-slip events that occurred soon after fracturing. The dip-slip events have mechanisms with steeper nodal planes oriented nearly vertically in the direction similar to the maximum horizontal stress. We carefully tested the reliability of the obtained nonshear components by comparing L2 misfits between pure shear and general full moment solution mechanisms and by computing the expected nonshear component due to noise in the data. We show that 90% of the observed moment released by these microseismic events can be explained by pure shear failure; in fact, more than 50% of the observed dip slips are likely pure shear.

We explain that the shear dip-slip events are the result of bedding plane slip along preexisting weak bedding planes loaded by the aseismic hydraulic fracture opening. This model can explain events located along the fracture as well as the multiplets and the orientation of the observed nodal planes with respect to the stress orientation. This model agrees with a large amount of fluid containing proppant being pumped into the reservoir, which is then stored in the aseismic vertical fracture. The observed strike-slip events probably resulted from the reactivation of favorably oriented preexisting fractures or faults.

Outlook

Microseismic data interpretation - what do we need to measure first?

Published in *First Break*, in 2018,
Volume 36, No. 2, 55 – 58.

Leo Eisner[1] and František Staněk[2,3]

[1] Seismik s.r.o., Prague, Czech Republic

[2] Czech Academy of Sciences, Institute of Rock Structure and Mechanics, Dept. of Seismotectonics, Prague, Czech Republic

***[3]** Charles University, Faculty of Mathematics and Physics, Dept. of Geophysics, Prague, Czech Republic*

Currently, there are four widely discussed theories used to describe how microseismicity interacts with hydraulic fracturing. Each theory has a different implication for the interpretation of microseismicity used for reservoir modeling. Therefore, better understanding of the relationship between microseismicity and hydraulic fracture stimulation is needed before further reservoir models are developed and applied. This would lead to a more precise estimation of hydrocarbon production and give greater value to microseismic data. We may use either seismic or non-seismic methods. While non-seismic methods provide an independent view of hydraulic fracturing they only provide a limited amount of information on the relationship between hydraulic fracturing and microseismicity. We propose microseismic monitoring of directivity as the most promising way to determine the orientation of fault planes and associated slip vectors. Although this is a suitable method it requires sensors in multiple azimuths that are well coupled to obtain reliable high frequency signals. We suggest using Distributed Acoustic Sensing (DAS) sensors which are capable of sampling high frequency and may provide continuous data along long offsets at reasonable costs.

O.1 Introduction

Hydraulic fracturing stimulation is accompanied by induced microseismic events resulting from the reactivation of pre-existing fractures or the creation of new fractures (e.g. Grechka and Heigl, 2017). Locations of microseismic events are then used to map the fracture geometry: the direction of fracture propagation, fracture length and height. Numerous authors and companies try to convert the measured microseismic information into estimations of reservoir production. These approaches use microseismicity to constrain linear and non-linear diffusion (e.g., Grechka at al., 2010), discrete fracture networks (Williams-Stroud *et al.*, 2013), tensile opening of hydraulic fracture (Baig and Urbancic, 2010), or bedding plane slip (Rutledge *et al.*, 2013; Staněk and Eisner 2013). Many of these approaches try to directly map microseismicity to production prediction and other highly valuable information but the reality of the current state of the art is that we do not know the exact nature of microseismicity and hydraulic fracture interaction with microseismicity. Therefore, many of the reservoir simulators based on microseismicity are subject to significant uncertainty. An important role in the determination of interaction between microseismicity and hydraulic fracture may be determined by better constraining the seismic signals and removing part of the uncertainty from both microseismic locations and additional information contained in the recorded seismic signal – the source mechanisms. Specifically, we may exclude some of the above-mentioned models if our inverted data is more precise or at least more accurate. Microseismic locations are often interpreted as a diffused cloud of widely activated fracture networks, while misinterpreting location errors with diffusion process (e.g. initial locations in Rutledge and Phillips, 2003). Similarly, there are doubts as to whether the non-shear components of microseismic events induced by hydraulic fracturing are real or the result of erroneous processing (e.g. differences in observation of Baig and Urbancic (2010) and Grechka *et al.* (2016) vs. Staněk and Eisner 2017). The main challenge in improving downhole acquired microseismic locations is downhole velocity model as wave propagation along horizontal layers is not suitable for commonly used ray tracing methodologies (e.g., Klimeš, 2012) and the high frequency content of recorded waveforms is compromised with trapped waves and clamping issues resulting in poor azimuthal measurements (e.g. Janská *et al.*, 2014). Additionally, poor azimuthal measurements as a result of single vertical monitoring borehole must be resolved with multiple monitoring boreholes or lateral array. Surface monitoring is usually compromised by relatively high levels of noise and lack of high frequency content as it is attenuated along a path to the surface.

The models of the interaction between microseismicity and hydraulic fracture result in different constraints to the reservoir model. i.e., the same observed seismicity must be interpreted based on the true interaction between hydraulic fracture and microseismicity. Here we discuss what kinds of monitoring can find the true model representing the nature of interaction and develop a more realistic interpretation of microseismic events with greater hopes of matching the production. For example, the bedding plane interpretation of microseismicity allows assessment of the amount of the hydraulic fracture opening as illustrated in Figure O.1a. If this model is valid, seismic moment of a microseismic event is proportional to fracture width. If the diffusion model is right, the width of the microseismic cloud provides important constraint of pore pressure changes in the formation (see Figure O.1b as illustration) and such pore pressure changes can be then used to predict production as they inform us on penetration of fluids through the formation. If the model of Rutledge *et al.* (2004) illustrated in Figure O.1c is valid microseismic events represent choke points of the hydraulic fractures and their seismic moments represent minimum spatial extend of the hydraulic fracture as they are part of the hydraulic fractures. An Alternative model of Eisner *et al.* (2010) explains hydraulic fracture as an opening of a horizontal fracture overcoming vertical stress and microseismicity is shearing almost vertical planes. That would mean that we could measure height of opened fracture from seismic moment of microseismic events. The least widely discussed model interprets microseismic events as tensile opening and closing (Fig. O.1d). Microseismic events are interpreted as a direct result of fracture opening (closing) close to the injection points combined with shearing away the injection. Such seismicity is characteristic with variable orientation of events as it is a random reaction of the reservoir to the stress changes.

Luckily, the above-mentioned models predict differences in observed data and we may be able to differentiate among them if sufficiently good datasets are acquired. In this study, we discuss what needs to be measured before the models are used for quantitative and qualitative production prediction, we want to discuss what kind of acquisition is needed to be able to differentiate between the proposed models and how to acquire such data.

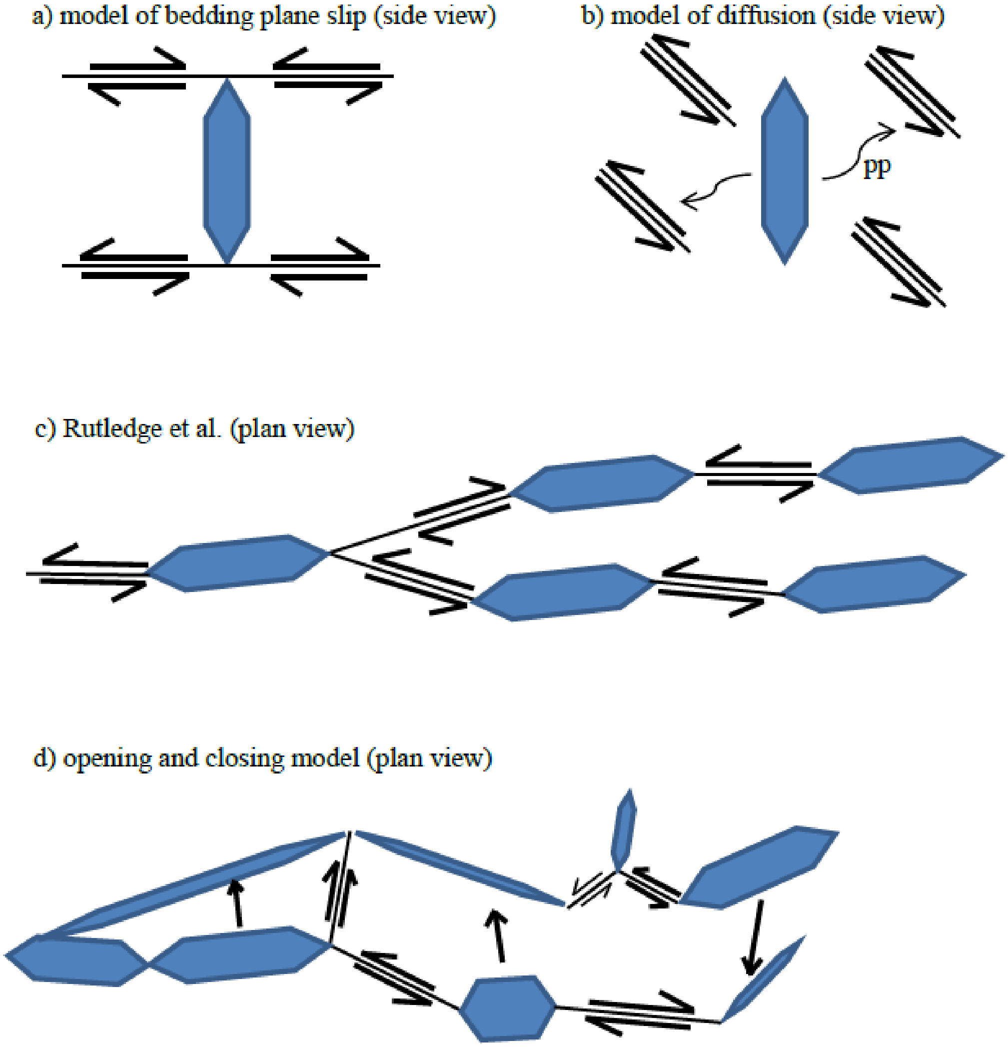
a) model of bedding plane slip (side view)

b) model of diffusion (side view)

c) Rutledge et al. (plan view)

d) opening and closing model (plan view)

Figure O.1 Commonly accepted models of induced seismicity: a) model of bedding plane slip, b) model of diffusion (linear), c) model of Rutledge *et al.* (2004), d) model of opening and closing. The blue objects represent fractures filled with fluids, the black lines shearing along fractures and the black arrows forces causing shearing or fracture closing.

O.2 What can be done

It is possible to drill and core the fractured area close to the treatment well where the microseismic events occur. In some circumstances, it is even possible to imagine a mine back experiment where the fractured area mined back (like potash mines experiments – Warpinski *et al.* 1981). In such experiments, it would be desirable to trace (chemical or other the injected fluids. Core sample from such a well could help us to understand where the fracturing fluid really penetrated and certainly it would differentiate between wet and dry fractures. However, there are two very fundamental problems associated with this experiment: It is extremely difficult to drill through the fault plane of a microseismic event given the uncertainties of the locations of these microseismic events. Even if we were able to drill precisely into the fractured area, we can’t distinguish between fracture opened seismically and aseismically. This experiment would only provide local and incomplete information about the interaction of hydraulic fracturing and microseismicity. Alternatively, we may use a network of sensitive borehole tiltmeters in the close vicinity of the fractured area combined with microseismic monitoring. Note that tiltmeters are sensitive to the volumetric changes due to the hydraulic fracture. Temporal interpretation of tiltmeter changes combined with space and temporal information on microseismic events could provide us a much better understanding of which microseismic events are part of the hydraulic fracture and which events are results of stress changes without volumetric fluid changes. Specifically, we would be able to differentiate between vertical and horizontal hydraulic fractures. Implicitly this would imply which microseismic fault planes are activated by the hydraulic opening. However, uncertainty of inversion of tiltmeter signals grows rapidly with distance from the sensors as the inversion of tiltmeter signals suffers from a large degree of uncertainty resulting from unknown geomechanical properties of the rock formation. Additionally, it would be hard to install tiltmeters in the vicinity around the hydraulic fracture area which would be necessary to constrain the hydraulic fracture image.

As the non-seismic methods seem to have significant drawbacks we turn back to induced seismicity monitoring and interpretation. For example, in seismology there are at least three options on how to overcome uncertainty of differentiation between the fault and the auxiliary planes in the far field approximation:

- Directivity – the use a ‘Doppler effect’ of seismic waves also known as the Haskell model of seismic source directivity. This model uses the anisotropy of the radiated energy to differentiate between fault and the auxiliary planes.
- Locations of aftershocks: aftershocks are usually distributed along the fault, not the auxiliary plane of the earthquake.
- Differentiation between hypocenter (point where the fault started to slip) and the centroid (point where most of the seismic energy is radiated) of an earthquake. Fault plane contains both points while auxiliary plane only contains one of them if at all.
- The Location of aftershocks and hypocenter-centroid methods both require high precision and accuracy of the located events and hypocenter especially in relative positioning resulting in significant subjectivity of results. Let us discuss in more details the directivity as this method uses the anisotropy of far-field seismic energy.

The Haskell model is the simplest representative of this model. The low frequency duration of far-field unilateral Haskell type of fault plane rupture forecasts that the duration time of source rupture is

$$T_r = L(\frac{1}{v_r} - \frac{\cos\alpha}{v_S}) \tag{O.1}$$

where v_r is rupture velocity, v_s is velocity in the source area, L is the length of the rupture and α is the angle between receiver and the slip vector (as shown in Figure O.2). For an estimate of the rupture length 1 m, the S-wave velocity 2500 m/s and the rupture velocity 80% of the S-wave velocity, the difference apparent rupture time T_r between the receiver in the direction of the slip vector and in the opposite direction is approximately 0.0005 s, i.e. one half of a millisecond. Such small difference implies at least two challenges for microseismic monitoring:

- Surface monitoring unless extremely shallow is unlikely to sample signal energy at the frequencies above 100 Hz because it is attenuated.
- Downhole instrumentation must be cemented behind the casing as in the seismic waves at the frequencies above 200-300 Hz interacts with borehole fluids and therefore the measurement of instruments clamped inside the

borehole is compromised. Additionally, it is well known that the instruments have internal coupling resonances at those frequencies, again making the uncemented coupling highly questionable and not suitable to measure amplitude information.

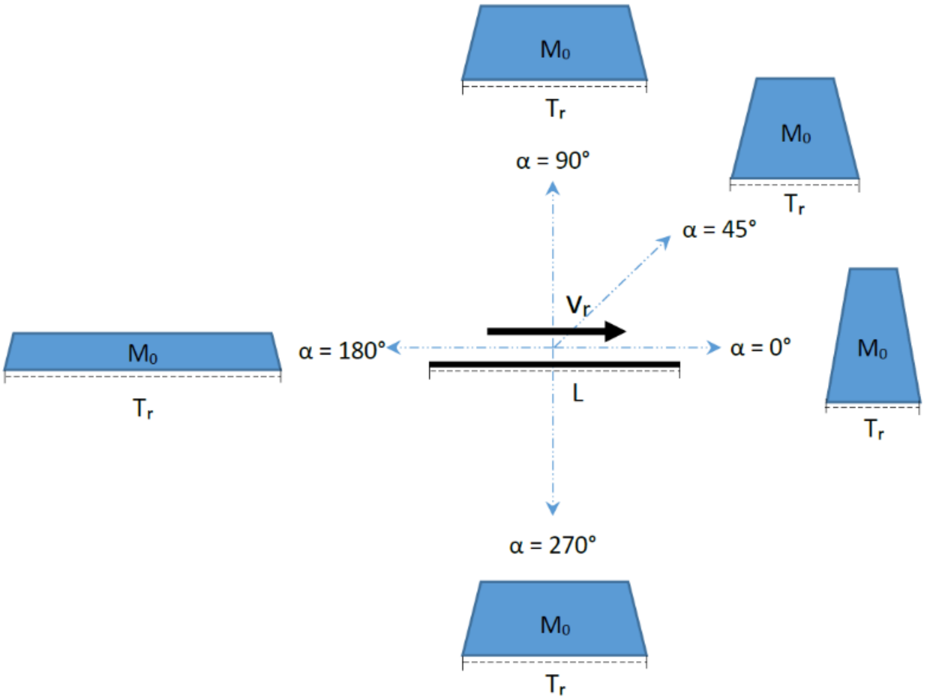

Figure O.2 Source time function of radiated pulse in different azimuths relative to slip vector (v_r).

Therefore, we conclude that only downhole sensors cemented behind casing in several azimuths are likely to sample well enough the seismic signals to differentiate between the discussed models. This experiment would also be extremely expensive to conduct.

Distributed Acoustic Sensing (DAS) sensors may be suitable for directivity resolution and are already developed and readily available: (e.g., Hull *et al.*, 2017; Karrenbach *et al.*, 2017; Starr and Jacobi, 2017). These DAS sensors can be bonded to the casing in the horizontal sections of the boreholes sufficiently close to microseismic events to record the effects of directivity. With DAS, it is possible to measure the strain changes continuously and in real time at acoustic frequencies of several MHz. This means we can achieve sufficient sampling resolution along the entire horizontal section of a well which can be several kilometers in length. The only drawback is the relatively short distance (approximately less than 50 m) between events and sensors to see the radiation directivity.

O.3 Conclusions

Currently, we have at least four competing theories on how microseismicity interacts with hydraulic fracturing. These theories have vastly different implications for interpretation of microseismicity in reservoir modeling. Therefore, a more precise understanding of microseismicity and hydraulic fracturing is needed before further reservoir models are developed and applied. Non-seismic methods provide limited understanding on which model is right. Seismic monitoring of directivity seems to be the most suitable but requires sensors in multiple azimuths that are cemented behind the casing due to high frequency signals. We suggest that the DAS sensors may provide the most promising sensitivity which could lead to differentiation among the proposed models and new improvement of reservoir simulators based on microseismicity.

References

Agrawal, A., 2009. *A technical and economic study of completion techniques in five emerging U.S. gas shale plays*. Master thesis, Texas A&M University.

Aki, K., Fehler, M., Aamodt, R.L., Albright, J.N., Potter, R.M., Pearson, C.M. and J.W. Tester, 1982. Interpretation of seismic data from hydraulic fracturing experiments at the Fenton Hill, New Mexico, hot dry rock geothermal site. *J. Geophys. Res.*, 87(B2), 936–944. doi:10.1029/JB087iB02p00936

Aki, K. and P.G. Richards, 1980. *Quantitative seismology*. Freeman and Co., New York.

Anderson, E.M., 1942. *The Dynamics of Faulting.* 2nd edn, Oliver and Boyd, Edinburgh, p. 206.

Angelier, J., 2002. Inversion of earthquake focal mechanisms to obtain the seismotectonic stress IV—a new method free of choice among nodal planes. *Geophys. J. Int.*, 150, 588-609.

Anikiev, D., Gajewski, D., Kashtan, B., Tessmer, E. and C. Vanelle, 2009. Localization of low-frequency microtremors by a modified diffraction stack. *71st EAGE Conference and Exhibition*, Amsterdam, the Netherlands, p. S040.

Anikiev, D., Staněk, F., Valenta, J. and L. Eisner, L., 2013. Imaging microseismic events by diffraction stacking with moment tensor inversion. *SEG Technical Program Expanded Abstracts*, 391, 2013–2018. doi:10.1190/segam2013-0830.1

Anikiev, D., Valenta, J., Staněk, F. and L. Eisner, 2014. Joint location and source mechanism inversion of microseismic events: benchmarking on seismicity induced by hydraulic fracturing. *Geophys. J. Int.*, 198(1), 249-258. doi:10.1093/gji/ggu126

Artman, B., Podladtchikov, I. and B. Witten, 2010. Source location using time-reverse imaging. *Geophys. Prospect.*, 58(5), 861–873.

Baig, A. and T.I. Urbancic, 2010. Microseismic moment tensors: A path to understanding frac growth. *The Leading Edge,* 29(3), 320-324. doi:10.1190/1.3353729

Bradford, I., Probert, T., Raymer, D., Ozbek, A., Primiero, P., Kragh, E., Drew, J. and C. Woerpel, 2013. Application of Coalescence Microseismic Mapping to

Hydraulic Fracture Monitoring Conducted Using a Surface Array. *75th EAGE Conference and Exhibition incorporating SPE EUROPEC 2013*. doi:10.3997/2214-4609.20131028

Cardott, B.J., 2013. Woodford Shale: From Hydrocarbon Source Rock to Reservoir. *AAPG Woodford Shale Forum*, Search and Discovery Article #50817.

Červený, V., 2001. *Seismic Ray Theory*. Cambridge University Press.

Chambers, K., Clarke, J. and S. Wilson, 2013. Imaging moment tensors from surface arrays. *4th EAGE Passive Seismic Workshop*, Amsterdam, the Netherlands, p. PS10.

Chambers, K., Dando, B. D.E., Jones, G. A., Velasco, R. and S. Wilson, 2014. Moment tensor migration imaging. *Geophys. Prospect.*, 62, 879–896. doi:10.1111/1365-2478.12108

Chambers, K., Kendall, J.M., Brandsberg-Dahl, S. and J. Rueda, 2010. Testing the ability of surface arrays to monitor microseismic activity. *Geophys. Prospect.*, 58(5), 821–830. doi:10.1111/j.1365-2478.2010.00893.x

Chuprakov, D. and R. Prioul, 2015. Hydraulic Fracture Height Containment by Weak Horizontal Interfaces. *SPE Hydraulic Fracturing Technology Conference*. doi:10.2118/173337-MS

Cieplicki, R., Eisner, L. and M. Mueller, 2014. Moment and moment magnitude of seismic events detected and located by stacking. *Geophysics*, 79(6), A57-A61. doi:10.1190/GEO2014-0179.1

Clarke H., Eisner, L., Styles, P. and P. Turner, 2014. Felt seismicity associated with shale gas hydraulic fracturing: The first documented example in Europe. *Geophys. Res. Lett.*, 41, 8308–8314. doi:10.1002/2014GL062047

Cornet, F.H. and Y. Jianmin, 1995. Analysis of induced seismicity for stress field determination and pore pressure mapping. *Pure and Appl. Geophys.*, 145(3), 677-700. doi:10.1007/BF00879595

De Meersman, K., Kendall, J. and M. van der Baan, 2009. The 1998 valhall microseismic data set: an integrated study of relocated sources, seismic multiplets, and S-wave splitting. *Geophysics*, 74(5), B183–B195.

Dricker, I., Friberg, P., Epiphansky, A., Kushnir, A., Rozhkov, M. and A. Varypaev, 2012. Statistically optimal technique of simultaneous event location and focal mechanism determination of weak microseismicity using surface arrays. *SEG Technical Program Expanded Abstracts*, 351, 1–5.

Droujinine, A.B., Oates, S. and J. Ita, 2011. Elastic Full Waveform Inversion for Locations and Moment Tensors of Microseismic Events. *73rd EAGE Conference and Exhibition*, extended abstracts C004, Vienna.

Dufumier, H. and L. Rivera, 1997. On the resolution of the isotropic component in moment tensor inversion. *Geophys. J. Int.*, 131(3), 595–606. doi:10.1111/j.1365-246X.1997.tb06601.x

Duncan, P.M., 2005. Is there a future for passive seismic? *First Break*, 23, 111-115.

Duncan, P.M. and L. Eisner, 2010. Reservoir characterization using surface microseismic monitoring. *Geophysics*, 75(5), 75A139–75A146. doi:10.1190/1.3467760

Eaton, D.W., Akram, J., St-Onge, A. and F. Forouhideh, 2011. Determining microseismic event locations by semblance-weighted stacking. *CSPG CSEG CWLS Convention*, Calgary.

Eaton, D.W. and F. Forouhideh, 2011. Solid angles and the impact of receiver-array geometry on microseismic moment-tensor inversion. *Geophysics*, 76(6), WC75-WC83. doi:10.1190/GEO2011-0077.1

Eaton, D.W. and A.B. Mahani, 2015. Focal mechanisms of some inferred induced earthquakes in Alberta, Canada. *Seismol. Res. Lett.*, 86(4). doi:10.1785/0220150066

Eaton, D.W., van der Baan, M., Birkelo, B. and J.B. Tary, 2014. Scaling relations and spectral characteristics of tensile microseisms: Evidence for opening/closing cracks during hydraulic fracturing. *Geophys. J. Int.*, 196(3), 1844-1857. doi:10.1093/gji/ggt498

Economides, M.J. and K.G. Nolte, 2003. *Reservoir Stimulation*, John Wiley, Hoboken, N.J., 5.1 – 5.14.

Einšpigel, D. and L. Eisner, 2012. Detection of perforation shots in surface monitoring: the attenuation effect. *SEG Technical Program Expanded Abstracts*, 342, 1–5.

Einšpigel, D. and L. Eisner, 2014. The differences in the detectability of perforation shots and microseismic events in the surface monitoring: the attenuation effect. *Acta Geodyn. et Geomater.*, 11(2), 159–164.

Eisner, L., Gei, D., Hallo, M., Opršal, I. and M. Ali, 2013. The peak frequency of direct waves for microseismic events. *Geophysics*, 78(6), A45–A49.

Eisner, L., Hulsey, B.J., Duncan, P., Jurick, D., Werner, H. and W. Keller, 2010a. Comparison of surface and borehole locations of induced seismicity. *Geophys. Prospect.*, 58(5), 809–820.

Eisner, L., Janská, E., Opršal, I. and P. Matoušek, 2011. Seismic analysis of the events in the vicinity of the Preese Hall well. *link: http://www.cuadrillaresources.com/news/news/*

Eisner, L., Williams-Stroud, S., Hill, A., Duncan, P. and M. Thornton, 2010(b). Beyond the dots in the box: Microseismicity-constrained fracture models for reservoir simulation. *The Leading Edge*, 29(3), 326-333. doi:10.1190/1.3353730

Foulger, G.R., Julian, B.R., Hill, D.P., Pitt, A.M., Malin, P.E. and E. Shalev, 2004. Non double-couple microearthquakes at Long Valley caldera, California, provide evidence for hydraulic fracturing. *Journal of Volcanology and Geothermal Res.*, 132, 45-71. doi:10.1016/S0377-0273(03)00420-7

Gajewski, D., Anikiev, D., Kashtan, B., Tessmer, E. and C. Vanelle, 2007. Localization of seismic events by diffraction stacking. *SEG Technical Program Expanded Abstracts*, 26(1), 1287–1291.

Gajewski, D. and E. Tessmer, 2005. Reverse modelling for seismic event characterization. *Geophys. J. Int.*, 163(1), 276–284.

Gei, D., Eisner, L. and P. Suhadolc, 2011. Feasibility of estimation of vertical transverse isotropy from microseismic data recorded by surface monitoring arrays. *Geophysics*, 76, WC117-WC126.

Gharti, H., Oye, V., Roth, M. and D. Kühn, 2010. Automated microearthquake location using envelope stacking and robust global optimization. *Geophysics*, 75(4), MA27–MA46. doi:10.1190/1.3432784

Gharti, H., Oye, V., Kuhn, D. and P. Zhao, 2011. Simultaneous microearthquake location and moment tensor estimation using time reversal imaging. *SEG Technical Program Expanded Abstracts*, 319, 1632–1637.

Grigoli, F., Cesca, S., Amoroso, O., Emolo, A., Zollo, A. and T. Dahm, 2014. Automated seismic event location by waveform coherence analysis. *Geophys. J. Int.*, 196(3), 1742–1753.

Grechka, V., 2015. On the feasibility of inversion of single-well microseismic data for full moment tensor. *Geophysics*, 80(4), KS41-KS49. doi:10.1190/geo2014-0471.1

Grechka, V., and W. Heigl, 2017. *Microseismic Monitoring.* eISBN: 978-1-56080-348-5, ISBN: 978-1-56080-347-8. doi:10.1190/1.9781560803485

Grechka V., Mazumdar, P., and S.A. Shapiro, 2010. Predicting permeability and gas production of hydraulically fractured tight sands from microseismic data. *Geophysics*, 75(1): B1-B10. doi:10.1190/1.3278724

Grechka, V., Zhao Li, Bo Howell, and V. Vavryčuk, 2016. Single-well moment tensor inversion of tensile microseismic events. *Geophysics*, 81(6), KS219-KS229. doi:10.1190/geo2016-0186.1

Gu, H., Siebrits, E. and A. Sabourov, 2008. Hydraulic fracture modeling with bedding plane interfacial slip. *Society of Petroleum Engineers*, SPE 117445. doi:10.2118/117445-MS

Gu, H., Weng, X., Lund, J.B., Mack, M.G., Ganguly, U. and R. Suarez-Rivera, 2011. Hydraulic fracture crossing natural fracture at non-orthogonal angles, a criterion, its validation and applications. *Society of Petroleum Engineers*. doi:10.2118/139984-MS

Guo, Y., Zhang, K. and K.J. Marfurt, 2010. Seismic attribute illumination of Woodford shale faults and fractures, Arkoma basin, OK. *SEG Technical Program Expanded Abstracts 2010*, 1372-1376. doi:10.1190/1.3513097

Gutenberg, B. and C.F. Richter, 1954. *Seismicity of the Earth and Associated Phenomena*. 2nd edn, Princeton Univ. Press.

Haldorsen, J., Brooks, N. and M. Milenkovic, 2013. Locating microseismic sources using migration-based deconvolution. *Geophysics*, 78(5), KS73–KS84.

Harper, T.R. and N.C, Last, 1990. Response of fractured rock subject to fluid injection, Part II. Characteristic behavior. *Tectonophysics*, 172, 33-51.

Heidbach O., Tingay, M., Barth, A., Reinecker, J., Kurfeß, D. and B. Müller, 2008. *The World Stress Map database release 2008*. doi:10.1594/GFZ.WSM.Rel2008

Hill, D.P., 1977. A model for earthquake swarms. *J. Geophys. Res.*, 82(8), 1347–1352. doi:10.1029/JB082i008p01347

Hubbert, M.K. and D.G. Willis, 1957. Mechanics of hydraulic fracturing. *Journal Petroleum Tech*., 9(6), 153-166.

Hudson, J., Pearce, R. and R. Roberts, 1989. Source type plot for inversion of the moment tensor. *J. Geophys. Res.*, 94, 765–774.

Hull, R.A., Meek, R., Bello, H. and D. Miller, 2017. Case History of DAS Fiber-Based Microseismic and Strain Data, Monitoring Horizontal Hydraulic

Stimulations Using Various Tools to Highlight Physical Deformation Processes (Part A). *Unconventional Resources Technology Conference*, Austin, Texas, 24-26 July 2017, 3050-3062.

Janská E., Eisner L. and I. Opršal, 2014. Vector Fidelity of Downhole Receivers for Microseismic Monitoring Revisited. *5th EAGE passive seismic workshop in Lisbon*, PSP18.

Jechumtálová, Z., Chu, F., Rong, J., Procházka, J. and L. Eisner, 2016. Downhole Microseismic Data Processing - Consistency of Locations, Source Mechanisms and Stress State. *78th EAGE Conference and Exhibition*, Extended Abstract. doi:10.3997/2214-4609.201600720

Jechumtálová, Z. and L. Eisner, 2008. Seismic source mechanism inversion from a linear array of receivers reveals non-double-couple seismic events induced by hydraulic fracturing in sedimentary formation. *Tectonophysics*, 460(1-4), 124-133. doi:10.1016/j.tecto.2008.07.011

Jechumtálová, Z. and J. Šílený, 2005. Amplitude ratios for complete moment tensor retrieval. *J. Geophys. Res.*, 32, 22, L22303. doi:10.1029/2005GL023967

Julian, B.R., Foulger, G.R. and F. Monastero, 2007. Microearthquake moment tensors from the Coso geothermal area. *Proceedings of 32nd Workshop on Geothermal Reservoir Engineering*, Stanford University, SGPTR-183.

Kagan, Y.Y., 1991. 3-D rotation of double-couple earthquake sources. *Geophys. J. Int.* (1991) 106(3), 709-716. doi:10.1111/j.1365-246X.1991.tb06343.x

Kao, H. and S.-J. Shan, 2004. The source-scanning algorithm: mapping the distribution of seismic sources in time and space. *Geophys. J. Int.*, 157(2), 589–594.

Kao, H. and S.-J. Shan, 2007. Rapid identification of earthquake rupture plane using source-scanning algorithm. *Geophys. J. Int.*, 168(3), 1011–1020.

Karrenbach, M., Ridge, A., Cole, S., Boone, K., Kahn, D., Rich, J., Silver, K. and D. Langton, 2017. DAS Microseismic Monitoring and Integration With Strain Measurements in Hydraulic Fracture Profiling. *Unconventional Resources Technology Conference*, Austin, Texas, 24-26 July 2017, 1316-1330.

Keshavarzi, R. and R. Jahanbakhshi, 2013. Investigation of hydraulic and natural fracture interaction: Numerical modeling or artificial intelligence? Effective and Sustainable Hydraulic Fracturing, Dr. Rob Jeffrey (Ed.), InTech. doi:10.5772/56382

Kiselevitch, V.L., Nikolaev, A.V., Troitskiy, P.A. and B.M. Shubik, 1991. Emission tomography: main ideas, results, and prospects. *SEG Technical Program Expanded Abstracts*, 441, 1602–1602.

Klimeš, L., 2012. Sensitivity of seismic waves to structure. *Stud. geophys. geod.*, 56, 483-520.

Kushnir, A., Varypaev, A., Dricker, I., Rozhkov, M. and N. Rozhkov, 2014. Passive surface microseismic monitoring as a statistical problem: location of weak microseismic signals in the presence of strongly correlated noise. *Geophys. Prospect.*, 62, 819–833. doi:10.1111/1365-2478.12124

Lambaré, G., Lucio, P.S. and A. Hanyga, 1996. Two-dimensional multivalued traveltime and amplitude maps by uniform sampling of a ray field. *Geophys. J. Int.*, 125, 584-598.

Lay, T. and T.C. Wallace, 1995. *Modern Global Seismology*. Academic Press, San Diego, pp. 313-356.

Liao, Y.-C., Kao, H., Rosenberger, A., Hsu, S.-K. and B.-S. Huang, 2012. Delineating complex spatiotemporal distribution of earthquake aftershocks: an improved source-scanning algorithm. *Geophys. J. Int.*, 189(3), 1753–1770.

Mahrooqi, S., Busaidi, S., Ismaili, I., Clow, F., Urbancic, T., Baig, A. and A. Kassam, 2013. Beyond the dots - Microseismic monitoring of a fractured reservoir during steam injection in Oman. *75th EAGE Conference and Exhibition*, Extended Abstract. doi:10.3997/2214-4609.20130014

Maxwell, S.C., 2014. Microseismic imaging of hydraulic fracturing: Improved engineering of unconventional shale reservoirs. *SEG Distinguished Instructor Series No. 17*.

Maxwell, S.C., Rutledge, J., Jones, R. and M. Fehler, 2010. Petroleum reservoir characterization using downhole microseismic monitoring. *Geophysics*, 75(5), 75A129–75A137, doi:10.1190/1.3477966

McMechan, G.A., 1982. Determination of source parameters by wavefield extrapolation. *Geophys. J. R. astr. Soc.*, 71(3), 613–628.

Mendecki, A.J., 1993. Real time quantitative seismology in mines: keynote address. *3rd International Symposium on Rock bursts and Seismicity in Mines*, Kingston, Ontario, Canada, pp. 287–295, Balkema, Rotterdam.

Moser, T.J. and V. Červený, 2007. Paraxial ray methods in anisotropic inhomogeneous media. *Geophys. Prospect.*, 55, 21-37.

Mustać, M. and H. Tkalčić, 2016. Point source moment tensor inversion through a Bayesian hierarchical model. *Geophys. J. Int.*, 204(1), 311-323. doi:10.1093/gji/ggv458, 2016

Neidell, N. and M. Taner, 1971. Semblance and other coherency measures for multichannel data. *Geophysics*, 36(3), 482–497. doi:10.1190/1.1440186

Neuhaus, C.W., Blair, K. Telker, C. and M. Ellison, 2013. Hydrocarbon Production and Microseismic Monitoring - Treatment Optimization in the Marcellus Shale. *75th EAGE Conference and Exhibition incorporating SPE EUROPEC 2013*. SPE-164807-MS.

Neuhaus, C.W., Ellison, M., Telker, C. and K. Blair, 2014. Drainage estimation and proppant placement evaluation from microseismic data. *SPE/EAGE European Unconventional Resources Conference and Exhibition*, Extended abstract. doi:10.2118/167685-MS

Neuhaus, C.W., and J.L. Miskimins, 2012. Analysis of surface and downhole microseismic monitoring coupled with hydraulic fracture modeling in the Woodford shale. *SPE Europec/EAGE Annual Conference.* doi:10.2118/154804-MS

Nolen-Hoeksema, R.C., and L.J. Ruff, 2001. Moment tensor inversion of microseisms from the B-sand propped hydrofracture, M-site, Colorado. *Tectonophysics*, 336(1), 163-181. doi:10.1016/S0040-1951(01)00100-7

Pearson, C., 1981. The relationship between microseismicity and high pore pressures during hydraulic stimulation experiments in low permeability granitic rocks. *J. Geophys. Res.*, 86(B9), 7855–7864.

Pesicek, J.D., Cieślik, K., Lambert, M., Carrillo, P. and B. Birkelo, 2016. Dense surface seismic data confirm non-double-couple source mechanisms induced by hydraulic fracturing. *Geophysics*, 81(6), KS207-KS217. doi:10.1190/geo2016-0192.1

Phillips, W.S., Fairbanks, T.D., Rutledge, J.T. and D.W. Anderson, 1998. Induced microearthquake patterns and oil-producing fracture systems in the Austin chalk. *Tectonophysics*, 289(1), 153-169. doi:10.1016/S0040-1951(97)00313-2

Rodriguez, I.V., Sacchi, M. and Y.J. Gu, 2012. Simultaneous recovery of origin time, hypocentre location and seismic moment tensor using sparse representation theory. *Geophys. J. Int.*, 188(3), 1188–1202. doi:10.1111/j.1365-246X.2011.05323.x

Rutledge, J.T., Downie, R., Maxwell, S., Drew, J. and T. Fischer, 2013. Extension-shear microseismic mechanisms during hydraulic fracturing. *SEG Technical Program Expanded Abstracts 2013*, 2067-2072. doi:10.1190/segam2013-1387.1

Rutledge, J.T., and W.S. Phillips, 2003. Hydraulic stimulation of natural fractures as revealed by induced microearthquakes, Carthage Cotton Valley gas field, east Texas. *Geophysics*, 68(2), 441–452. doi:10.1190/1.1567214

Rutledge, J.T., Phillips, W.S. and M.J. Mayerhofer, 2004. Faulting induced by forced fluid injection and fluid flow forced by faulting: An interpretation of hydraulic fracture microseismicity, Carthage Cotton Valley gas field, Texas. *Bull. Seismol. Soc. Am*, 94, 1817–1830.

Rutledge, J.T., Yu, X. and S. Leaney, 2015. Microseismic shearing driven by hydraulic-fracture opening: An interpretation of source-mechanism trends. *The Leading Edge*, 34(8), 926. doi:10.1190/tle34080926.1

Robein, E., Cerda, F., Drapeau, D., Maurel, L., Gaucher, E. and E. Auger, 2009. Multi-network Microseismic Monitoring of Fracturing Jobs - Neuquen TGR Application. *71st EAGE Conference and Exhibition*, extended abstracts X009, Amsterdam.

Shapiro, S.A., 2008. *Microseismicity: a tool for reservoir characterization*. EAGE Publications, ISBN: 978-90-73781-70-2

Shapiro, S.A., Dinske, C. and E. Rothert, 2006. Hydraulic-fracturing controlled dynamics of microseismic clouds. *Geophys. Res. Lett.*, 33, L14312. doi:10.1029/2006GL026365

Šílený, J., 2009. Resolution of non-double-couple mechanisms: Simulation of hypocenter mislocation and velocity structure mismodelling. *Bull. Seismol. Soc. Am*, 99(4), 2265–2272. doi:10.1785/0120080335

Šílený, J., Hill, D.P., Eisner, L. and F.H. Cornet, 2009. Non–double-couple mechanisms of microearthquakes induced by hydraulic fracturing. *J. Geophys. Res.*, 114, B08307. doi:10.1029/2008JB005987

Simpson, D., Leith, W. and C. Scholz, 1988. Two types of reservoir-induced seismicity. *Bull. seism. Soc. Am.*, 78(6), 2025–2040.

Sipkin, S.A., 1982. Estimation of earthquake source parameters by the inversion of waveform data: synthetic waveforms. *Physics of the Earth and Planetary Interiors*, 30(2-3), 242-259, Special Issue Earthquake Algorithms.

Spötl, Ch., Houseknecht, D.W. and R.C. Jacques, 1998. Kerogen maturation and incipient graphitization of hydrocarbon source rocks in the Arkoma basin, Oklahoma and Arkansas: a combined petrographic and Raman spectrometric study. *Org. Geochem.*, 28, 535–542.

Staněk, F., Anikiev, D., Valenta, J. and L. Eisner, 2015. Semblance for microseismic event detection. *Geophys. J. Int.*, 201(3), 1362-1369. doi:10.1093/gji/ggv070

Staněk, F. and L. Eisner, 2013. New model explaining inverted source mechanisms of microseismic events induced by hydraulic fracturing. *SEG Technical Program Expanded Abstracts*, 2201–2205. doi:10.1190/segam2013-0554.1

Staněk, F., and L. Eisner, 2017. Seismicity induced by hydraulic fracturing in shales: A bedding plane slip model. J. *Geophys. Res.*, 122(10): 7912-7926, doi:10.1002/2017JB014213

Staněk, F., Eisner, L. and T.J. Moser, 2014. Stability of source mechanisms inverted from P-wave amplitude microseismic monitoring data acquired at the surface. *Geophys. Prospect.*, 62(3), 475–490. doi:10.1111/1365-2478.12107

Staněk, F, Jechumtálová, Z. and L. Eisner, 2015. Reservoir stress from microseismic source mechanisms. *The Leading Edge*, 34(8), 890–893, 895, doi:10.1190/tle34080890.1

Starr, J. and R. Jacobi, 2017. Simultaneous use of microseismic monitoring and DAS-strain measurements to analyze the anatomy of a hydraulic stimulation in the Marcellus Shale. *SEG Technical Program Expanded Abstracts 2017*, pp. 2841-2845.

Tan, Y. and T. Engelder, 2016. Further testing of the bedding-plane-slip model for hydraulic-fracture opening using moment-tensor inversions. *Geophysics*, 81(5), KS159-KS168. doi:10.1190/geo2015-0370.1

Tarantola, A., 2005. *Inverse Problem Theory and Model Parameter Estimation*. SIAM.

Thomsen, L., 2002. Understanding seismic anisotropy in exploration and exploitation. *Distinguished Instructor Short Course*, Distinguished instructor Series, No. 5, SEG, EAGE.

Thornton, M. and L. Eisner, 2011. Uncertainty in surface microseismic monitoring. *SEG Technical Program Expanded Abstracts*, 298, 1524–1528. doi:10.1190/1.3627492 van der Baan, M., Eaton, D.W. and G. Preisig, 2016. Stick-split mechanism for anthropogenic fluid-induced tensile rock failure. *Geology*, 44(7), 503-506 doi:10.1130/G37826.1

Vavryčuk, V., 2001. Inversion for parameters of tensile earthquakes. *J. Geophys. Res.*, 106(B8), 16.339-16.355. doi:10.1029/2001JB000372

Vavryčuk, V., 2005. Focal mechanisms in anisotropic media. *Geophys. J. Int.*, 161, 334-346.

Vavryčuk, V., 2007. On the retrieval of moment tensors from borehole data. *Geophys. Prospect.*, 55(3), 381–391. doi:10.1111/j.1365-2478.2007.00624.x

Vera Rodrigues, I., Gu, Y.J. and M.D. Sacchi, 2011. Resolution of seismic-moment tensor inversions from a single array of receivers. *Bull. Seismol. Soc. Am*, 101(6), 2634–2642. doi: 10.1785/0120110016

Vernik, L., 2008. Anisotropic correction of sonic logs in wells with large relative dip. *Geophysics*, 73, E1-E5.

Vincent, M.C., 2010. Refracs: Why do they work, and why do they fail in 100 published field studies? *SPE Annual Technical Conference and Exhibition*. doi:10.2118/134330-MS

Vinje, V., Iversen, E., Åstebøl, K. and H. Gjøystdal, 1996a. Estimation of multivalued arrivals in 3D models using wavefront construction — Part I. *Geophys. Prospect.*, 44, 819–842.

Vinje, V., Iversen, E., Åstebøl, K. and H. Gjøystdal, 1996b. Estimation of multivalued arrivals in 3D models using wavefront construction — Part II: Tracing and interpolation. *Geophys. Prospect.*, 44, 843–858.

Warpinski, N.R., Branagan, P.T., Wolhart, S.L. and J.E. Uhl, 1998. Mapping hydraulic fracture growth and geometry using microseismic events detected by a wireline retrievable accelerometer array. *SPE*, 40014.

Warpinski, N.R., Du, J. and U. Zimmer, 2012. Measurements of hydraulic-fracture-induced seismicity in gas shales. *SPE Hydraulic Fracturing Technology Conference*, SPE151597. doi:10.2118/151597-MS

Warpinski, N.R., Mayerhofer, M.J., Agarwal, K. and J. Du, 2013. Hydraulic fracture geomechanics and microseismic source mechanisms. *SPE Journal*, 18, 4, Society of Petroleum Engineers. doi:10.2118/158935-PA

Warpinski, N.R., Northrop, D.A., Schmidt, R.A., Vollendorf, W.C. and S.J. Finley, 1981. The Formation Interface Fracturing Experiment: An In Situ Investigation of Hydraulic Fracture Behavior Near a Material Property Interface. *Sandia National Laboratories Report*, SAND81-0938.

Waters, G., Dean, B., Downie, R., Kerrihard, K., Austbo, L. and B. McPherson, 2009. Simultaneous hydraulic fracturing of adjacent horizontal wells in the Woodford shale. *SPE Hydraulic Fracturing Technology Conference*. doi:10.2118/119635-MS

Williams-Stroud, S., Kilpatrick, J.E., Cornette, B., Eisner, L. and M. Hall, 2010. Moving outside of the borehole: characterizing natural fractures through microseismic monitoring. *First Break*, 28(7), 91-92.

Williams-Stroud, S., Ozgen, C. and R.L. Billingsley, 2013. Microseismicity-constrained discrete fracture network models for stimulated reservoir simulation. *Geophysics*, 78(1), B37-B47. doi:10.1190/geo2011-0061.1

Withers, M., Aster, R., Young, C., Beiriger, J., Harris, M., Moore, S. and J. Trujillo, 1998. A comparison of select trigger algorithms for automated global seismic phase and event detection. *Bull. seism. Soc. Am.*, 88(1), 95–106.

Yagi, Y. and Y. Fukahata, 2011. Introduction of uncertainty of Green's function into waveform inversion for seismic source processes. *Geophys. J. Int.*, 186, 711-720. doi:10.1111/j.1365-246X.2011.05043.x

Zahradník, J. and S. Custódio, 2012. Moment tensor resolvability: Application to Southwest Iberia. *Bull. Seismol. Soc. Am*, 102(3), 1235-1254. doi:10.1785/0120110216

Zhang, Y., Eisner, L., Barker, W., Mueller, M.C. and K.L. Smith, 2013. Consistent imaging of hydraulic fracture treatments from permanent arrays through a calibrated velocity model. *Geophys. Prospect.*. doi:10.1111/1365-2478.12017

Zhang, W. and J. Zhang, 2013. Microseismic migration by semblance weighted stacking and interferometry. *SEG Technical Program Expanded Abstracts*, 397, 2045–2049.

Zhao, H., 2005. A fast sweeping method for Eikonal equations. *Math. Comp.*, 74(250), 603–627.

Zhebel, O. and L. Eisner, 2012. Simultaneous microseismic event localization and source mechanism determination. *SEG Technical Program Expanded Abstracts*, 341, 1–5. doi:10.1190/segam2012-1033.1

Zimmer, U., 2011. Calculating stimulated reservoir volume (SRV) with consideration of uncertainties in microseismic-event locations. *Canadian*

Unconventional Resources Conference SPE Journal, SPE-148610-MS, Society of Petroleum Engineers. doi:10.2118/148610-MS

Zoback, M.D., 2007. *Reservoir geomechanics*. Cambridge University Press.

Zoback, M.L. and M.D. Zoback, 1980. State of stress in the conterminous United States. *J. Geophys. Res.*, 85, 6113-6156.